

Structure and composition dynamics
of single-crystal copper interfaces
and Fe-Ag and Fe-Cu nanoparticles

Dissertation
to obtain the degree of
doctor rerum naturalium (Dr. rer. nat.)

Submitted to
the Faculty of Chemistry and Biochemistry
at the Ruhr-University Bochum

by
Sebastian Kunze

*Science, my lad, is made up of mistakes, but they are mistakes which it is useful to make,
because they lead little by little to the truth.*
– Jules Verne

Berlin, 19.04.2021

Abstract

For heterogeneous (electro)catalysis, the catalytic properties of a material are foremost determined by its structure and composition at the interface between the catalyst and the reaction environment. However, both the structure and composition are not static factors, but parameters that respond dynamically to their environment. A deeper understanding of these dynamic processes is therefore required to be able to, in turn, make targeted improvements to electrocatalytic materials. Here, three projects are presented that each address the surface alterations that result from specific catalyst functionalization and activation treatments. First, we show the oxidation of Cu(100) and Cu(111) surfaces via a low-pressure O₂-plasma treatment, investigated by scanning tunneling microscopy, x-ray spectroscopy and low energy electron diffraction. We traced the evolution of Cu, Cu₂O and CuO and the surface structure over time and found that the surface orientation plays a critical role in the time-dependent oxidation process. The results show that initial surface reconstruction is accompanied by island growth, coalescing into a thin layer for longer exposure times. The composition trace reveals an initial Cu₂O overlayer until eventually a thicker CuO is grown on top of it. The second study investigates the effects of a pulsed potential on the surface morphology of a Cu(100) single crystal. The stepped surface of a UHV-prepared crystal experiences large alterations in the form of cubic protrusions evolving during the pulsed potential in a certain potential window, resulting in a reconstructed surface and highly reactive structural motifs. We also identified key potentials and pulse durations and their corresponding structural changes to allow for separation of morphological from oxidation state effects in future studies. In the final project, nuclear resonant inelastic X-ray scattering (NRIXS) and X-ray absorption fine-structure spectroscopy (XAFS) measurements were employed to gain insight into the dynamic structure and surface composition of FeCu and FeAg nanoparticles under CO₂RR conditions. We also extracted their correlations with the catalytic activity and selectivity. The formation of a core-shell structure during CO₂RR for FeAg NP was inferred from the phonon density of states (PDOS), extracted from NRIXS data, and XAFS measurements.

Contents

1	Background	9
1.1	Carbon Dioxide: Waste or Resource?	9
1.2	The electrochemical CO ₂ reduction reaction	11
1.3	The Central Role of the Catalyst Surface	13
1.4	Nanostructuring	14
1.5	Project Objectives	15
2	Methods and Experimental Setups	17
2.1	Scanning Tunneling Microscopy	17
2.2	Atomic Force Microscopy	21
2.3	X-ray photoelectron spectroscopy (XPS)	23
2.4	UHV Systems	25
2.5	Single Crystal Preparation and Plasma Treatment	28
2.6	Electrochemical experiments without air exposure	30
2.7	Nuclear Resonant Inelastic X-ray Spectroscopy (NRIXS)	33
2.8	X-ray Absorption Fine Structure Spectroscopy (XAFS)	36
2.9	Synchrotron Setup for Spectroelectrochemistry	38
2.10	Nanoparticle Synthesis	39
2.11	Low Energy Electron Diffraction (LEED)	40
3	Plasma-assisted oxidation of Cu(111) and Cu(100)	43
3.1	Introduction	43
3.2	Experimental details	45
3.3	Results and Discussion	46
3.4	Summary	63
4	<i>In situ</i> generated morphological motifs on Cu(100) by pulsed electroreduction	67
4.1	Introduction	67

4.2	Experimental Details	69
4.3	Results and Discussion	71
4.4	Summary	81
5	<i>Operando</i> NRIXS and XAFS Investigation of Segregation Phenomena in FeCu and FeAg Nanoparticle Catalysts during CO ₂ Electroreduction	83
5.1	Introduction	84
5.2	Experimental Details	86
5.3	Results and Discussion	89
5.4	Summary	105
6	Conclusion and Outlook	107
7	Bibliography	111
8	Appendix for Plasma-assisted Oxidation of Cu(100) and Cu(111)	141
8.1	Cu LMM deconvolution	141
8.2	Work function measurements	143
8.3	O K-edge NEXAFS	145
8.4	Composition Analysis of NEXAFS spectra	145
8.5	Model of Copper oxide formation for Cu(100)	146
8.6	Composition fit of XPS data	148
8.7	Correlation between film thickness and plasma exposure time . . .	149
9	Appendix for <i>Operando</i> NRIXS and XAFS Investigation of Segregation phenomena in FeCu and FeAg nanoparticle catalysts during co ₂ electroreduction	153
9.1	Fitting of XPS spectra	153
9.2	Additional NRIXS data	154
9.3	Supplementary EXAFS Information	154
9.4	Synthesis of ⁵⁷ FeCl ₂ · 2 H ₂ O	156
9.5	Synthesis of Nanoparticles	159
10	List of Publications	163
11	Curriculum Vitae	165

This work was carried out in the period from April 2017 to April 2021 in the department of Experimental Physics 4 at the Ruhr-University Bochum and the Interface Science Department at the Fritz-Haber Institute in Berlin, with the support of the International Max Planck Research School for Interface Controlled Materials for Energy Conversion under the supervision of Prof. Dr. Beatriz Roldan Cuenya.

First Examiner: Prof. Dr. Beatriz Roldan Cuenya

Second Examiner: Prof. Dr. Wolfgang Schuhmann

Third Examiner: Prof. Dr. Martin Muhler

Abbreviations

AFM	Atomic Force Microscopy
bcc	body centered cubic
CA	Chronoamperometry
CE	Counter Electrode
CO ₂ RR	Carbon Dioxide Reduction Reaction
CV	Cyclic Voltammetry
EDX	Energy Dispersive X-ray Analysis
EC	Electrochemistry, Electrochemical
fcc	face-centered cubic
LDOS	Local Density of States
LEED/M	Low Energy Electron Diffraction/Microscopy
NEXAFS	Near Edge X-ray Absorption Fine Structure Spectroscopy
NP	Nanoparticle
NRIXS	Nuclear Resonance Inelastic X-ray Scattering
PDOS	Phonon Density of States
RE	Reference Electrode
RHE	Reversible Hydrogen Electrode
RT	Room Temperature
SPM	Scanning Probe Microscopy
STM	Scanning Tunneling Microscopy
SEM	Scanning Electron Microscopy
TEM	Transmission Electron Microscopy
UHV	Ultra High Vacuum
WE	Working Electrode
XAS	X-ray Absorption Spectroscopy
(E)XAFS	(Extended) X-ray Absorption Fine Structure Spectroscopy
XANES	X-ray Absorption Near Edge Spectroscopy
XPS	X-ray Photoelectron Spectroscopy

Acknowledgement

Besides the obvious material and intellectual benefits of pursuing a PhD, I found the people I have met during my time in Bochum and Berlin to be one of the greatest rewards. I want to dedicate this section, and with that, my sincere gratitude, to everyone who blessed me with their support and companionship.

First of all, none of this would be possible without my doctoral advisor, Prof. Dr. Beatriz Roldán Cuenya, who gave me the opportunity to do the PhD in her group. During my PhD, she advised and guided me patiently, but also encouraged me to pursue difficult projects. As a result, I have grown as a scientist and as a person. Starting in Bochum with only a handful of people and later transitioning to Berlin, I can say it was quite an adventure. For everything I mentioned and much more that I did not mention, I want to express my sincere gratitude.

Next, I would like to thank Prof. Dr. Wolfgang Schuhmann for being my second referee and advisor in my thesis advisory committee in the IMPRS SurMat. I would also like to thank Prof. Dr. Martin Muhler for agreeing to be my third referee. Their lectures during my chemistry education were further convincing me to go for a specialisation in the surface sciences.

I was blessed with engaging and productive scientific cooperation, and I want to express my gratitude and respect to my coauthors and collaborators, both in our group and from outside. I want to thank in particular Dr. Thomas Schmidt, Dr. Liviu Tanase, Dr. Mauricio Prieto and Lucas Caldas de Suza from the SMART beamline at BESSY II, as well as Dr. See Wee Chee and Dr. Janis Timoschenko at the FHI.

I had the great pleasure to meet Dr. Markus Heyde, who supported me throughout my stay, be it with a friendly talk or a pressure reducer for a minican. It was reassuring to always have a cheerful face nearby, and I want to especially thank him for his help in staying organized towards the end of my PhD.

I also want to thank all my great fellow lab members, students, postdocs, group leaders, technicians, and everyone from the Experimental Physics 4 and Interface Science Department. I am grateful to so many people: Ioannis, who always took care of us students, and who I'm always glad to meet again. Ilya and Nuria, for the great experiences on our beamline trips. Dennis, with whom I first worked on a new system. Rosa and Ruben, who somehow managed to make me appreciate summer more. I will still visit in winter, though. Fabian and David, my fellow Bochumers. Nikolai, for sharing his plentiful knowledge about UHV and STM and his humor with me. Also Bernd and Martin, who made our transition to Berlin much easier. Jared, for his positivity and our office chats. Jeffrey, for our thorough debates on everything, and Juan, who must be C1 by now. Weiming, Mauricio, Miguel and Clara, who were there with me whether at night or on weekends, in and outside of the lab. It made the challenges of the PhD much easier to bear with you around.

I am grateful for the people who joined me in my personal life away from the lab, especially Helen who supported me during my PhD. Also, I thank my friend Ping for the great time we shared during university and after. I am looking forward to more with you and Niklas. I also want to thank Philipp, who I am sure knows that he cannot escape me. Lastly, I want to thank Tobias for his excellent humor, and of course all my other friends with whom I enjoyed my life in Bochum and Berlin with.

Lastly, I was very fortunate to have had the financial and educational support of the International Max Planck Research School for Interface Controlled Materials for Energy Conversion (IMPRS SurMat). Many thanks to them and greetings to my fellow SurMat students.

Thesis Outline

This thesis focuses on three research projects, each addressed in an individual chapter. They are preceded by a background and experimental chapter. The former explains the overarching research topic and theme in order to set the following projects into context. This introduction is followed by a chapter of the combined theoretical and practical aspects of the methods used in the experimental work, including a brief explanation of the techniques and descriptions of the involved setups. The three subsequent chapters then present the results of the research projects, each chapter including the general structure of a research article, starting with an introduction outlining the current state of the literature, an experimental section with descriptions of processes and workflows, and a results and discussion section. In the appendix, additional data and descriptions are available that are excluded from the main text to increase readability. This thesis contains previously unpublished data and content that is either intended to be published soon or already published in peer-reviewed scientific journals. In order to streamline the reading and keep consistent with the structure of a thesis, parts of the supporting information and unpublished, additional data are incorporated at the appropriate places.

1 Background

1.1 Carbon Dioxide: Waste or Resource?

The first industrial revolution started over two-hundred years ago, and rapid development and progress have since transformed almost every aspect of civilization. Unfortunately, we have a serious problem: the ever increasing demand for energy is satisfied by the burning of fossil fuels (oil, coal and gas), which in turn releases enormous amounts of CO₂ into the atmosphere, year after year. The rising CO₂ levels have been identified as the driving force of global warming, heating up the atmosphere, with far-reaching negative consequences.¹⁻⁶ Logically, research towards technologies that reduce the emission of CO₂ and to remove it from the atmosphere and store it – i.e., carbon capture and sequestration (CCS) – has intensified.⁷⁻⁹ The former is envisioned by the utilisation of renewable energy resources, such as wind and solar power, although nuclear energy could also provide significant amounts of power.¹⁰⁻¹² The downside of renewable energy however, is the intermittent nature of its availability, requiring some form of energy storage that can store and release large amounts of energy, enough to supply a country for days.

But it is not only the energy sector that depends on fossil fuels. The petrochemical industry relies on the availability of hydrocarbons for the production of basic goods, such as polymers, oils, waxes and pharmaceuticals. The required olefins, aromatics and other hydrocarbons are the basic building blocks that are currently only available through processing of coal, oil and gas.¹³ It is evident that in the future, sustainable production of base chemicals will be necessary.^{14,15}

Curiously, there is already a biological paradigm that ties carbon dioxide fixation, energy storage and organic building blocks together. *Photosynthesis* is a sunlight powered biochemical process that fixates carbon dioxide in the form of a simple carbohydrate and utilizes it as an energy storage and to build more complex biomolecules.¹⁶

In kindred spirit, using carbon dioxide as a resource rather than a waste product could alleviate some of the addressed problems. Artificial fuel, its synthesis powered by renewable energy, would be a high density, CO₂-neutral substitute for fossil fuels. Combustion technologies have matured over a century, and merely replacing the fuel source would have considerable synergy with our current technologies. Carbon dioxide could also constitute a virtually unlimited supply of carbon compounds, if we can establish the chemistry to convert it. Obviously, the feasibility of each of these goals is contentious, but even partial success in implementing the valorization of CO₂ is an ecologically worthwhile endeavour.¹⁷ For the aforementioned reasons, the conversion of carbon dioxide is one of the proposed paths to a sustainable industry, along with the hydrogen economy.¹⁸

The chemical objective is also clear: Understand how CO₂ can be efficiently converted into reduced carbon compounds. Unfortunately, carbon dioxide is a remarkably stable and unreactive molecule. Comparing the formation enthalpy of CO₂ (-393 kJ mol^{-1})¹⁹ to that of water (-285 kJ mol^{-1})^{19,20} illustrates how thermodynamically favored the oxidation reaction is. Correspondingly, the reverse reaction is thermodynamically unfavorable and requires a significant amount of energy to facilitate. Chemistry has a solution to increase the reaction dynamics favorably via catalysis, reducing the activation barrier of the reaction.

In 1912, Paul Sabatier received the Nobel Prize for his work on the hydration of CO, a process that was made viable by Hans Tropsch and Franz Fischer with the development of the Fischer-Tropsch synthesis in 1925.^{21,22} This enabled the production of hydrocarbons from CO. As long as CO can be produced from it, any carbon source can be used for this process. One proposed process in research to utilize carbon dioxide from carbon capture is therefore to convert CO₂ into

CO first, and then continue with the established Fischer-Tropsch process, or use an adapted process for direct CO₂ conversion.²³

1.2 The electrochemical CO₂ reduction reaction

Starting in the 1980's, the group of Yoshio Hori made a fundamental discovery that opened another possibility. They discovered that CO₂ can be *directly* reduced to hydrocarbons and alcohols over copper electrodes in an electrocatalytic reaction.^{24,25} The CO₂ reduction reaction (CO₂RR) has been an increasingly researched topic since then. However, despite four decades of research, a number of obstacles that prevent an economically feasible CO₂RR application remain unsolved.^{26,27} The products obtained from the CO₂RR cover a wide range, and hence, steering selectivity towards a certain product is a priority. The second problem is the deviation of the required potentials to obtain the desired products; the reaction requires higher applied potentials than expected from thermodynamics. Table 1 summarizes a few CO₂ reduction reaction pathways to illustrate the variety of products and their standard reduction potentials E^0 . We also see that the reactions to C₂₊ products are many-electron reactions, which emphasizes that the involved reaction mechanisms are quite complex.

Reaction	E^0 (V vs RHE)
$2\text{H}^+ + 2\text{e}^- \longleftrightarrow \text{H}_2$	0.00
$\text{CO}_2 + 2\text{H}^+ + 2\text{e}^- \longleftrightarrow \text{HCOOH}$	-0.25
$\text{CO}_2 + 2\text{H}^+ + 2\text{e}^- \longleftrightarrow \text{CO} + \text{H}_2\text{O}$	-0.11
$\text{CO}_2 + 8\text{H}^+ + 8\text{e}^- \longleftrightarrow \text{CH}_4 + 2\text{H}_2\text{O}$	0.17
$\text{CO}_2 + 12\text{H}^+ + 12\text{e}^- \longleftrightarrow \text{C}_2\text{H}_4 + 4\text{H}_2\text{O}$	0.06
$\text{CO}_2 + 14\text{H}^+ + 14\text{e}^- \longleftrightarrow \text{C}_2\text{H}_6 + 4\text{H}_2\text{O}$	-0.27

Table 1: Products and half-cell potentials of several CO₂ reduction reactions.

The currently reported potential range at which the CO₂RR is yielding significant amounts of products is around -1 V. The *overpotential* ($\eta = E_{\text{applied}} - E^0$), compared to the expected value, is a major source of energy inefficiency.

In addition to selectivity and activity there is a third parameter to take into account when researching catalysts, which is their stability. Even the most active and selective catalysts are economically unfeasible if they are not stable over a sufficiently long period of time. Hence, stability is another factor to consider.

To find solutions to overcome the inefficiencies of the CO₂RR, and indeed those of other catalysed heterogeneous electrochemical reactions, an intricate network of contributing factors needs to be unravelled. In the case of the CO₂RR, one of these factors to consider is the reaction medium, i.e. the electrolyte in which the reaction takes place and its composition and pH. Other factors are temperature and pressure and the gas feed composition. In addition, there are technical solutions to consider in order to overcome certain limitations, such as the use of gas diffusion electrodes to overcome the limited solubility of CO₂ in aqueous media. The most extensive research however is focused on the catalyst material itself, since it is the essential piece in catalysis. Naturally, two main factors contribute to the catalytic performance (i.e. activity, selectivity and stability), which are the composition of the material and its structure. In the case of heterogeneous (electro)catalysts, there is yet another complication to consider: The bulk of a material is not in contact with the reactants. This requires researchers to investigate the surface of a catalyst specifically. In turn, it does not mean that the near-surface region can be neglected, since it still has an effect on the surface itself, through strain induced lattice widening or shrinking, and electronic polarization, for example through an added second metal.^{28–31}

Of all these contributing factors, we now want to narrow it down thematically to the role of the surface, its structure and composition, and expand on why it is important to consider it in the frame of the CO₂RR.

1.3 The Central Role of the Catalyst Surface

In order to design a catalyst that is as energy efficient and selective as possible, we need to understand how the reaction dynamics are controlled by the properties of the catalyst. Since electrochemical processes occur at the interface between the electrode and the electrolyte, this is primarily a surface science question and involves interdisciplinary concepts from physics and chemistry.

Studying the fundamental processes facilitating the CO₂RR on surfaces is difficult, since it is not obvious or straightforward which structural aspects determine the catalytic activity. The initial studies on CO₂RR by Hori et al. were done on copper foils²⁴. These polycrystalline surfaces contain various grains of rotated (hkl) oriented planes, and the atomic structures at the grain boundaries are a factor that is difficult to account for. Hence, the catalytic performance of polycrystalline surfaces is always a result of a combination of surface structures. This makes studies on single crystal surfaces of defined planar orientations Cu(hkl) particularly valuable, since they reduce complexity and are reproducible model surfaces. Furthermore, they lend themselves to set into context computational studies such as DFT calculations, which assume homogeneous surfaces, which are approximated better by the flat single crystal surfaces.²⁷

Interestingly, even the surface orientation of the low-index copper surfaces, which has fewer step sites than the higher index surfaces, has an effect on the product distribution.³² Of these, the Cu(100) surface is the most selective for ethylene, while Cu(110) and Cu(111) preferentially produce methane.^{33,34}

A major challenge to draw conclusions from experiments on electrode surfaces lies in the transformations these undergo after their preparation, i.e. the surface that was characterized after preparation might not be the surface that exists during reaction. Studies on copper single crystals in various electrochemical reactions have indeed shown that adsorbate-induced reconstructions and facet-reordering have to be taken into account.³⁵

The fact that surfaces have a major influence on the course of a reaction but experience transformations during that reaction necessitates studies on the dynamics of these transformations. An understanding of the underlying processes is needed to make meaningful conclusions from further experiments on the catalytic performance of a given surface. In the end, a full picture of the involved processes can give us the tools to design a catalyst that is tailored to a specific reaction.

1.4 Nanostructuring

The more active surface area a catalyst has (in relation to volume or mass), the more products can be produced in a given time. Another goal of catalysis research is therefore to maximize the available surface area of a catalyst material. For an extreme example, nanoparticles offer dramatically higher surface-to-volume ratios than single-crystals. Their use in industrial applications is therefore an extensively studied topic, and studies focused on realistic systems, apart from the model systems that single crystals represent, need to take this into account. Besides the increased surface-to-volume ratio, several studies have shown that size effects can strongly enhance the activity and selectivity towards desired products.³⁶ However, it is also known for CO₂RR that very small particles increase the parasitic H₂ evolution due to a high amount of uncoordinated sites that bind hydrogen strongly.^{37,38}

1.5 Project Objectives

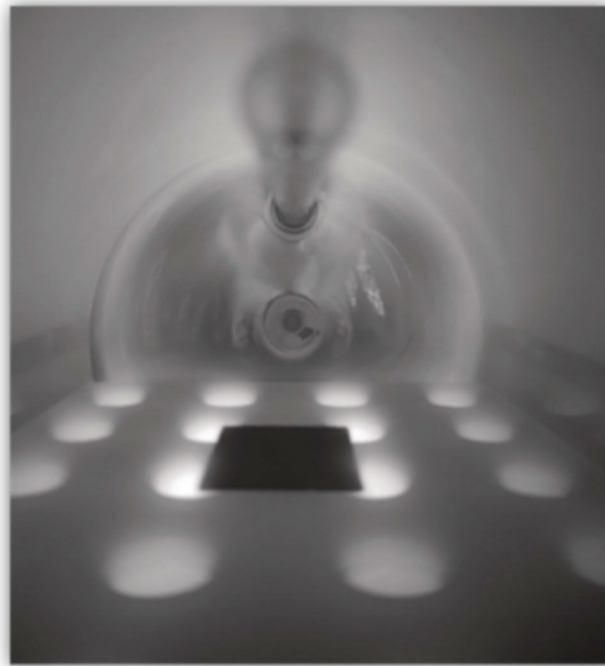
As has been laid out in the previous sections, gaining insights into the surface dynamics under different environmental conditions is a critical part in the pursuit of rational catalyst design. The projects presented here address this from three angles. The first project, chapter 3, was pursued based on previous findings that oxygen plasma treated copper foils exhibit increased catalytic performance for CO₂RR. The goal here was to elucidate the effects of a plasma treatment on a copper surface, from the standpoints of structural changes and the copper species contents in the form of metallic copper and copper oxides. This project was planned to be done in a very controlled UHV environment and under mild conditions, performed on well-defined surface orientations, to yield fundamental understanding on an atomic scale.

The second project is set in a more complex environment, as we wanted to explore the surface morphology of the Cu(100) surface after different pulsed potentials. The crystal was to be prepared *in situ*, to most closely resemble an ideal surface, and to avoid the significant impacts that the preconditions of Cu surfaces have on the outcome.^{39,40}

The third project is an attempt of an indirect approach to structure determination for very complex systems. As explained above, the single crystal samples, which are ideal for SPM techniques, display low current densities due to their limited surface area, which makes them unsuitable for industrial application.²⁷ A possible solution to this are nanostructured catalysts with much higher surface area per volume, but the scanning probe methods we used in the previous projects are unsuitable to address these systems, since they are limited to flat samples. We devised a project to probe the structure and composition changes of a bimetallic nanoparticle array on a carbon support under realistic reaction conditions, with operando spectroscopic methods.

Chapter 2

Methods and Experimental Setups



2 Methods and Experimental Setups

This chapter contains brief descriptions of the most important methods and equipment setups that were used in the course of these projects. The *project-specific* procedures and workflows of the experiments are explained in detail in the related experimental sections in chapters 3 to 5.

2.1 Scanning Tunneling Microscopy

Scanning tunneling microscopy (STM) utilizes tunneling of electrons to image a surface at the atomic scale. The fundamental concept relies on bringing a conductive tip, mostly tungsten or a Pt/Ir alloy, in close proximity (but not physical contact) to a conductive surface until a small current (pA to nA range) can be measured. A bias voltage between the sample and the tip is usually applied to shift the Fermi levels in respect to each other to enable electron flow. Since there is no direct contact between the tip and the sample, electrons can only flow via quantum tunneling.⁴¹ Quantum tunneling is a classic example of both quantum mechanics and the particle-wave duality.

The physical quantity which is detected is a current, i.e., the number of electrons which are tunneling through the gap between the sample and tip. The probability of an electron to tunnel through the gap is always greater than zero for a finite barrier, but decreases exponentially with the width of the barrier.

This scaling decrease is ultimately what enables the subatomic resolution in the direction of the surface normal, as the tunneling current I_t is proportional to equation 1:

$$I_t \propto G(E)e^{-2\gamma z} \quad (1)$$

$G(E)$ is a function of energy and γ is a decay length specific for a material (range of 1 \AA^{-1}). As can be seen by the exponential relationship between the tunneling current and the barrier width (which is the sample-tip-distance for all practical purposes), small changes in the sample-tip distance δz in turn result in a proportionally large change of the tunneling current I_t . This is utilized in STM, by bringing a tip very close to a surface in the order of a few \AA and controlling the distance precisely.⁴²

In order to image a surface with STM, the tip is brought close to the surface until a current is detected. It is then scanned in a rastering pattern of lines over the surface, in either constant height or constant current mode. The former keeps the tip at a set height while the current is recorded. The latter utilizes a feedback loop, adjusting the tip-sample distance continuously to maintain a set current. The resulting images are mostly correlated to the surface topography, but the correct dependency is the local density of states (LDOS), since this determines the electron flow. This means that protrusions or depressions in an image are not necessarily topographic, but may just be variations in the LDOS due to adsorbates or surface reconstructions. Even on a surface consisting of just one element, electronic anisotropy can alter the LDOS significantly.⁴¹⁻⁴³

The STM data shown in this thesis were taken with two STMs, located in different UHV systems. They share the same design, with a few differences. The SPM chamber of UHV system 1 (labeled as 'Bochum') hosts the SPECS SPM Aarhus 150 NAP scanning probe microscope, a version of the Aarhus STM design, modified to bridge the pressure gap from UHV to near atmospheric pressures (NAP) up to 100 mbar. Figure 1 shows a photograph of the microscope and the position of some of its components. It can be operated at variable temperatures,

from 120 K by LN_2 cooling to 850 K via heating with an infra-red lamp heater. The sample stage is encased in a reaction cell with integrated pumping and gas inlet/outlet, which can be completely sealed off by a lid. The cell can then be pressurized up to 100 mbar without affecting the UHV outside the cell. A three spring suspension in conjunction with viton dampeners decouples the microscope from vibration and regularly achieves mechanical stability with a noise floor of 10 pm over a range of 1 Hz to 1000 Hz.

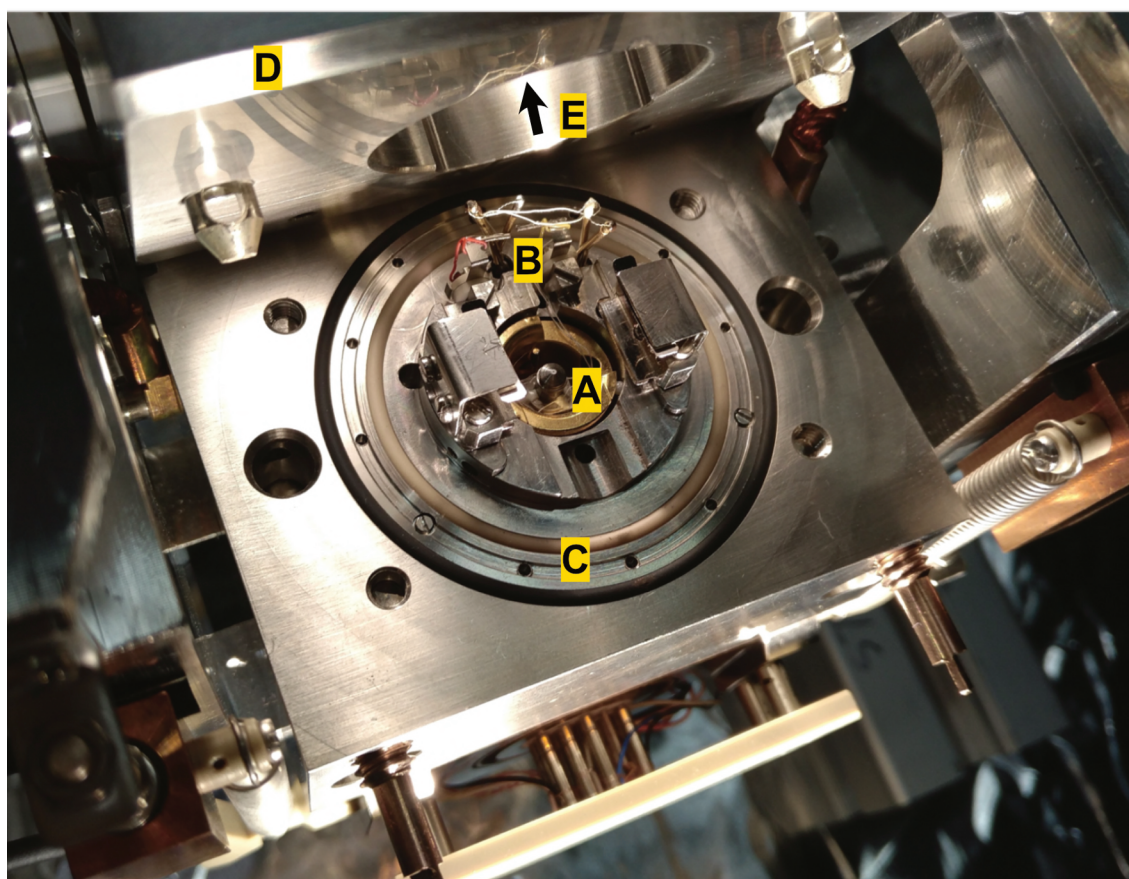


Figure 1: Top-view of the SPM Aarhus 150 NAP reaction cell with open lid and position of the components. Note that the halogen lamp is inside the cutout of the lid and not visible from this angle. **A:** KolibriSensor or STM tip. **B:** Thermocouples. **C:** Cell gaskets and differential pumping holes. **D:**

The scanner consists of a combined inchworm coarse approach motor and a piezo tube drive for scanning. In contrast to many other setups, it is not possible to do lateral coarse movements, but the design allows for a wide lateral scan range of $2.4\ \mu\text{m}$. Two types of probes may be used - traditional STM

tips, and a quartz-oscillator probe designated as KolibriSensor™. While the former supports only the STM modes, the latter enables also non-contact atomic force microscopy (NC-AFM) operation. The KolibriSensor features a separated tungsten tip, which means that the current and force signals can be recorded separately and independently. An ion gun IQE 11/35 in the chamber provides the means for tip preparation, i.e., it allows to condition a tip (also the tips of a KolibriSensor) via argon sputtering. Control of the SPM is realized with the Nanonis SPM Control System (both hardware and software suite).

The STM located in UHV system 2 (labelled as 'MOKE') is a high-temperature version of the STM Aarhus 150, the STM Aarhus 150 HT. The reaction cell for NAP operation is absent here, and replaced by the standard microscope body. There is no infra-red heater, instead a retractable heating filament can be placed atop the sample stage for e-beam heating of the sample during STM experiments. Temperatures of up to 1000 K can be achieved when used with a corresponding high-temperature sample holder. This microscope does not make use of a KolibriSensor™, so it only operates in STM mode.

2.2 Atomic Force Microscopy

Atomic force microscopy (AFM) was developed shortly after the invention of the STM, and functions based on the same scanning principle, but uses a different physical quantity to probe the surface. In this case, the forces between the tip and the sample surface are the probed interaction. When brought into contact, several forces act between the tip and the sample. The most important of these are van-der-Waals forces, electrostatic and capillary forces, as well as the chemical forces resulting from overlapping wave function and the Pauli exclusion principle.^{43/44}

The operating principle of AFM relies on sensing the sum of these forces between sample and tip. In cantilever-based AFMs, a tip with nanoscale apex (3 nm to 15 nm) is mounted on the underside of a cantilever, which in turn is mounted on a silicon carrier. A laser beam is projected onto the cantilever and reflected onto a detector, which is often a 4-quadrant photodiode. If the tip is brought into contact with the sample and the cantilever starts bending, the deflection can be measured. When scanning, the deflection angle (and thus, the force) is kept constant by a feedback loop while the sample is scanned.^{42/44} There are several operating modes for AFM. The contact mode works as just described, by dragging the tip across the surface at a set force. This however has the downside of destructive interactions on soft samples and blunting the tip apex over time. The most commonly used mode is the intermittent mode (different manufacturers of AFMs have since invented their own naming schemes, such as Brukers' TappingMode™), where the cantilever is oscillated at a resonance frequency and a high amplitude (around 20 nm to 100 nm) and regularly brought into contact with the sample until a threshold amplitude change is detected, induced by the interaction with the surface. This mode is amplitude-modulated and results in low destructive interference with the sample topography as it avoids lateral forces. Non-contact modes are mainly used in UHV-AFM and utilize a different sensing mechanism than cantilever based AFM. There, the high oscillation frequencies and a frequency modulated feedback loop are used to avoid contact between tip and sample.⁴³

The Bruker MultiMode 8 (figure 2) is the atomic force microscope utilized to record all the shown AFM images in this work. It was configured in a traditional cantilever and laser configuration. This MultiMode 8 model features a maximum lateral range of 15 μm . It was operated in manual (as opposed to the automated ScanAsyst mode) TappingMode™, which, as mentioned, is Brukers' implementation of an intermittent mode. The pyramidal, Si_3N_4 -coated AFM tips from Team-Nanotec (Aspire™300) with an 8 nm tip radius were tuned to their main resonance frequency of 300 kHz. Vibration isolation was implemented with an active damping stage supporting the AFM.

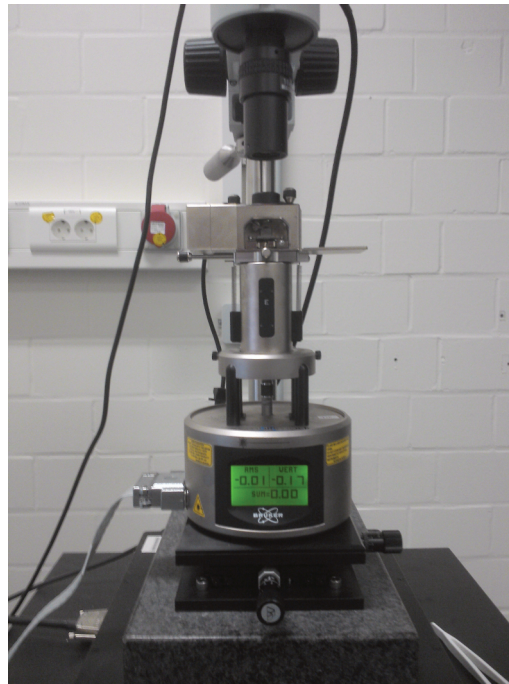


Figure 2: Bruker MultiMode 8 atomic force microscope.

2.3 X-ray photoelectron spectroscopy (XPS)

Compositional analysis of a surface is a complementary technique to the morphological analysis of scanning probe microscopy. X-ray photoelectron spectroscopy (XPS) offers very surface sensitive probing depths of 1.5 nm to 6 nm and allows to analyze the surface of a sample by its elemental composition. The basic concept follows the photoelectric effect, which is the phenomenon of photons in the X-ray energy range ejecting core electrons from an atom.⁴⁵ Figure 3 shows the photoelectric and Auger processes.

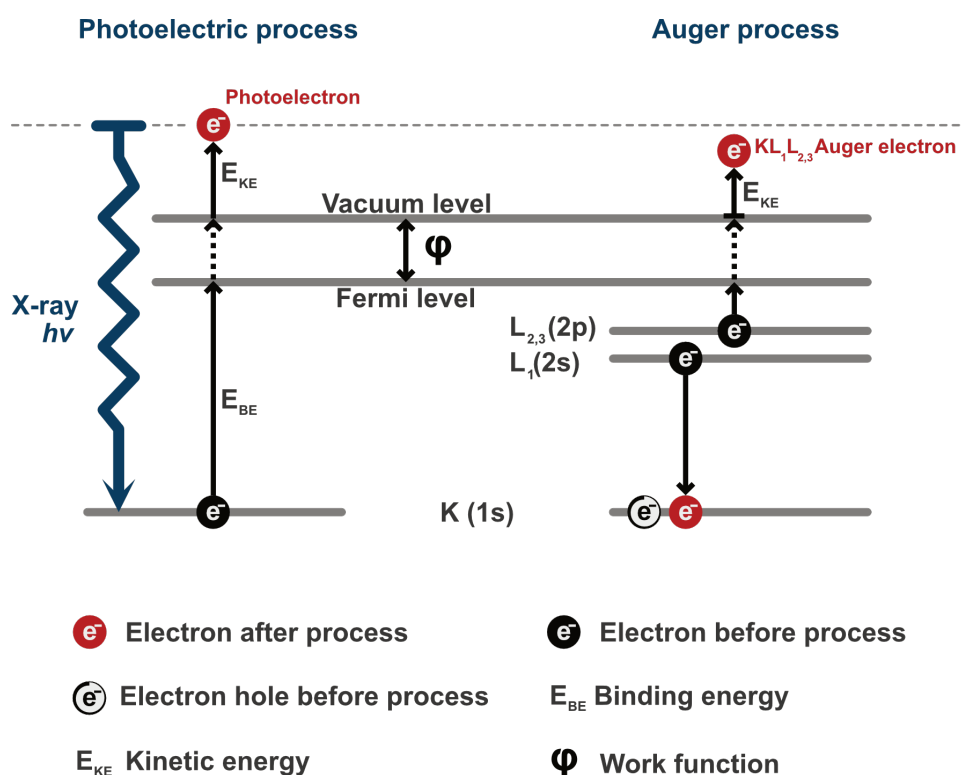


Figure 3: Qualitative depiction of photoelectron (left) and Auger electron emission (right). Left: Absorption of X-ray photon, emission of photoelectron. Right: Ionized atom; relaxation to lower energy state by transition of a higher shell electron to the core hole. The released energy induces the ejection of an Auger electron.

In an XPS measurement, X-rays of a specific energy (mostly Al $K\alpha$ at 1486.3 eV or Mg $K\alpha$ at 1253.6 eV) illuminate the sample and eject core electrons from atoms. These photoelectrons interact strongly with matter, hence the remarkable surface sensitivity. The kinetic energy of the ejected electrons depends on the energy

of the incident X-rays, the binding energy of the core electron, and the work function between the detector surface and the vacuum level.^{45,46} Equation 2 states the relevant dependency:

$$E_k = h\nu - E_b - \phi \quad (2)$$

One should note that the Fermi levels of the sample and spectrometer are aligned, so the work function of the sample surface is disregarded here and only the work function of the spectrometer is considered. The photoionized atoms follow two main pathways for relaxation to lower states. Upon creation of the electron hole in the core shell, an electron from a higher shell relaxes into the lower energy state. This may release a photon of equal energy, resulting in fluorescent photoemission of an X-ray photon, whereas the competing Auger process emits electrons alongside photoelectrons during an XPS measurements. These Auger electrons also result from deexcitation of photoionized atoms, but instead of emission of a photon, the relaxing electron induces ejection of a different electron from a higher shell, known as an Auger electron. They have element-specific kinetic energies that are *independent* of the energy of the illuminating X-rays. Transitions for the different electron shells give rise to a characteristic series of peaks for each element. Depending on the chemical bonding situation of an atom, the XPS peaks can be shifted towards higher or lower binding energies, which is referred to as *chemical shift*. The chemical environment can pull electron density from around the element atom and thereby increase the binding energy of the core electrons, or vice versa. A basic XPS setup consists of an X-ray gun that generates X-rays of a specific energy and an electron energy analyzer to count the electrons while scanning the energy. Comparison of the resulting spectra (peak position, peak shape, relative intensity) with reference measurements allows to identify several surface properties, such as the elemental composition, oxidation state and specific chemical compound.^{46,47}

2.4 UHV Systems

The experiments presented in this work rely on surface science tools of which several require the absence of an atmosphere. The main surface preparation to obtain ideal surfaces and the analytical methods to characterize them are combined in two ultra-high vacuum systems, the 'Bochum' system and the 'MOKE' system, both of which will be described in this section.

Figure 4 shows the multipurpose UHV 'Bochum' system ¹ which provides several tools for surface analysis. The base system is a commercially built configurable unit from SPECS Surface Nano Analysis GmbH. Unless stated otherwise, SPECS GmbH is also the vendor of the subsequently described components. The system is divided into six UHV chambers, with three main chambers and three auxiliaries, separated by gate valves. The former include a sample preparation chamber, analysis chamber, and SPM chamber. The auxiliary chambers include the loadlock chamber, distribution chamber and high-pressure reaction chamber. Pressures in (or close to) the UHV range are achieved by a pumping regime based on turbomolecular drag pumps (HiPace 80/300, Pfeiffer Vacuum), backed by dry scroll pumps (nXDS 6i/10i/15i, Edwards Vacuum). The three main chambers are also equipped with ion sublimation combination pumps (VacIon, Agilent), a combination of ion getter and titanium sublimation pumps. This setup provides ultimate pressures better than 2×10^{-10} mbar in the main chambers and better than 10^{-9} mbar in the auxiliary chambers. Due to regular venting, the pressure in the loadlock was usually in the 10^{-8} mbar range. The loadlock is a small chamber designed to quickly load and extract samples into/out of the system. It is fitted with a door that is sealed with a reusable viton gasket. Venting of the chamber with dry nitrogen (5N) facilitates fast pump-downs since less water vapor is introduced during the venting procedure. Directly attached to the loadlock is the distribution chamber with a six-slot sample storage.

The preparation chamber fulfills multiple roles. To clean the sample surface, argon ion bombardment is done here with the IQE 11/35, an extractor type ion

¹ The system is named after the location of its first installation at the Ruhr-University Bochum

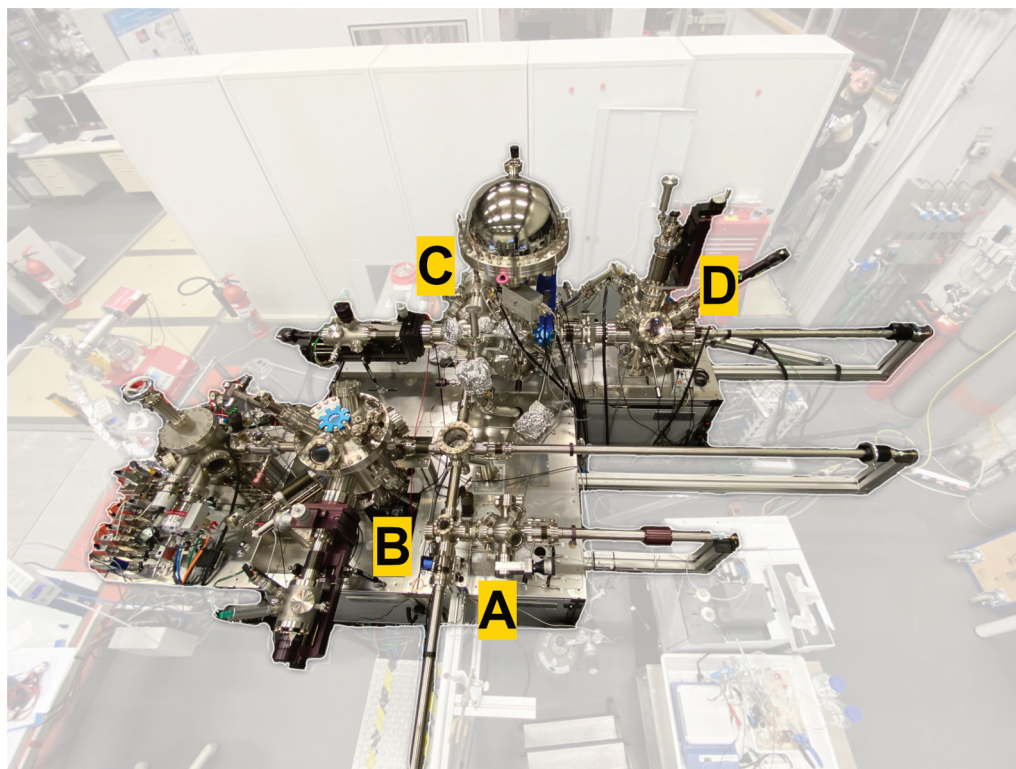


Figure 4: Photograph of the UHV system 1 'Bochum' . (A) Loadlock. (B) Preparation chamber (C) Analysis Chamber with XPS system (D) SPM Chamber.

source with direct gas feed via an attached leak valve. An electron beam heater is integrated into the manipulator head for sample annealing, where temperature monitoring is realized by a type-K thermocouple receptacle which touches an equivalent type-K thermocouple mounted on the sample holder. An MPS-ECR (mini microwave plasma cracker source) allows the generation of streams of atomic or ionized gas (oxygen/hydrogen or nitrogen) at pressures ranging from 10^{-6} mbar to 10^{-3} mbar. Currents resulting from ions hitting the sample can be measured over the ground of the manipulator.

Most analytical techniques are built into the analysis chamber; the hemispherical energy analyzer PHOIBOS 100 with MCD5 detector, in combination with an X-ray source XR 50M, enables XPS/AES, UPS, and ion spectroscopy in form of ISS and LEIS (in conjunction with an IQE 12/35). Notable extensions of the XPS capabilities are the FOCUS 500 monochromator and the EQ/FG flood gun. The XR 50M X-ray source has two anodes, aluminum and silver, installed

(corresponding to Al-K α and Ag-L α energies). A HIDEN HAL/3F residual gas analyzer is also located in the analysis chamber.

The UHV 'MOKE' system ² (figure 5) is in many aspects equivalent to the 'Bochum' UHV system, with a few key differences. A minor difference is the lack

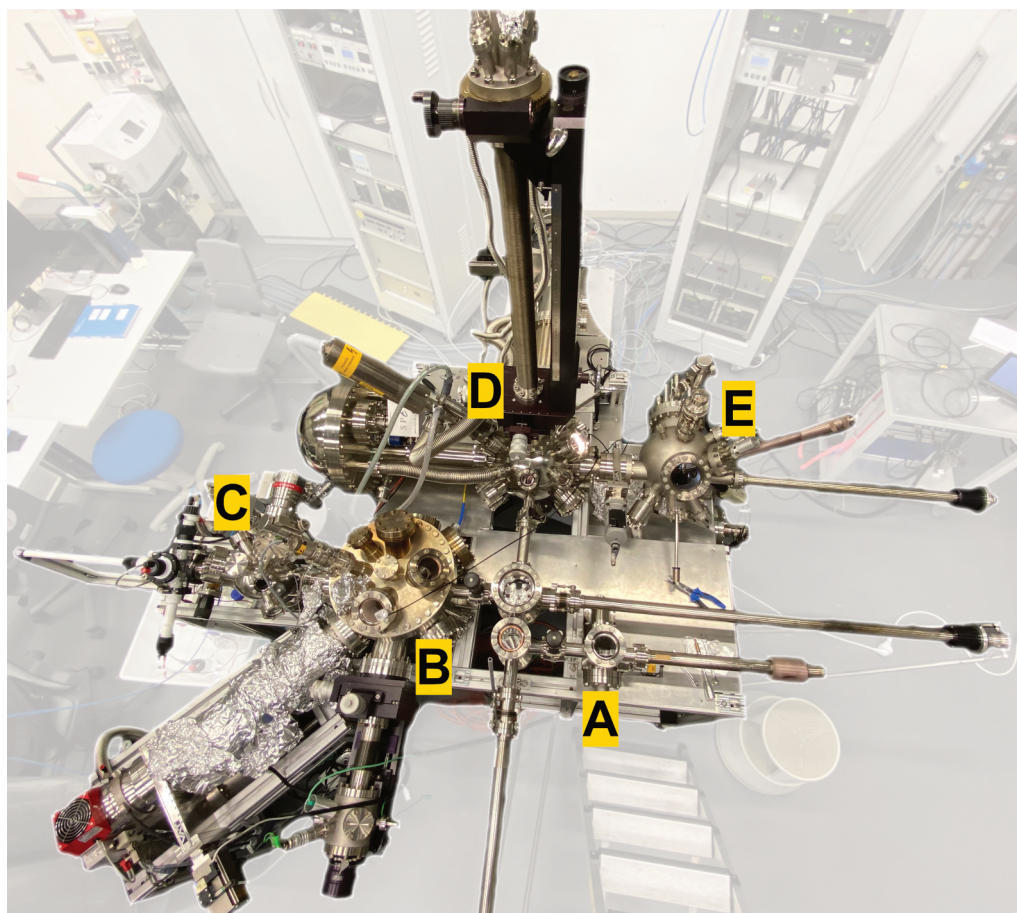


Figure 5: Photograph of the UHV system 2 'MOKE'. (A) Loadlock. (B) Preparation chamber (C) EC-Cell transfer/loadlock chamber (UHV) and inert gas chamber (glass) containing the EC cell proper (D) Analysis Chamber with XPS system (E) STM Chamber.

of a monochromator for the X-ray gun, along with a different set of anodes (Al and Mg instead of Ag). The system is not equipped with a high-pressure chamber; in its place, an arrangement for an electrochemical cell has been mounted, which is described in a separate section.

² The system is named after the facilities to measure the magneto-optic kerr effect, which it was equipped with in the past.

2.5 Single Crystal Preparation and Plasma Treatment

Single crystal samples were mounted on a stainless steel (V4A or 1.4401), double railed holder with a 'flag style' base plate compatible with the SPECS transfer rod heads, which makes it suitable for XPS and STM measurements. Figure 6 provides an overview of this homemade variant. Crystals were fixed with either screws and washers or two spot-welded tantalum strips. The double rail configuration allows to transfer flat crystals and access the sample surface, while still maintaining compatibility with the SPM by turning it over and using the upper rails to insert it into the SPM, keeping a safe distance between the sample surface and SPM stage. This holder was also used for EC experiments in the MOKE system and is compatible with the electrochemical cell described later. As mentioned, the preparation chamber is equipped with a sputter gun and

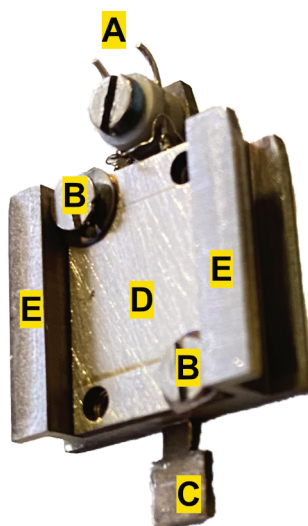


Figure 6: Double rail style sample holder for UHV experiments. **A:** Thermocouple contacts. **B:** Screws and washers to hold the sample. **C:** Holder head to lock and unlock the sample with the transfer rods. **D:** Sample base plate. **E:** Holder rails.

a manipulator with an e-beam heater for sample cleaning and annealing. The manipulator head is shown in detail in figure 7. When a sample holder is inserted into the clamps, heating is possible from the backside via e-beam, and a pair of K-type (Alumel and Chromel) thermocouple contacts on the sample holder and the manipulator head provide temperature feedback. Plasma treatment of

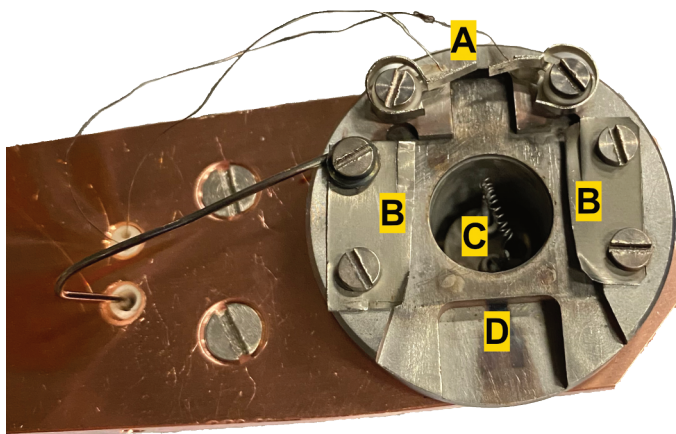


Figure 7: Detailed view of the manipulator head. **A:** Thermocouple contacts. **B:** Clamps. **C:** E-beam filament. **D:** Plate mount for the sample holder.

the sample surface with the MPS-ECR source was also done in the preparation chamber, where the plasma source is pointing upwards from the bottom of the chamber. The plasma is ignited inside the plasma crucible (Al_2O_3 for O_2 plasma) inside the tube (not visible), and guided through an accelerator grid into the chamber. Figure 8 shows a topview picture of the plasma source inside the chamber and its position relative to the manipulator head.

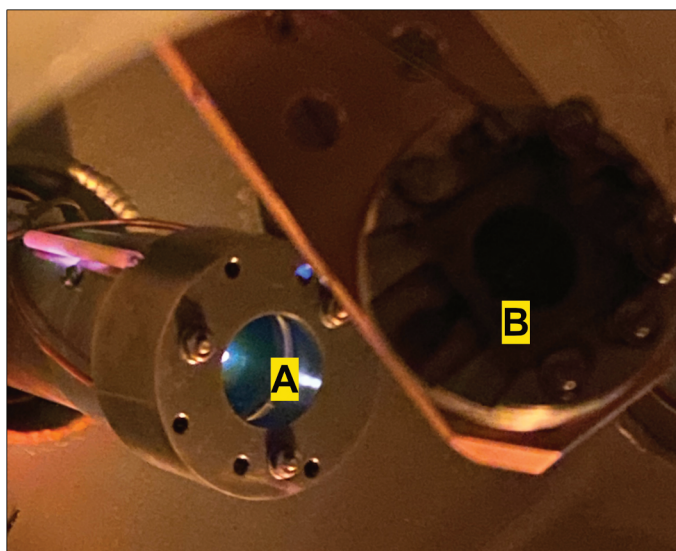


Figure 8: Plasma source inside preparation chamber with O_2 plasma ignited **A:** Plasma source exit with visible glow discharge. **B:** Manipulator head.

The sample, on the manipulator stage, can be moved into and out of the plasma stream and is facing away from the stream unless turned 180° .

2.6 Electrochemical experiments without air exposure

In UHV, a clean surface of a sample may be unaffected by contamination for several hours up to days, depending on the system's base pressure of residual gas. But in ambient conditions, it is always covered by layers of adsorbates, such as water. Since most metals are readily oxidized, this has the consequence that the surface is also chemically modified prior to an experiment. Considering that analytical methods that are done *after* an experiment look at the surface following another exposure to air, we can anticipate that the results might also be affected by this. Besides the development of true *operando* and *in-situ* techniques, partial improvements to current techniques can offer a compromise between ease-of-use, availability and 'value' of the results it delivers. We realized this with an electrochemical cell that is connected to our MOKE UHV system via a transfer chamber that prevents air exposure before and after an electrochemical experiment.

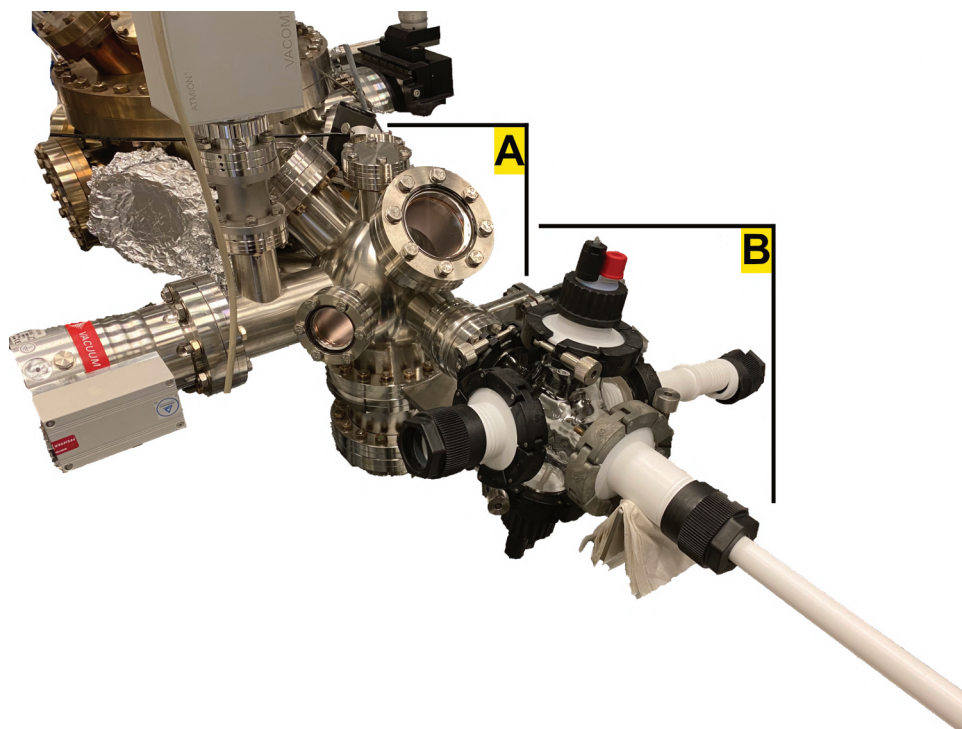


Figure 9: The EC-Cell side of the MOKE system. **A:** Loadlock chamber for the transfer of samples from the UHV side to EC side, and vice versa. **B:** Inert gas chamber interfacing the loadlock (UHV side) and EC cell. The EC cell itself is not attached here.

The MOKE system is equipped with a second loadlock, an inert-gas transfer chamber and an electrochemical cell. In combination, these allow the transfer of a sample from UHV to the electrochemical cell and vice-versa without exposing the sample to air.

The electrochemical cell consists of a PTFE tube with an open cone on one side which the sample is pressed upon during usage. The other side contains three ports on the short side and two on the long side. The latter are used to inject and extract electrolyte, while the former provide access for the counter and reference electrodes and the gas feed. The electrode setup is laid out for a three electrode configuration, with a platinum mesh counter electrode (CE) and a leak-free Ag/AgCl (3M KCl) reference electrode (RE). The sample acts as the working electrode; it is mounted on a metallic sample holder, which in turn is connected by a wire which runs through the otherwise isolated PTFE stamp that presses against the aforementioned cone. Figure 9 shows the cell arrangement in practice. The electrochemical procedures were controlled with a Metrohm Autolab potentiostat.

The EC-cell and the stamp are mounted in a large glass chamber. This chamber can be continuously purged with argon and has a septum on the top port to inject liquids for rinsing after an electrochemistry experiment. An orthogonally mounted PTFE transfer rod is used to carry a sample to or from the loadlock. The choice of PTFE as the main material here arises from its ability to make a gas-tight seal while still allowing sliding (due to the low friction coefficient) and its compatibility with many chemicals.

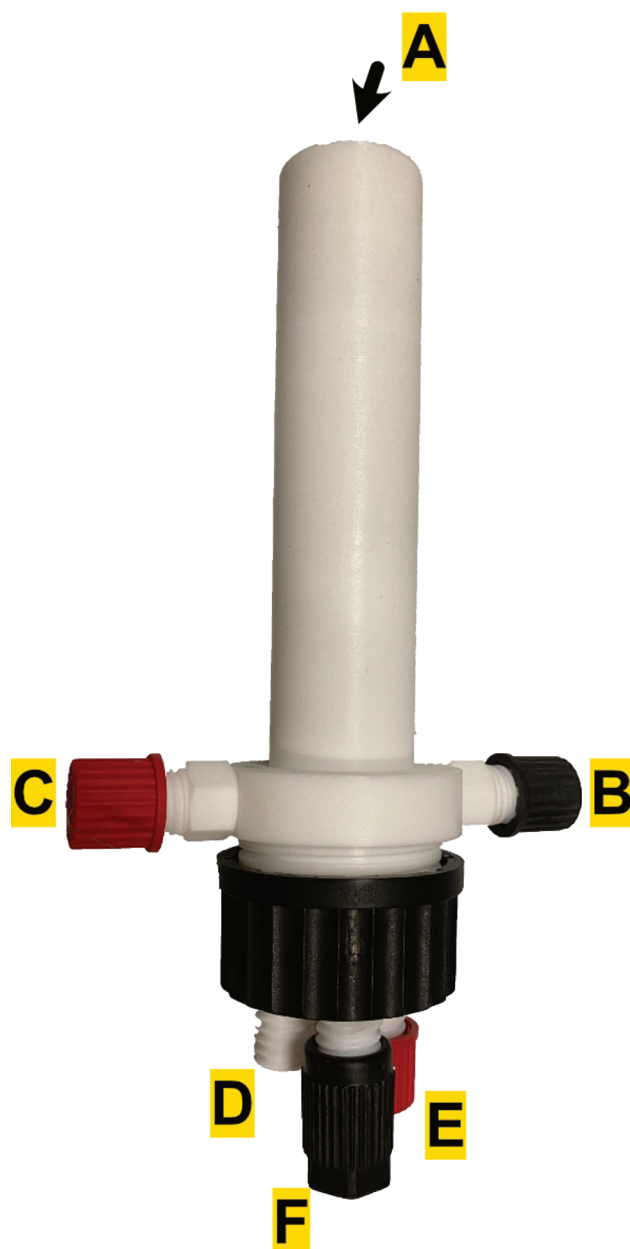


Figure 10: Vertical view of the EC-cell. **A:** Cell opening towards the sample side. **B:** Drain for electrolyte. **C:** Counter electrode (CE), Pt-mesh. **D:** Gas-in. **E:** Reference electrode (RE), Ag/AgCl (3M KCl). **F:** Gas-out.

2.7 Nuclear Resonant Inelastic X-ray Spectroscopy (NRIXS)

Nuclear resonant inelastic X-ray spectroscopy (NRIXS) is a nuclear vibrational spectroscopy method that is selective for Mössbauer-active isotopes, especially ^{57}Fe . It is also known as Nuclear Resonant Vibrational Spectroscopy (NRVS).⁴⁸ One of the main strengths of this method is the isotope selectivity combined with access to lattice vibrations and thermodynamic properties in extreme environments such as high-pressure, high-temperature and diverse matrices.^{49,50} NRIXS shares a relationship to Mössbauer spectroscopy similar to that of Raman spectroscopy to infrared spectroscopy, i.e. NRIXS probes the inelastic components (phonon annihilation and creation) besides the elastic main peak in Mössbauer spectroscopy. At the heart of this technique is a unique approach to X-ray scattering relying on the separation of nuclear and electronic contributions to X-ray scattering. It is only possible for select isotopes, for reasons that can be explained by considering the interactions between photons and atomic nuclei, and the lifetime of the excited nuclei.

The Thomson model (equation 3, given in cgs units) assumes a point charge q with mass m and yields the interaction cross section σ_T of a photon interacting with that point charge:

$$\sigma_T = \frac{8\pi}{3} \left(\frac{q^2}{mc^2} \right)^2 \quad (3)$$

where c is the speed of light.

It can be used as an approximation of the X-ray scattering cross section of an atom with the atomic number Z . An atom's X-ray scattering cross section depends mainly on the photon interaction with the electron shell, since the contribution from its nucleus, σ_N , is smaller by a factor of $(Zm/M)^2$, which is a reduction by a power of 10^7 .

Exceptions to this are found for certain isotopes. The nuclei of those that are Mössbauer active exhibit resonant excitations upon interaction with X-rays, which leads to a greatly increased nuclear scattering cross section; in the case of

^{57}Fe , the factor $\frac{\sigma_N}{\sigma_T}$ is roughly 5700. The excitation of nuclear vibrations for ^{57}Fe requires an incident X-ray energy of 14.4125 keV, and is only possible if the energy of the irradiating X-rays is within several hundred neV of this value, since the off-resonance cross section σ_N is magnitudes lower for even very small deviations from the exact value. This requires to use synchrotron facilities to achieve the high energy and energy resolution required to perform an experiment.⁵⁰

Unfortunately, despite the resonance effect enhancing the nuclear vibrations, the electronic signal is still more intense and drowns out the signal from the nuclear relaxation. Fortunately, the nuclear vibrational levels differ significantly from their electronic counterparts in terms of energy width Γ and lifetime τ of an excited state Λ . Equation 4 shows their inverse relationship.

$$\tau(\Lambda) = \frac{\hbar}{\Gamma} \quad (4)$$

The energy width of the nuclear resonance is only $\gamma=4.66$ neV, and the corresponding lifetime of the excitation is $\tau = 141$ ns. Since the lifetime of the electronic excitation is far shorter (nanoseconds), they (electronic and nuclear excitation) are separated in the time domain. It is thereby possible to distinguish the vibrational origin of the emitted photons, nuclear or electronic, by time discrimination.⁵⁰

Figure 11 outlines how this theoretical description is implemented experimentally. The synchrotron beam is pulsed in very short bursts which are highly monochromated to achieve 1 meV energy resolution at 14.4125 keV, which is then used to irradiate the sample. After a pulse has ended, the detector (an avalanche photodiode) records the emitted fluorescence photons. With appropriate time resolution, fluorescence from the nuclear relaxation and electronic relaxation events are then separated.

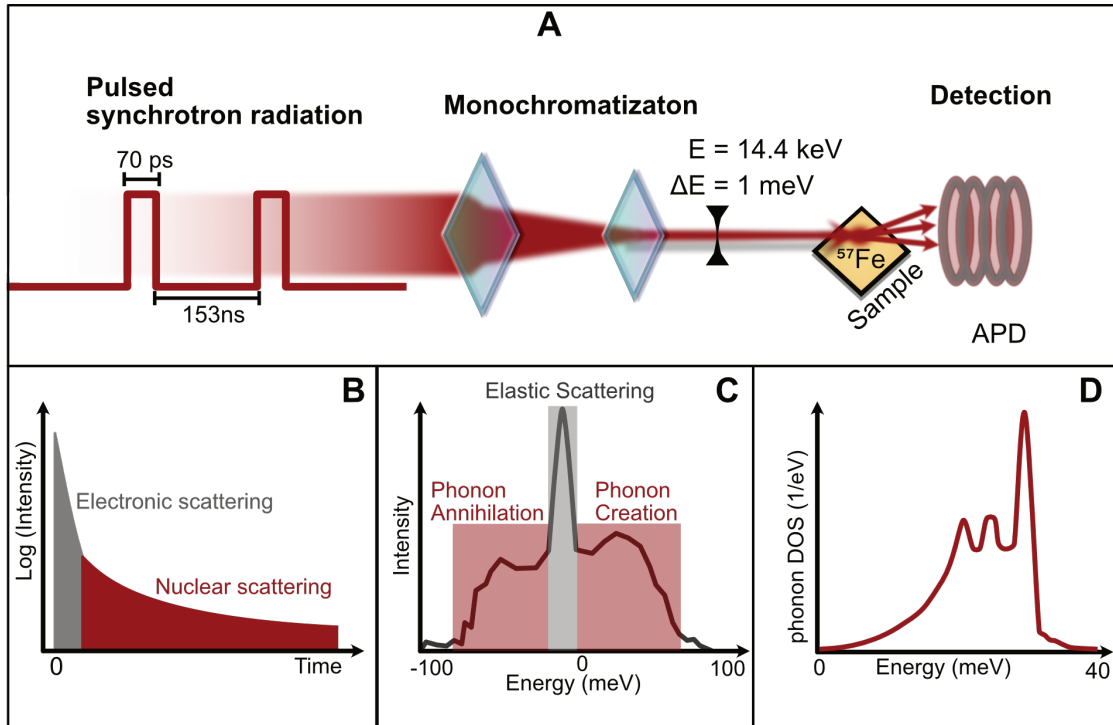


Figure 11: Schematic of an NRIXS experiment: **(A)**: The synchrotron radiation is pulsed in bunches of 70 ps width with a separation of 153 ns. **Monochromatization**: A series of monochromators cuts the energy distribution in the incoming beam down to 1 meV, focused around the main excitation energy for ^{57}Fe , 14.41 keV. **Detection**: An avalanche photodiode detects the fluorescence response after the sample is irradiated. **(B)**: Electronic and nuclear scattering intensities on a timescale. At $t = 0$, a pulse of synchrotron radiation excites the sample. Electron relaxation is immediate when compared to the nuclear response, which enables separation of electronic and nuclear contributions. **(C)**: The raw NRIXS spectrum contains the elastic center peak (from the Mössbauer effect) and the inelastic side bands, which can be interpreted as phonon annihilation and creation. Similar to the Stokes and Anti-Stokes bands in Raman spectroscopy, the phonon creation contributes slightly more intensity. **(D)**: The (partial) phonon density of states can be extracted from the raw spectrum.

It is evident that the data acquired are correlated to the vibrations of the nuclei in a material. The elastic component of the photon-phonon interactions gives rise to the Mössbauer peak, with red-shifted and blue-shifted signals accompanying it. These shoulder bands can be thought of as the result of inelastic interactions of

the photons with phonons, either due to phonon creation or phonon annihilation. Removing the Mössbauer peak from the spectrum results in a spectrum of the inelastic scattering, which can be transformed to the projected phonon density of states (PDOS) in case of solid materials. Many thermodynamic properties are linked to the phonon density of states, such as sound velocity and temperature, and can therefore be deduced from an NRIXS spectrum.⁵¹

2.8 X-ray Absorption Fine Structure Spectroscopy (XAFS)

As mentioned, X-ray spectroscopy probes the excitation of an electron to a higher energy state through the interactions between incident X-ray photons and electrons. In the case of X-ray absorption, all the energy of incident photons is transferred to electron excitation. The absorption can be described using the Lambert-Beer law (equation 5):

$$\mu = -\frac{d \ln I}{dz} \quad (5)$$

Here, μ is the *linear absorption coefficient*, I the intensity of the X-rays and z the thickness of the sample. The absorption coefficient depends strongly on the energy of incident X-rays. In the case of X-ray absorption by core-level electrons, the contributions of different core levels to X-ray absorption are well-separated.⁴⁷ A typical X-ray absorption spectrum (the dependency of the absorption coefficient on X-ray energy) corresponding to such a situation is shown in figure 12.

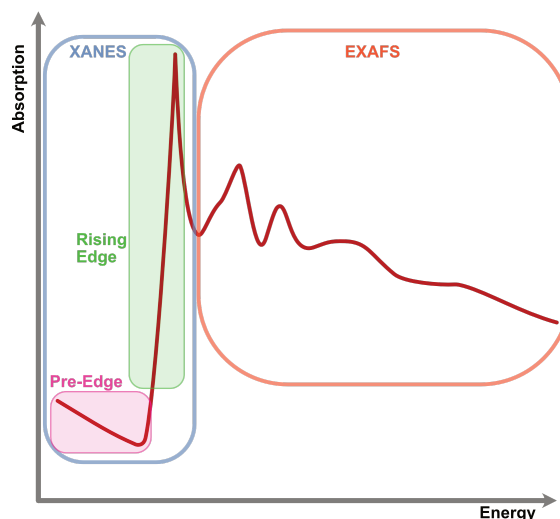


Figure 12: Different regions in an unnormalized X-ray absorption (XAS) spectrum.

The sharp first peak relates to the *absorption edge*, which corresponds to the excitation of core electrons to the available unoccupied states. The region before (*pre-edge*) and at the absorption edge (*rising edge*) are part of the so-called XANES region. XANES stands for X-ray absorption near edge structure and is also called near edge X-ray absorption fine structure or NEXAFS. The subsequent oscillations after this near edge region is part of the extended X-ray absorption fine structure (EXAFS), which starts at about 30 eV beyond the edge.^{47,52} The oscillations are a result of the interaction between the electrons, excited to delocalized states, and electrostatic potentials of neighboring atoms. In the commonly used approach, these interactions are described as a scattering of excited electron from the neighboring atoms, resulting in modulations of the wave function for the excited electron state, and, hence, changes in absorption probability. The frequency and amplitude of the EXAFS oscillations are therefore sensitive to the details of local structure. Modeling of a local environment and calculation of the resulting scattering paths enables the extraction of several physical properties of an analyzed sample; most notably, the coordination number and interatomic distances in a material can be deduced. From the XANES region on the other hand, the chemical state of the absorbing atom can be identified. Owing to the comparatively high penetration depth of X-rays as opposed to electrons,

XAFS measurements allow to collect information about the bulk structure and composition of a material rather than being limited to the surface, as is the case in XPS and AES. It is also possible to perform measurements in diverse environments, solid, gaseous or liquid.^{47,52,53} However, the prerequisite for XAFS techniques is a highly tunable and intense X-ray source with a high flux, which means that these experiments are normally limited to synchrotron facilities.

2.9 Synchrotron Setup for Spectroelectrochemistry

The ec-cell in use for spectroelectrochemical XAS and NRIXS is made of a polyacrylic glass and provides a detachable vertical window frame where the sample, a carbon paper disc, can be mounted with a KaptonTM tape, as well as access for gas feeds and counter and reference electrodes (Pt-mesh and leak-free Ag/AgCl (3M KCl), respectively). Figure 13 shows a schematic of this cell design.

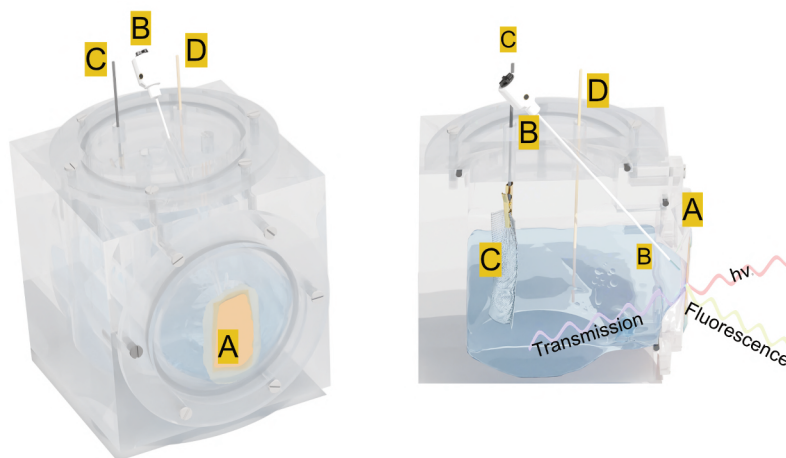


Figure 13: Schematic of the acrylic electrochemical cell for operando XAFS and NRIXS measurements. It is configured for a three electrode setup with the sample as the working electrode (A), a leak-free Ag/AgCl (3M KCl) reference electrode B and a platinum mesh counter electrode C. A gas inlet is located on the top side (D). **Right:** Configuration of the cell in relation to the beam during measurement. This cell is designed for fluorescence mode operation, where the sample is irradiated from the backside and the fluorescence is detected. Cell image made by Philipp Grosse.

During the measurement, the incident beam penetrates the sample from the backside, while the cell is at an angle with respect to the detector and beam, so the fluorescent emission can be recorded.

2.10 Nanoparticle Synthesis

Micelles are surfactant assemblies of molecules with hydrophilic and hydrophobic groups on opposite ends of the molecule, leading to a typical arrangement in water, where the hydrophobic groups point to the inside of the assembly and the hydrophilic groups form an outwards facing layer. Accordingly, the assembly is inversed in non-polar solvents, and the inner assembly is mostly comprised of hydrophilic groups. A bottom-up synthesis method to form nanoparticles of metal salts is using these inversed micelles, in what is called *inverse micelle encapsulation*. Here, metal salts, which are polar, are mixed with a block co-polymer (poly(styrene-*b*-vinyl-pyridine)) with polar head and non-polar tail groups in a non-polar solvent such as toluene. This mixture self-assembles, and forms nanocapsules of metal salt inside inverse micelles. The micelle solution can be used to apply a monolayer of micelles on a substrate via several coating methods, in this case via dip coating. At slow dip-coating speeds, only a monolayer of micelles is attached to the substrate, and the distance between the micelles is determined by the length of the non-polar polymer tail. The polymer shells around the metal salts can be removed by plasma treatment, and free standing nanoparticles containing the metal salt are now left patterned on the substrate surface. The size of the nanoparticles is determined by the size of the micelle head groups and the amount ('loading') of metal salt in relation to polymer. Figure 14 outlines the procedure. The preparation of samples for electrochemical measurements included the dip coating of glassy carbon electrodes with the nanoparticle solution, which was done with a simple dip coater with a step motor. The removal of the involved polymers was based on plasma treatments in an *SPI Plasma Prep III* plasma etcher. This device is a compact plasma etcher with dual-gas feed (O_2 and N_2) for radio frequency plasmas at pressures at about 0.5 mbar.

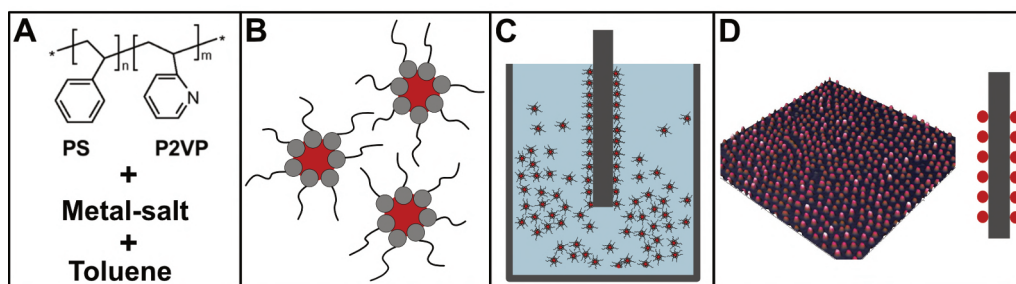


Figure 14: Nanoparticle synthesis via inverse micelle encapsulation and subsequent preparation of a monolayer of free standing nanoparticles on a substrate. **A:** Mixing of polymer and metal salt in toluene. **B:** Formation of inverse micelles. **C:** Dip coating, with inverse micelles attaching to the substrate. **D:** Free standing nanoparticles after removal of the polymer shell.

2.11 Low Energy Electron Diffraction (LEED)

Depending on the energy, electrons undergo different interactions with a sample surface, such as absorption or inelastic scattering. Specifically, electrons at relatively low kinetic energies (20 eV to 300 eV) have a high cross-section in regards to elastic backscattering. In a low energy electron diffraction (LEED) experiment, a collimated electron beam is projected onto a sample surface (oriented to the surface normal), and the diffraction pattern is detected and visualized by a fluorescent screen, preceded by an arrangement of retarding grids that act as a ground and filter out electrons with deviating energies.^{47,54} The diffraction pattern is a consequence of interference of electron waves satisfying the Bragg condition of scattering at solid surfaces:

$$a \sin \theta = n\lambda \quad (6)$$

Here, a is the lattice parameter, λ the wavelength of the electrons and θ the angle of the backscattered wave to the incident wave. To understand the spot intensity in LEED, one has to consider the reciprocal lattice of the investigated sample. The reciprocal lattice of a 2D surface can be described as 'rods' in the place of the 2D lattice points. Lattice vectors parallel to the surface do not contribute to the spot intensity, since they do not satisfy diffraction conditions. The LEED

pattern is thus an image of the reciprocal lattice of the surface region from the view of the surface normal (as viewed from the electron gun). Qualitatively, the real space periodicity and point group of the surface can be concluded from this. This is especially interesting when the surface is reconstructed from the expected structure of the bulk material.

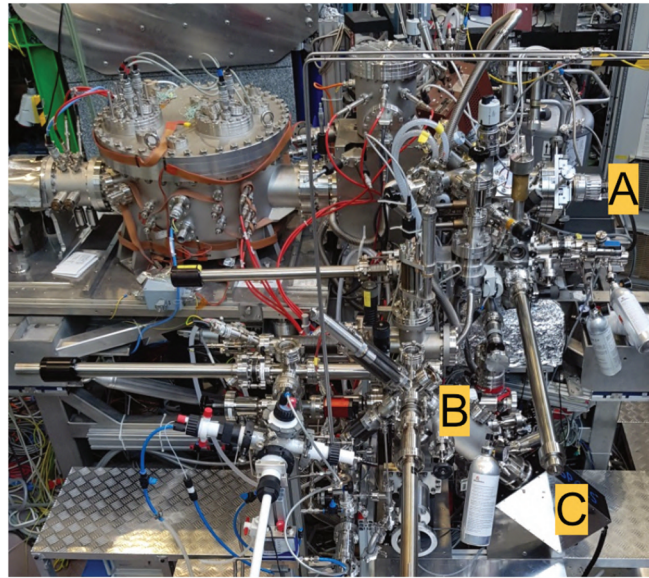
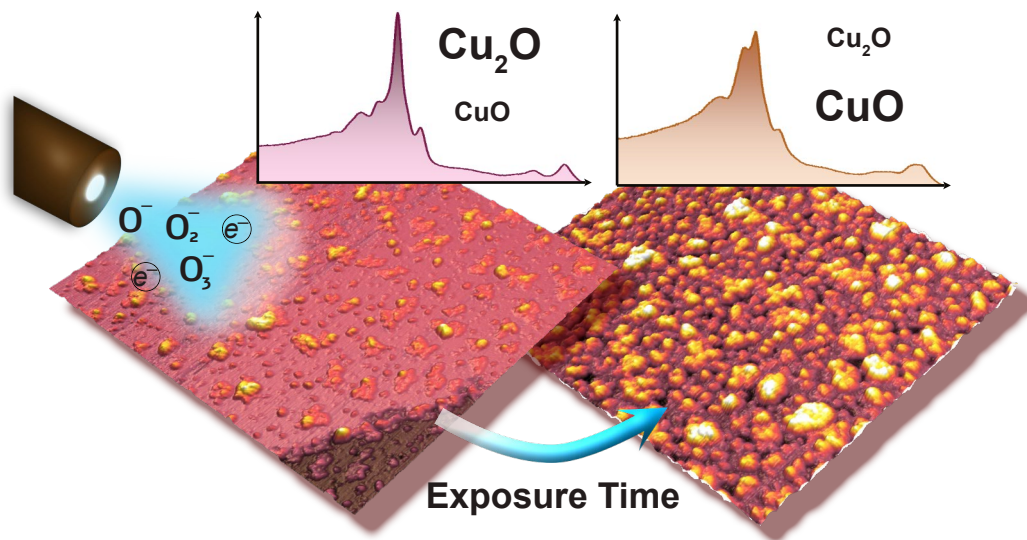


Figure 15: SMART microscope at the BESSY II synchrotron. **A:** Specimen analysis chamber. **B:** Preparation chamber with the attached MPS plasma source **C:**

The LEED measurements presented in this work have been performed at the UE49PGM undulator beamline of the BESSY II synchrotron light source, specifically in the SMART LEEM/XPEEM microscope shown in figure 15.

Chapter 3

Plasma-assisted Oxidation of Cu(100) and Cu(111)



3 Plasma-assisted oxidation of Cu(111) and Cu(100)

The content of this chapter consists of material intended to be published in the immediate future. Changes to the structure and additions were made to better fit within the scope of this thesis. This includes the addition of content from the supporting information at the appropriate places and a short introductory paragraph. The experiments at the SMART LEEM/XPEEM microscope at the BESSY II synchrotron (LEED, NEXAFS) were done by L. Tanase, M. Prieto, L. Caldas de Suza, P. Grosse, F. Scholten and T. Schmidt. Data analysis of the obtained LEED and NEXAFS data was done by L. Tanase and T. Schmidt, the growth model was made by T. Schmidt.

3.1 Introduction

Copper has a long history of industrial applications in metallurgy, construction and electronics. Due to its wide spread use, insights into the oxidation dynamics of copper are interesting for various science and technology fields. The main oxides of copper, Cu_2O and CuO , are both p-type semiconductors and are themselves investigated for their application in solar cells^{55,56} and as photocatalysts.^{57,58} Furthermore, copper has unique properties that make it suitable for use as a catalyst in the electrochemical conversion of CO_2 (CO_2RR) to multicarbon products, such as ethylene.²⁵ Several studies have shown that oxidizing the copper surfaces can enhance the catalytic activity and selectivity towards certain products.

Electrochemical oxidation is often utilized for its morphology-altering capabilities to obtain rough surfaces in the form of oxide-derived copper (OD copper).^{59–61} Our group has also shown that treatment of copper foils with an oxygen plasma results in lower overpotential and enhanced selectivity towards ethylene.^{62,63} The origin of the enhanced catalytic properties of OD-Copper is thought to lie in morphological transformations underwent by the pre-oxidized Cu surfaces during the reducing CO₂RR conditions, as well as to the presence of resilient Cu(I) species that might remain at/near the surface during reaction.^{64,65} In fact, the coexistence of Cu(0)/Cu(I) species during CO₂RR has been recently achieved through pulsed electrochemical treatments and shown to open up a new and highly selective route towards ethanol generation.⁶⁶

Understanding how the oxide formation can be controlled and tuned is therefore a desirable goal for further research into efficient catalysts and energy materials. However, the complex nature of the processes involved has not yet been unravelled to a sufficient degree.⁶⁷ In ultra-high vacuum, copper surfaces remain unreconstructed for an extended duration. The initial oxidation, on an atomic scale and under low oxygen pressures, depends on the orientation of the surface plane. On Cu(100), it has been shown that chemisorbed oxygen induces reconstructions of the surface even at low coverages.^{68–70} On the Cu(111) surface, ordered structures have not been reported at low oxygen coverages, while hexagonal overlayers have been identified for higher coverages.^{71–73} The formation of reconstructed O/Cu(111) surfaces by exposure to molecular oxygen requires higher temperatures, leading to several reconstructions, notably the ‘29’ and ‘44’ reconstructions.^{74,75} Owing to the requirement of flat surfaces, studies on the oxidized surface at the atomic scale utilized either very low oxygen exposures, high temperature oxidation (inducing reconstruction) or bulk Cu₂O single crystals. This also lead to a lack of studies in the range between the initial oxide growth and later stages of oxide film growth, with only few studies tracking the propagation of the oxide growth over time.^{76,77}

Notably absent from fundamental studies is the oxidation at room temperature via exposure to an oxygen plasma. Little research has been done on the

morphology of such oxidized surfaces besides the identification of increased surface roughness.⁷⁸ One of the most appealing aspects to use a plasma is the possibility that it offers the decoupling of the oxidation process from elevated temperatures (thermal oxidation)⁷⁵ and chemically compromising environments (electrooxidation). Here, we investigate the oxidation of Cu(111) and Cu(100) single crystal surfaces with a low-pressure oxygen plasma at room temperature (RT). We applied a comprehensive suite of complementary microscopic (STM, LEEM), spectroscopic (XPS, NEXAFS) and diffraction (LEED) techniques to study the growth dependencies in regards to the exposure and surface orientation as a first step towards a deeper understanding of plasma-modified surfaces.

3.2 Experimental details

The experiments were performed in two separate UHV systems (called 'STM/XPS system'¹ and 'LEEM/XPEEM' in the following) and with two sets of single crystals. Both UHV systems have a base pressure in the low 10^{-10} mbar range. The STM/XPS system is the UHV system 1 which is described in the methods chapter. STM was done with an etched tungsten tip, and a monochromated Al-K α radiation source (1486.6 eV) was used for XPS. Low energy electron diffraction/microscopy (LEED/LEEM) and near edge X-ray absorption fine structure (NEXAFS) were done in the LEEM/XPEEM (SMART) microscope operating at the UE49PGM undulator beamline of the BESSY II synchrotron light source at the Helmholtz Centre Berlin (HZB). The aberration corrected and energy filtered LEEM-XPEEM system achieves a lateral resolution of 2.6 nm in LEEM mode.^{79,80} Both systems were equipped with a commercial microwave plasma cracker sources (MPS-ECR-HO, SPECS GmbH), which were used to direct streams of oxygen ions at low pressures ranging from 10^{-5} mbar to 10^{-4} mbar towards the sample. The plasma sources were mounted in UHV chambers separated by gate valves from the analysis chambers to avoid background oxygen during the subsequent surface analysis measurements. Copper single crystals with (111) and (100) orientations (from MTI Corporation, and MaTeck) were prepared by successive cycles of sputtering with Ar⁺ ions (10^{-5} mbar) and annealing at 880 K

¹ Corresponds to the Bochum UHV system outlined in the previous chapter

until clean and flat surfaces were obtained. Before plasma exposure, the samples were cooled down to room temperature (RT) to avoid thermal oxidation. The plasma treatments and subsequent measurements were done in a sequential fashion. A sequence consisted of two steps. First, a sample was exposed to the plasma for a set amount of time. Subsequently, it was transferred to the analysis chamber (within UHV) and characterized. This order was then repeated in the next sequences without any intermediate cleaning or annealing processes. Consequently, the plasma exposure is cumulative and the sum of all treatments carried out before. The plasma sources were operated at an oxygen pressure range of $pO_2 = 3 \times 10^{-5}$ mbar in the STM/XPS system and at a slightly higher $pO_2 = 4 \times 10^{-4}$ mbar in the LEEM/XPEEM due to the different geometry of both experimental systems. The sample was placed about 100 mm - 150 mm in front of the plasma source. We used anode voltages of 400 V - 500 V, roughly translating to the kinetic energy of the extracted ions. While LEED, XPS and NEXAFS were done after each sequence for the entire plasma treatment, image acquisition with STM was done until the measurements became increasingly difficult due to the reduced surface conductivity and growing surface roughening. We used the Gwyddion and WSxM software packages for image analysis of the STM data, and CasaXPS for the analysis of the XPS spectra.^{81,82}

3.3 Results and Discussion

3.3.1 Morphology

The morphological changes after sequential plasma treatments have been investigated using LEEM and STM in the two different setups. While STM allows resolving the surface in greater detail and with relevant sensitivity in height, LEEM favours the visualization of larger areas. Fig. 16 shows a series of STM images, starting from the clean Cu(100) and Cu(111) surfaces, after successive plasma exposure of 30 s at each sequence. Clearly, island growth sets in after the first treatment. The stepped structure of the surfaces is however retained as we can find steps in several images. We can therefore conclude that the plasma treatment is mild enough not to result in destructive changes on a scale beyond the surface structure. The oxide island coverage increases with each sequence,

and qualitatively it is obvious that the island growth and nucleation progresses faster on the Cu(111) surface as compared to Cu(100).

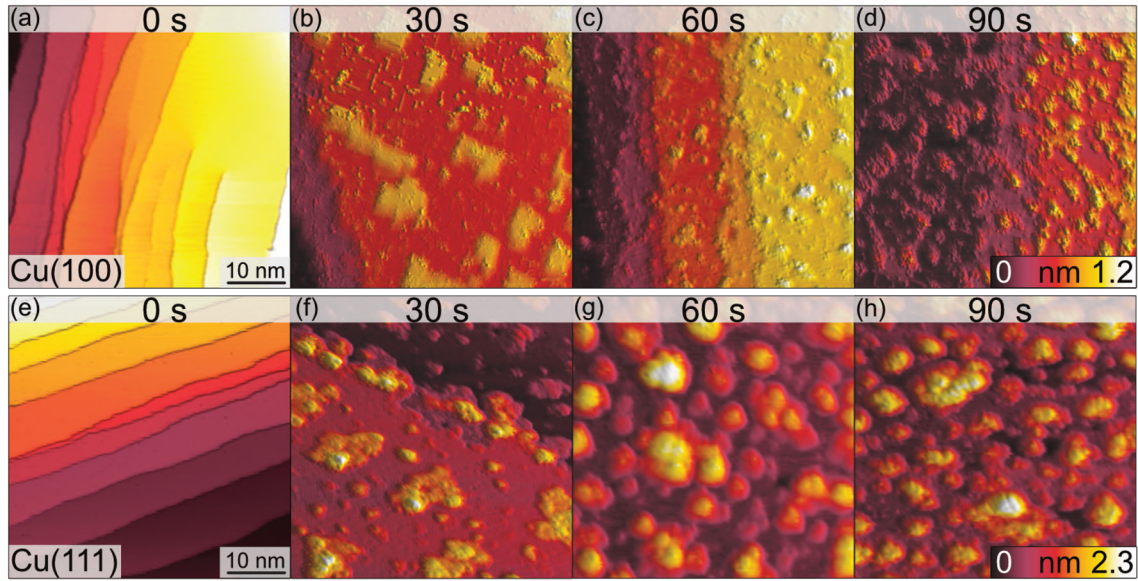


Figure 16: STM images of the clean (0 s) Cu(100) (a-d) and Cu(111) (e-h) surfaces and those after the initial oxide growth following the exposure to an O_2 -plasma at RT, 3×10^{-5} mbar for the times indicated. The lateral sizes of all images are 50 nm x 50 nm. The height scales are cut off at 1.2 nm and 2.3 nm to equalize each tile. Imaging parameters for a-d: $U = -0.6$ V to -1.5 V, $I_t = 115$ pA - 222 pA. Imaging parameters for e-h: $U = -1.5$ V, $I_t = 155$ pA - 289 pA.

Figure 17 shows a detailed view of the Cu(100) and Cu(111) surfaces after the initial 30 s plasma exposure. In figure 17 (a), four distinct features are visible. Rectangular islands (green square) of monoatomic height and stripe-like structures (arrow) following the (100) surface structure. The surface, including the rectangular islands, is also covered in part by small adsorbate clusters (green circles). The clean, flat substrate (green triangle) resembles a missing-row (MR) reconstruction which resembles a known O/Cu system following oxygen exposure.⁸³ We can identify a ladder-type contrast⁸⁴ as shown in figure 17 (b). We find larger numbers of the small clusters nucleated at ad-islands. It has been reported that the edge and corner sites of the ad-islands are preferential nucleation sites for oxide islands.^{68,69} This is more apparent in the 120 s image in figure 18 (a). For this greater exposure, numerous oxide clusters (green circle)

are covering the surface in conjunction with the stripes (arrows) and rectangular islands (green square). However, the substrate structure itself is seemingly still intact, and the stepped surface structure is retained.

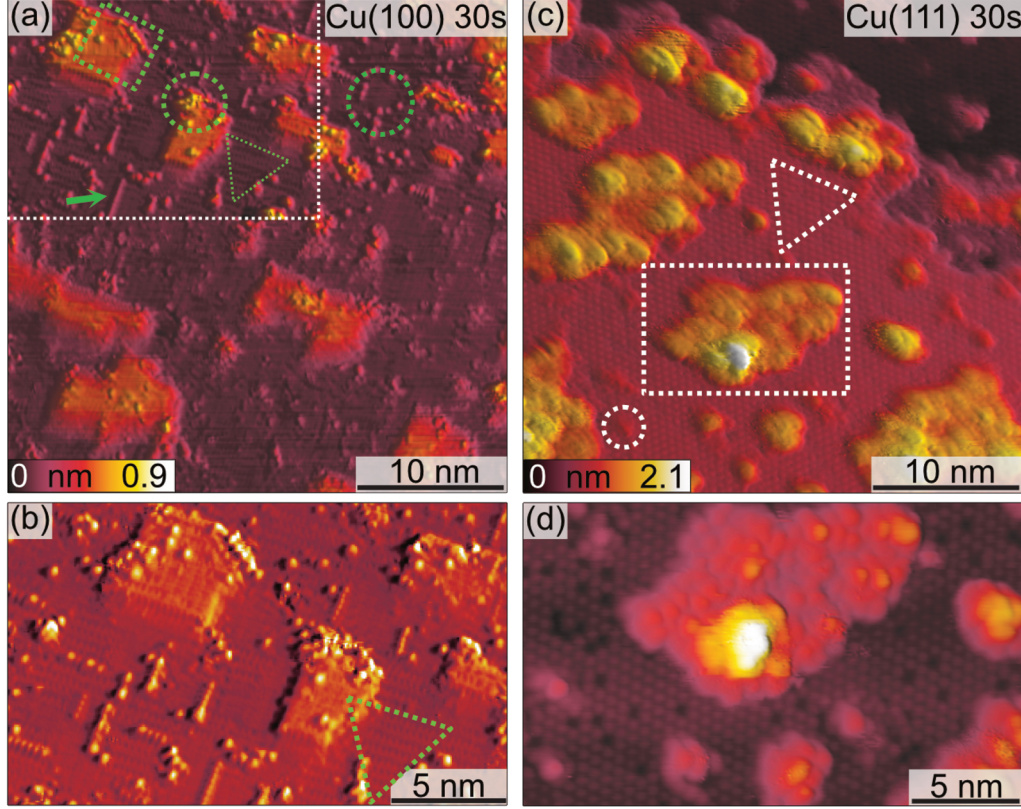


Figure 17: STM images of the (a,b) Cu(100) and (c,d) Cu(111) surfaces after 30 s plasma exposure at RT, 3×10^{-5} mbar O_2 . (a) Overview of Cu(100). (b) Area marked with the white rectangle in (a). Imaging parameters $U = -0.6$ V to -0.6 V, $I_t = 155$ pA. (c) Overview of Cu(111) and (d) zoom on the area around the island marked with the white rectangle in (c). Imaging parameters: $U = -0.9$ V, $I_t = 115$ pA. Green and white markers highlight key features of the surface morphology.

In comparison, on Cu(111), we did not observe similar preferred nucleation sites. The Cu(111) surface after 30 s of plasma exposure is shown in figure 17(c,d). From the larger scale STM image in figure 17(c) it is clear that the coexistence of flat, reconstructed substrate and islands is shifted towards islands on the (111) orientation. The islands can be classified into three types, the first being larger, disordered structures (white rectangle in figure 17(c)), which are accompanied

by two types of smaller islands (white circles). The islands are not limited to monolayer height, but appear to have grown immediately three dimensionally. The substrate appears to be reconstructed as $\text{Cu}_2\text{O}(111)$ -like (white triangle), as shown in figure 17(d).⁸⁵⁻⁸⁷ Typical etching along the step edges is seen, which is known to occur on $\text{Cu}(111)$ during oxidation.⁸⁸ Curiously, ordered surface reconstructions have been described upon thermal treatments,⁷⁵ whereas at RT and lower dosages, unordered surfaces have been reported,^{67,71} but we see them here in combination with disordered structures and etched steps from the initial oxide growth. Analogous to $\text{Cu}(100)$, further sequences of plasma exposure result in a $\text{Cu}(111)$ surface that is covered by more islands, with increasing density and height, as is evident from figure 18 (b). Still, flat areas between islands remain intact. This wetting behaviour is also observed for the (100) orientation.

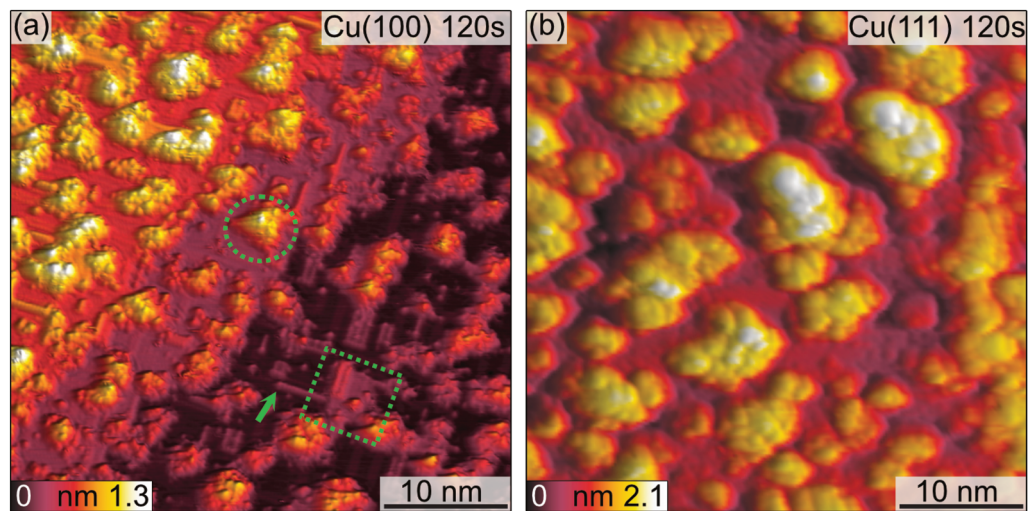


Figure 18: STM images of the (a) $\text{Cu}(100)$ and (b) $\text{Cu}(111)$ surface after 120 s plasma exposure at RT and 3×10^{-5} mbar. In (a), marked with green shapes are key features discussed in the text. Imaging parameters: (a) $U = -0.9$ V, $I_t = 155$ pA (b) $U = -1.5$ V, $I_t = 115$ pA

Because of the nature of the plasma, it is reasonable to expect a high reactivity of the impinging oxygen ions. Assuming immediate reaction upon impact, one could expect a randomly dispersed oxygen distribution. One would also expect similar evolution of Cu_2O and CuO for both orientations. Our observations

from STM and XPS contradict this, and we interpret the differences in the copper oxide formation and evolution as a result of the thermalization of the impinging oxygen ions, rather than immediate reaction. Thermalization and the accompanying diffusion processes of oxygen and copper atoms offer an explanation for the continued island growth after the first sequences, and also for the orientation-dependent copper oxide formation. For similar O₂-plasma exposures, the average island height on the (111) surface is higher than on the (100) surface. The observation of flat inter-insular areas is made over the entire range of STM measurements. Figure 19 shows line scans across islands after dosing for 30 s and 120 s, respectively.

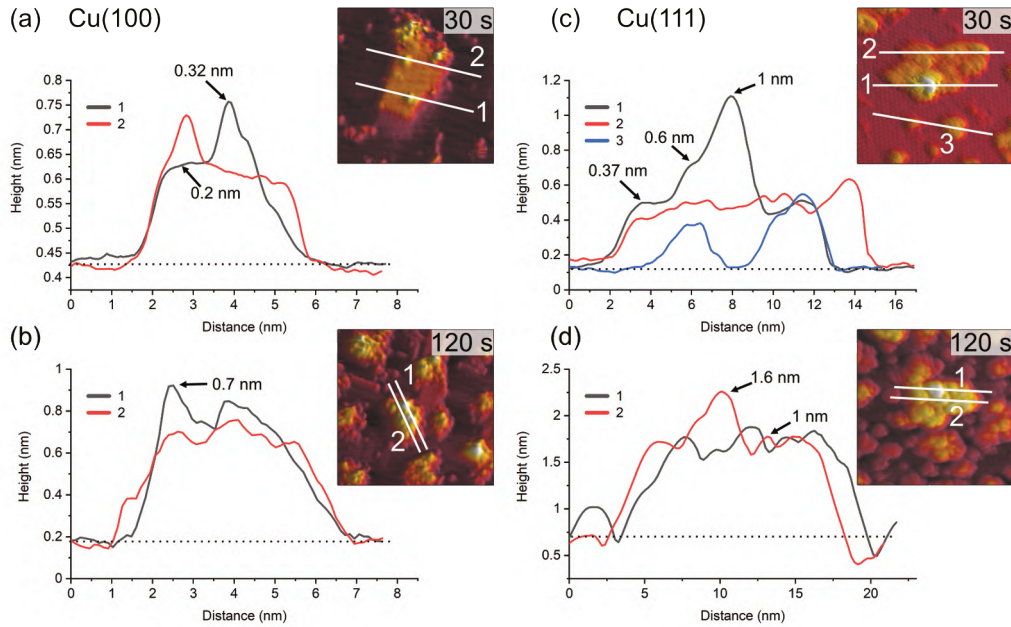


Figure 19: Profiles of line scans on the islands shown in figures 16 and 18 for 30 s and 120 s plasma exposure at RT and 3×10^{-5} mbar O₂. In (a) and (b), Cu(100). In (c) and (d), Cu(111). The inserts show the position of the line scans corresponding to the graphs. The baselines (dotted) used for the determination of the apparent heights at the positions marked with arrows are also shown.

The apparent height of the islands varies between the Cu(100) and Cu(111) substrates. The maximum and the average height of the islands is lower for islands formed on Cu(100) as compared to Cu(111), with a maximum height of 0.7

nm on (100) after 120 s and 1.6 nm on Cu(111). In addition, the variation in height is more pronounced for Cu(111), ranging from 0.4 nm to 1 nm as compared to 0.2 nm to 0.3 nm on Cu(100). The height of the flat islands on Cu(100) corresponds to the step height of Cu(100). Specifically for the 30 s measurement, we can see that the islands on Cu(111) have distinct step heights, possibly due to their arrangement according to the crystal structure of the oxide. We can identify two steps corresponding to the first and second island layer. One should keep in mind that these are apparent heights, since STM correlates to the local density of states which can deviate from the true height profile. Nonetheless, these results show a significant preference for a height increase of the islands in the case of Cu(111) over Cu(100).

In addition to the nanoscale morphology obtained by STM, we investigated the larger scale morphology of the samples in a LEEM/XPEEM system by analysing the low energy electrons reflected from the surface (LEEM), or, via X-ray photoemission electron microscopy (XPEEM), by recording the electrons emitted by the photoelectric effect. We observe in LEEM that the plasma oxidation does not change the morphology of the initial surface on scales larger than 100 nm. Both, LEEM and XPEEM-NEXAFS, show homogenous surfaces, with a roughness of about a few tens of nanometer that can be spatially resolved at low kinetic electron energies due to their highest sensitivity to lateral work function variations.⁸⁹

Figure 20 presents a comparison of LEEM images acquired on clean Cu surfaces of both orientations and those exposed to an in situ O₂ plasma (30 s, pO₂ = 4×10^{-4} mbar) treatment.

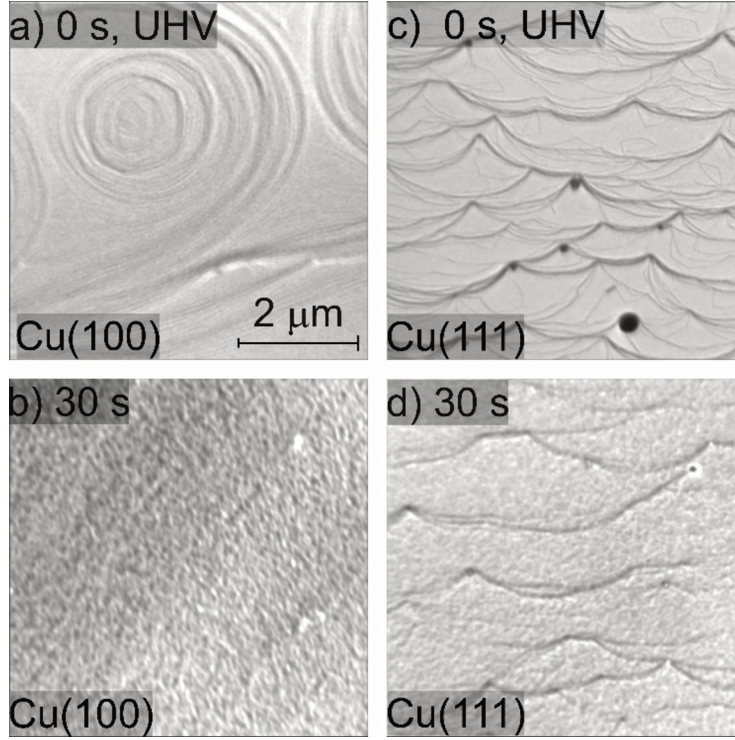


Figure 20: LEEM images recorded before and after 30 s of O₂ plasma treatment of the Cu(100) and Cu(111) surface, top and bottom row, respectively. (a) clean Cu(100), electron energy $E = 20$ eV; (b) Cu(100) after plasma treatment, $E = 2.3$ eV; (c) clean Cu(111), $E = 20$ eV; (d) Cu(111) after plasma treatment, $E = 2.4$ eV. The O₂ pressure during the plasma exposure was 4×10^{-4} mbar. Note that the images do not represent the same local area on the sample.

On the clean surface, the atomic steps and step bunches can be identified by dark lines. The 30 s plasma treatment in 4×10^{-4} mbar O₂ does not change the main texture significantly. However, a grainy morphology is clearly visible in figure 20 (b) and (d), corresponding to a spatial roughening of the surface and consequently, the sharpness of the step edges and of the step bunches gets gradually lost within 30 s and in the following treatments (not shown here). This plasma-induced roughening was observed on both orientations. Additionally, by following the LEEM intensity as a function of the electron energy, one can observe work function variations upon different stages. A discussion about this aspect is presented in the appendix.

3.3.2 Crystallinity

The crystallinity of the surface has been characterized by LEED in the LEEM/PEEM setup after each plasma treatment. Figure 21 presents the LEED images for the initial clean state, after 10 s, 180 s and after 1800 s of plasma treatment in 4×10^{-4} mbar O_2 , for both crystal orientations.

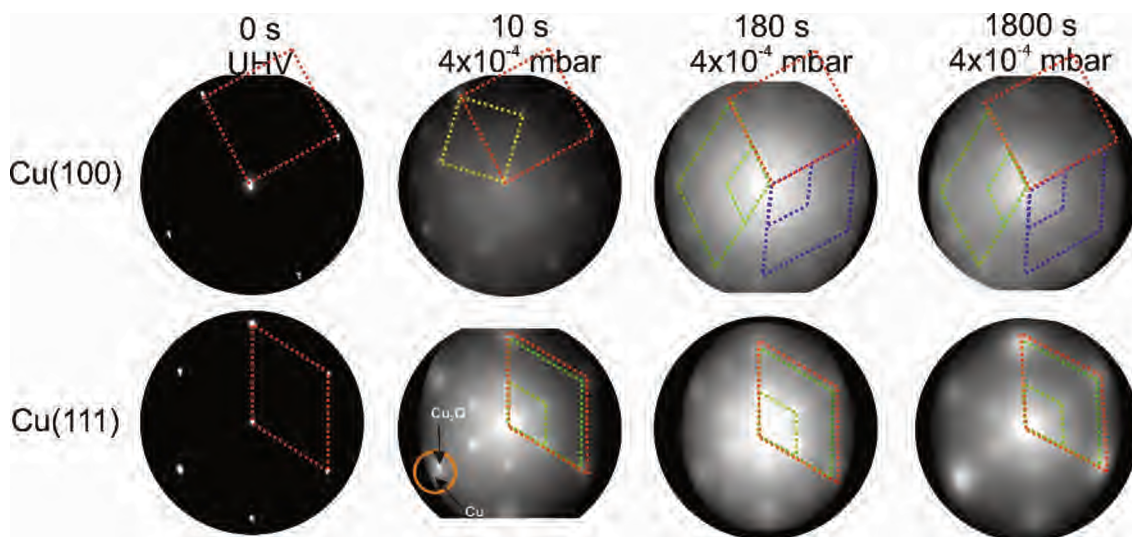


Figure 21: LEED images acquired on the Cu(100) and Cu(111) after different exposures to in situ O_2 plasma treatment, starting from the clean crystals (left), after 10 s, 180 s and finally after 1800 s of total oxidation time (right) performed in 4×10^{-4} mbar O_2 . The kinetic energy is 42 eV in all LEED patterns, except for the last column, where the energy is 32 eV. The dashed lines represent the unit cells of Cu crystals (in red), the $c(2 \times 2)$ reconstruction on Cu(100) (yellow square), unit cells of the two rotational domains on Cu(100) (green and purple, on top), respectively quasi (2×2) reconstruction and unit cell of $Cu_2O(111)$ (green, at the bottom).

The LEED pattern of the clean surfaces exhibit the spots of the metallic surface, with a four-fold symmetry for the (100) and six-fold symmetry for the (111) surface. The corresponding unit cells are presented in the pattern with red dotted lines. Within a plasma treatment of 1800 s one observes a clear change in the LEED pattern for both surfaces: (i) additional LEED spots appear – indicating larger unit cell size in real space and (ii) the spots get increasingly blurry – exhibiting a loss in crystallinity with increasing plasma exposure. However,

there are differences between the plasma oxidation of the two single crystal orientations. For both cases, the 10 s treatment constitutes a special case in the image series, since the oxide layer is so thin that the LEED pattern still displays the sharp (1×1) spots of the metallic support. The LEED of the Cu(100) substrate shows additionally a $c(2 \times 2)$ structure (marked with a yellow unit cell) and a ring of 12 diffuse spots which becomes more pronounced upon further treatment (marked in green and purple). The $c(2 \times 2)$ structure is well-known for oxygen adsorbed on Cu(100), a phase that was observed during the thermal oxidation of Cu(100) at lower oxygen content, e.g. 0.3 ML.^{68,90} The same 10 s treatment on the Cu(111) produced only a quasi (2×2) structure together with the substrate (1×1) spots, meaning a (111)-oriented growing oxide film, in agreement with the initial oxidation step observed in STM. A closer look exhibits a double spot structure (see the orange circle in figure 21), which proves that the oxide layer formed has a larger unit cell in real space than the substrate. In previous studies, a mismatch of 17.5% has been estimated between the two unit cells, taking into consideration that the $\text{Cu}_2\text{O}(111)$ surface unit cell is 2.35 times larger than the one of Cu(111).⁹¹

For oxidation treatments longer than 10 s in 4×10^{-4} mbar O_2 , the LEED patterns do not show substrate spots anymore, but the quasi (2×2) superstructure with the hexagonal orientation corresponding to the ongoing growth of $\text{Cu}_2\text{O}(111)$ and $\text{CuO}(111)$ film. However, on the Cu(100) crystal, the LEED pattern is composed of 12 equally distant diffuse spots superposed to an inner smaller diffuse ring. The structure can be described by two coexisting rotational domains of hexagonal structures (see the green and purple unit cells in figure 21). The same structure has been previously reported for an oxygen covered Cu(100) surface which was annealed at 870 K for a longer time⁹², that was explained by two domains of an hexagonal phase, rotated by 90° against each other and each aligned along one crystallographic surface direction. This structure was attributed to the (111) phase of Cu_2O , at an oxygen content of maximum 2.6 ML. In our case, the remarkable difference is that the same kind of structure could be obtained even at room temperature as a result of the interaction of the O_2 plasma with the surface. In contrast, the LEED pattern of the Cu(111) crystal

shows the formation of a single (2×2) domain that does not change significantly during the plasma treatment. Comparing the LEED pattern changing over time for the two crystals, one observes a spot broadening with ongoing treatment, but at the same stage of treatment the spots on the Cu(100) crystal are broader and more diffuse than on the (111). The broadening of the LEED spots in the present data set, in comparison with the previous reports,⁹² indicates a higher density of defects and smaller grain size⁹³ than it would be expected for films grown by thermal oxidation. Based on the spot width one can estimate a grain size of about 2.5 nm for the CuO film produced by plasma-assisted oxidation.

From the crystallinity point of view, it is worth to compare the plasma oxidation with the thermal analogue. The latter has been well studied so far in a large range of exposure times, oxygen pressures and temperatures.⁶⁷ In the case of the thermal oxidation of Cu(100) crystals, during the initial oxygen adsorption at low oxygen coverages of about 0.3 ML and temperatures lower than 473 K, the $c(2 \times 2)$ reconstruction is observed, while at higher coverages the missing row (MR) structure $(2\sqrt{2} \times 2)R45^\circ$ starts to form.^{94,95} In our case, the $c(2 \times 2)$ structure could be identified only in the case of 10 s at 4×10^{-4} mbar O_2 treatment, but no MR pattern could be detected in the LEED data. Further oxygen dosing or higher temperature induce the initial growth of Cu_2O islands that develop and coalesce. In fact, the wetting layer displays again a MR structure.⁶⁹ Nevertheless, excepting the already discussed report⁹² of the two rotational domains that we observe after oxygen plasma oxidation, we could not find any other study that reports the growth of hexagonal $Cu_2O(111)$ on top of cubic Cu(100).

In the case of the Cu(111) surface, it is known that it does not favour the adsorption of oxygen at lower coverages. Various structures and reconstructions have been reported for oxygen adsorption on Cu(111) at RT or at higher temperatures and for the initial oxidation^{74,88,96}, displaying rather complex LEED patterns. Regarding the $Cu_2O(111)$ reconstructions typically observed, one could identify the (1×1) and $(\sqrt{3} \times \sqrt{3})R30^\circ$, which were attributed to a pristine oxygen-terminated (111) surface, respectively to a defective $Cu_2O(111)$ surface missing oxygen anions.^{86,87,97} Additionally, during the thermal oxidation, the

'44' or '29' reconstructions are typically observed upon annealing at over 423 K or over 673 K and describe surface oxide structures with unit cells that are 44 or 29 times larger than the one of Cu(111).^{75,88,98} Other rather complex reconstructions have also been observed after exposing the Cu(111) surface to a hyperthermal oxygen molecular beam at RT.⁹⁹ Interestingly, we could not identify an experimental study to report a (2×2) reconstruction of oxygen adsorbed on Cu(111) or of Cu₂O(111), even though there are theoretical studies that considered these kind of structures.⁷² Other studies reported a mixture of (2×2) and weak $(2\sqrt{3} \times 2\sqrt{3})$ superstructure in the case of Cu oxidation on top of Pt(111) at high temperatures¹⁰⁰, which resulted in a similar LEED pattern as the ones shown herein. Taking into consideration the spectroscopic results that will be discussed in the following section, one can assume that longer exposures to oxygen plasma produce a thick CuO layer on the surface, while the Cu₂O is only an intermediate layer of about 1 nm to 2 nm thickness. One could infer therefore that the LEED data acquired for the samples exposed to the plasma for longer times correspond to a CuO(111) surface. In fact, the increase of the diffuse shape of the LEED spots by time could be interpreted as being the consequence of an increase of the lattice tension induced by the growth of the top layer. Interestingly, there are no particular reconstructions that could be observed at intermediary oxidation steps that could have indicated the formation of a different oxide. Furthermore, the attempt to anneal the crystals after the final oxidation treatment up to a maximum of 570 K (not shown) did not result in a stabilization of a flat oxide film, but in dewetting and the formation of multiple oxide islands, where the LEED patterns of the surface did not resemble the one acquired after 1800 s of plasma oxidation in 4×10^{-4} mbar O₂.

3.3.3 Chemical Composition

The chemical state of the samples was probed after each step of the plasma treatment by measuring the Cu LMM Auger peak with XPS in the STM/XPS system and additionally, over longer exposure times by Cu-L edge and O-K edge NEXAFS in the LEEM/XPEEM system. The Cu LMM spectra and the results of the related analysis of the component fitting (appendix, figure 42) are shown in figure 22.

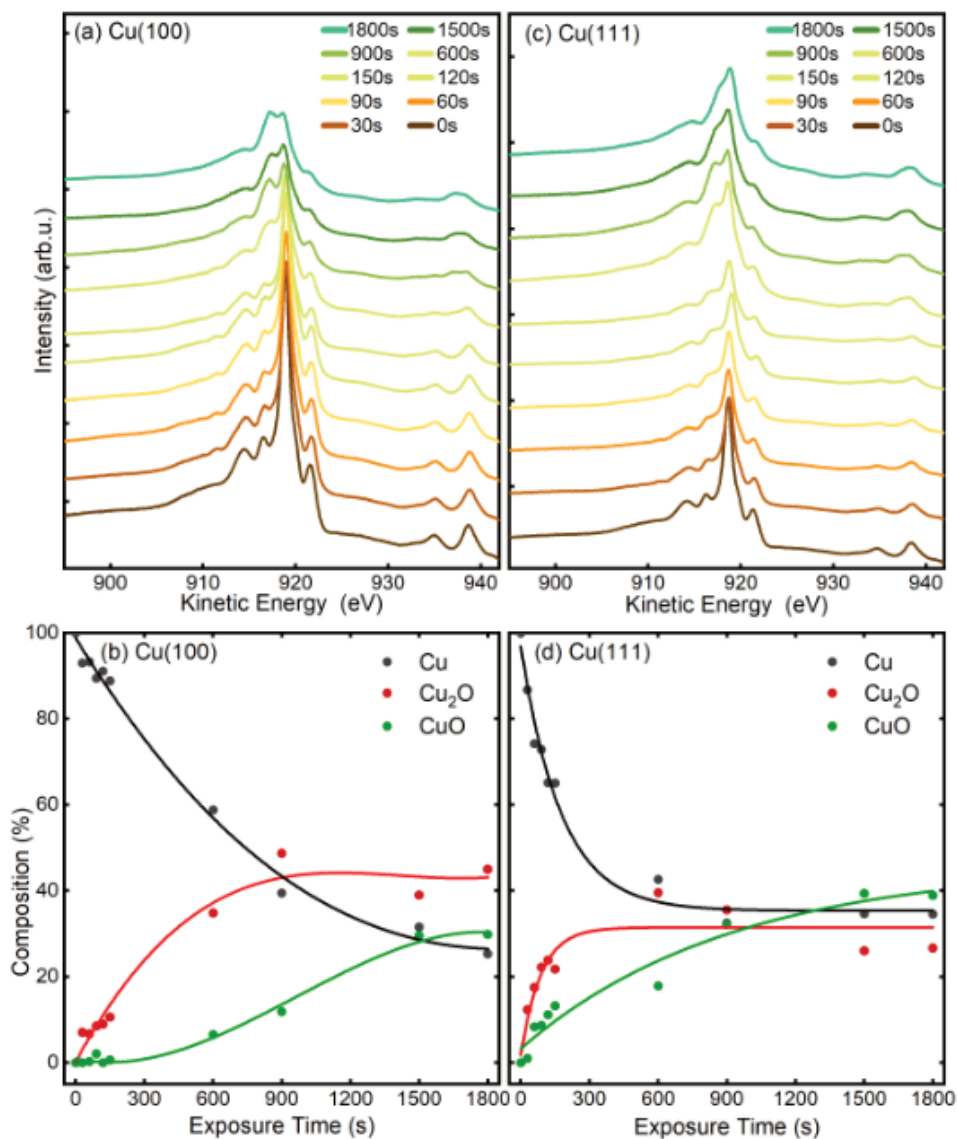


Figure 22: Cu LMM AES spectra measured before and after different in situ O₂-plasma exposures at 3×10^{-5} mbar of (a),(b) Cu(100) and (c),(d) Cu(111) single crystal surfaces. The content of the different Cu species was determined by fitting and deconvolution of the Cu LMM signal (b and d). The corresponding fits are shown in the appendix in figure 42. The connecting lines are meant as guides for the eyes.

The analysis of the Cu LMM peaks after each plasma treatment step reveals a different evolution of the content of the Cu₂O and CuO species for the Cu(100) and Cu(111) surfaces, as shown in Fig. 22 (b) and (d), respectively. Cu₂O and CuO are formed immediately upon plasma exposure on Cu(111), in contrast to the Cu(100) surface, where only Cu₂O is formed up to at least 150 s at 3×10^{-5} mbar O₂. The ratio of metallic to oxidized copper species decreases also faster on Cu(111) for exposures under 900 s, after which both surfaces exhibit slower oxide growth. The former behaviour is in accordance with the STM morphology results, where the comparative island growth over time inferred a swifter oxidation of Cu(111). After a total exposure of 1800 s, a significant difference in the Cu species is apparent. On Cu(111), the nominal Cu₂O content has decreased to 27 % and CuO increased to 39 %. On Cu(100), the fractions are reversed, with 45 % Cu₂O and 34 % CuO. Indeed, we initially see that the Cu₂O and CuO content on Cu(111) increases similarly, before the Cu₂O contribution levels off after 150 s, while CuO still increases. This trend was different on Cu(100), where the Cu₂O increases faster than CuO until an inflection point is reached after 900 s. The remaining detectable metallic copper after 1800 s *in situ* O₂-plasma exposure for both crystals is similar at 25 % for Cu(100) and 34 % on Cu(111), which is a sign of a thin film in the range of a few nanometers, which is compatible with the STM results. It should be noted that the XPS signal of the deeper layers (Cu, Cu₂O) is also expected to be dampened with increasing thickness of the CuO overlayer.

To extract additional information on the formation and stability of the different oxide species formed upon O₂-plasma exposure, NEXAFS spectra have been measured in microscopy mode, by recording the signal around the maximum of the secondary electrons peak, using an energy filter. No local contrast could be resolved, which proves the homogenous oxidation of the surface, and therefore, the NEXAFS spectra that are discussed herein represent the total intensity of the emitted electrons recorded in a field of view of 20 μm. In figure 23, the NEXAFS spectra measured after each O₂ plasma treatment are shown, as well as the intensity of various components, Cu, Cu₂O and CuO, as determined by a linear combination (LC) analysis based on NEXAFS fingerprints of the different Cu

species.^{101,102} The details regarding the LC analysis can be found in the appendix. The variation of the intensity profiles is in a good agreement with the XPS/AES measurements described previously, considering a different signal damping for the two instrumental set-ups. In the case of Cu(100), the initial oxidation steps also show only an increase of the Cu₂O component, while the first signal of CuO could be detected only after a total exposure of 60 s O₂-plasma in 4×10^{-4} mbar. On the other hand, the spectra of the Cu(111) surface show the formation of both, Cu₂O and CuO species right after the 10 s treatment. In both cases, after about 60 s atomic oxygen exposure, the Cu₂O signal gradually decreases, while CuO continues to increase which can be explained with the signal damping of the Cu₂O underlayer caused by the CuO film overgrowth, discussed in the following.

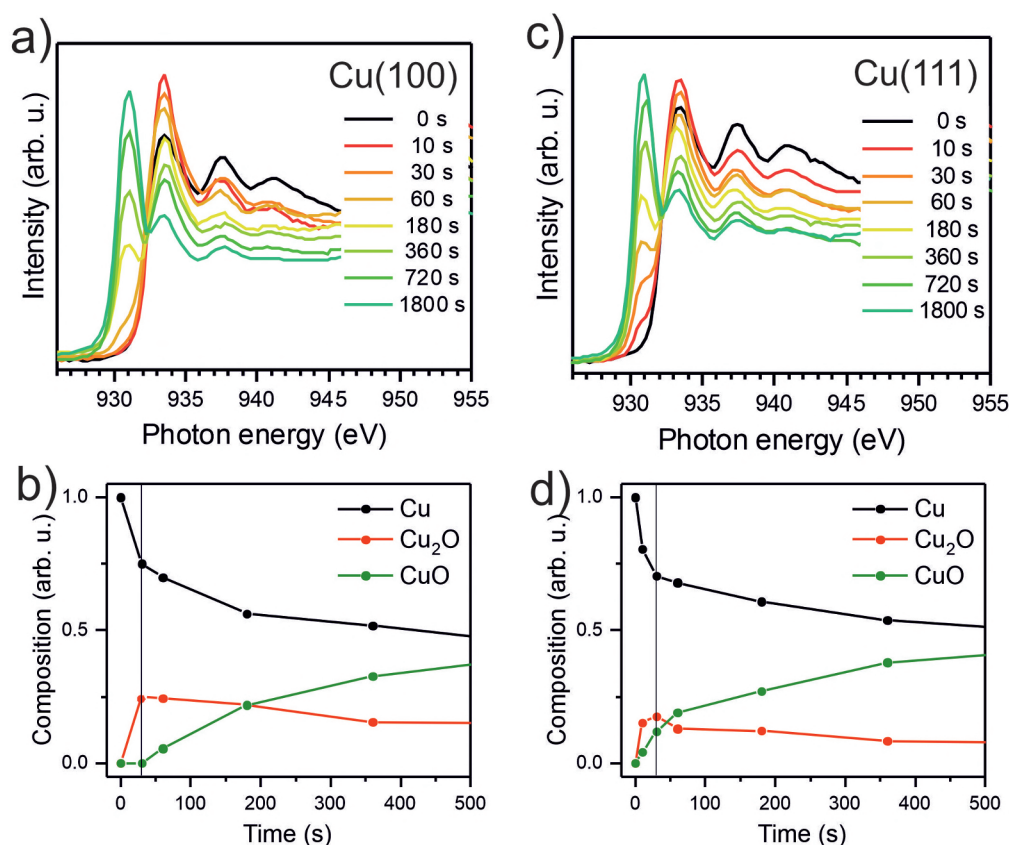


Figure 23: NEXAFS after *in situ* oxygen plasma treatment of Cu(100) and Cu(111) at 4×10^{-4} mbar O₂, top and bottom row respectively. (a, c) Cu L-edge NEXAFS data at different doses. (b, d) The analysis displays the content of metallic Cu, Cu₂O and CuO versus oxygen plasma treatment time. The O₂ pressure during the plasma exposure was 4×10^{-4} mbar.

Based on the intensity evolution extracted from the NEXAFS spectra, we constructed a model to explain the oxide growth during the plasma exposure of the two crystal orientations. A simple model can be imagined in the case of the Cu(100) orientation, based on the two stages of gradual oxidation, i.e., $\text{Cu} \rightarrow \text{Cu}_2\text{O} \rightarrow \text{CuO}$, where we assume for the first stage a linear increase of the concentration of Cu_2O species, followed by the CuO growth on top. The details about this model are described in the appendix. Starting from the assumption of this sandwich-like film structure where the thickness of Cu_2O species increase linearly within 30 s and stays constant at $\delta = 2.2$ nm in the following and considering the attenuation of the intensity with the thickness of the oxide layer, we try to correlate the intensity evolution with the oxide layer thickness and with the exposure time to oxygen plasma. Figure 24 (a) presents a fit of the Cu composition displayed in Figure 24 (b) as a function of the total time, by assuming that the plasma oxidation rate is exponentially damped by the thickness of the growing oxide film, yielding $\Delta(t) = \Lambda \ln(1 + \frac{R}{\Lambda}t)$, where Λ is the effective oxidation length and R is the initial oxidation rate (i.e. thickness per time, see also appendix). The fitting curves prove that the damping model employed largely describes the experimental curves. We also tried a model considering a linear growth of the oxide which however did not match the experimental data, which is shown in the appendix for reference. The parameters extracted from the fits are displayed in the appendix.

By considering the inelastic mean free path to be around 5 nm at the implied electron kinetic energy, the damping model provides an initial oxidation rate of the CuO layer of $R = 0.015 \text{ nm s}^{-1}$ and an effective oxidation length of $\Lambda = 1.75$ nm. Based on these values we constructed the schematic representations shown in Fig. 24, where the two-step growth taking place in Cu(100) is illustrated for the two copper species as a function of the exposure time and total thickness. For the growth profile in figure 24 (c) and (f) we considered the different atomic Cu densities in the metallic support and the two oxide structures. This results in the oxide film growth into the Cu bulk as well as out of the surface, whereas the initial surface position is defined at $z=0$ nm (dashed lines in figure 24(c) and (f)).

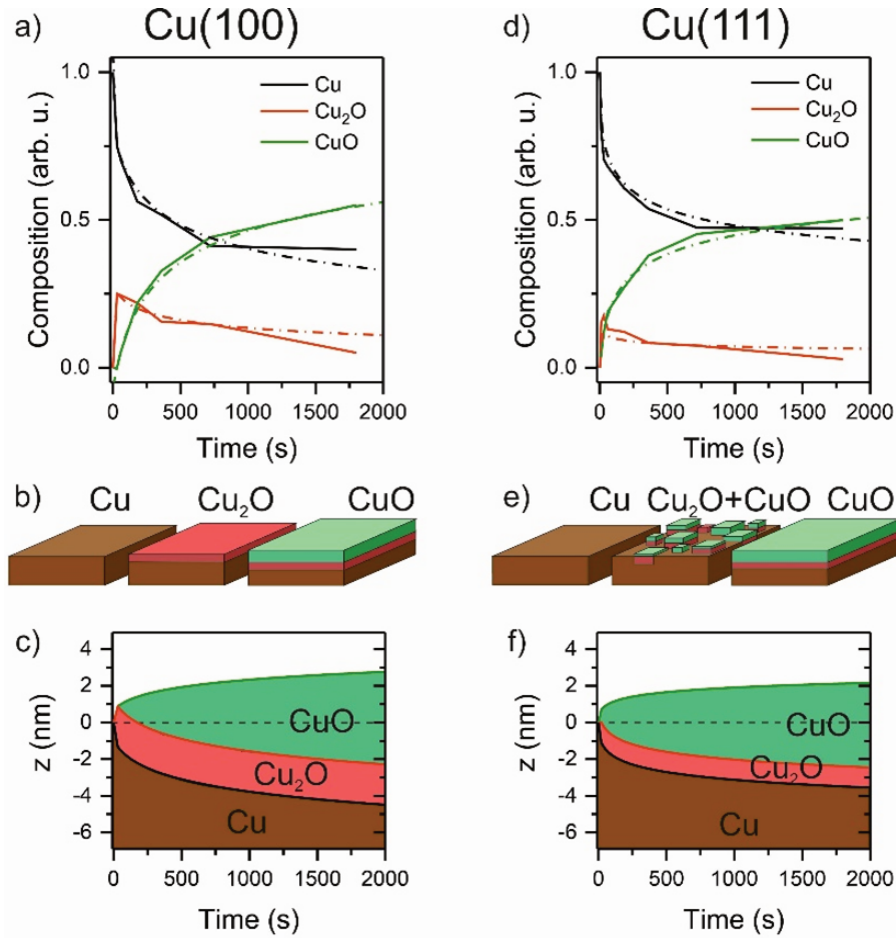


Figure 24: Oxide film growth on Cu(100) (a-c) and on Cu(111) (d-f) by oxygen plasma treatment at 4×10^{-4} mbar. (a) and (d) raw data and fitting of the NEXAFS composition using a damping model. (b and e) Schematic of the oxidation model showing the initial metallic copper surface, the intermediate state with a complete Cu₂O film on the Cu(100) crystal and a mixture of Cu₂O and CuO for the Cu(111) surface. As a final state, the CuO film overgrows the Cu₂O film. (c, f) exhibit the sample depth profile over the plasma exposure time using a damping model. After 30 s the Cu₂O film keeps a constant thickness and is overgrown by the CuO film whereas the growth rate is damped over dosage.

For the oxidation of the Cu(111) crystal, we modified the model. The two oxide species grow again in a sandwiched structure with CuO on top of Cu₂O, but, contrary to Cu(100), (i) the CuO starts to grow from the very beginning on Cu(111) and (ii) the Cu₂O grows linearly in thickness up to 20 s and keeps

a thickness of constant $\delta = 1.1$ nm in the following. Despite the uncertainty of the initial growth stages, the damping model describes the experimental data quite well and is similar to the growth on the Cu(100). However, the growth parameters on Cu(111) are slightly different: the Cu₂O film thickness is half the one of Cu(100), the oxidation rate $R = 0.05 \text{ nm s}^{-1}$ and the effective oxidation length of $\Lambda = 1.0$ nm differ by a factor of about 3 and 0.6, respectively. Notably, with these two sets of oxidation parameters, the XPS data in figure 22 are also well described, if mainly the mean free path length of the electrons is adapted to 2 nm (see appendix). Concluding from the chemical analysis, it is demonstrated that the oxide formation (at the investigated exposures) is limited to a confined space near the surface. The ratio between the different oxides depends on the exposure, with different evolution trends for the two surface orientations.

In our oxidation study, we find similarities and deviations to reported thermal oxidation dynamics on the two surface orientations. On Cu(100), Lahtonen et al. have described a structure of disordered Cu₂O islands on a reconstructed surface, which they achieved by dosing a total of $9.4 \times 10^{-2} \text{ L O}_2$ at $3.7 \times 10^{-2} \text{ mbar}$ and 373 K.^{68,69} The resulting structure appeared similar in STM to our observations here for plasma treatments at a dosage below 120 s, corresponding to 2700 L². However, the conditions differ greatly, as we found this to happen at a significantly lower O₂ pressure (10^{-5} mbar). Critically, we also found further oxidation towards a closed CuO film for continued sequences which has not been reported to occur without the use of elevated temperatures.

² Unit of dosage is Langmuir, equivalent to $1 \text{ torr } \mu\text{s}^{-1}$

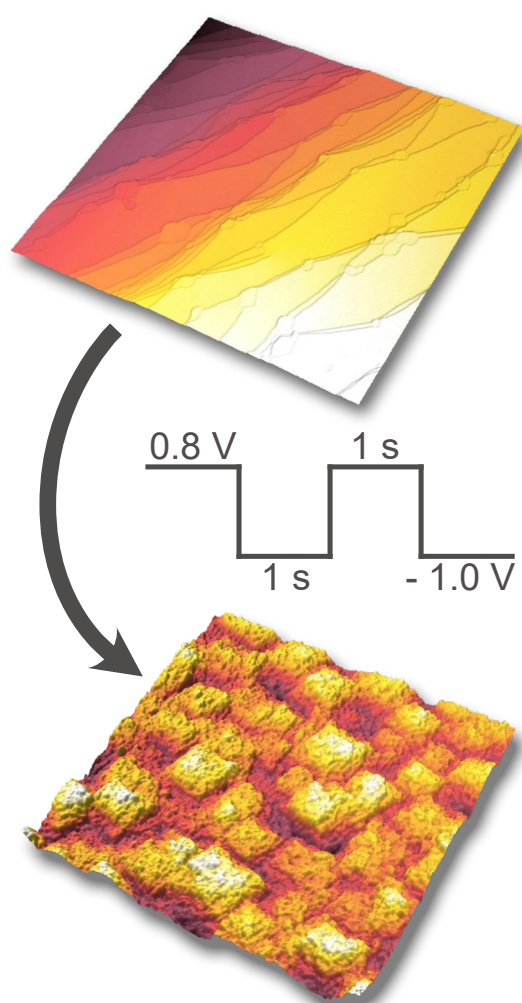
3.4 Summary

Here, we systematically investigated the oxidation of low index copper surfaces at RT under the influence of an oxygen plasma at low pressures of 10^{-5} mbar to 10^{-4} mbar O_2 , employing a multi-technique approach in two different setups that allowed comprehensive sample characterization while controlling for reproducibility. Our study of non-thermal plasma assisted oxidation constitutes one of the first studies to provide insight on the resulting surface structure and composition by such plasma treatments. We revealed not only different growth behaviors of the two investigated Cu crystal orientations, but at the same time we show that longer plasma-assisted oxidation stabilizes on both substrate orientations an ordered $CuO(111)$ film. We identified different behaviors regarding the evolution of the morphology and oxide composition on $Cu(100)$ and on $Cu(111)$ surfaces, respectively. The initial growth of an approximately 2 nm thick homogenous Cu_2O film on the (100) substrate is similar to thermal oxidation. However, on the (111) substrate, both Cu_2O and CuO species form simultaneously during the first plasma exposure. This behavior can be correlated not only to distinct morphological transformations, but also with a different growth rate that seems to be determined by the substrate orientation. A higher growth rate could be determined for the (111) crystal. This behavior is in a very good agreement with the STM measurements, where the closing of the oxide film proved to happen at an earlier moment on (111) as opposed to (100). On both surface orientations however, longer exposures up to 30 min lead to the development of a few nanometers thick CuO layer that shows a preferential orientation along the (111) direction, as was observed by LEED. In both cases, the CuO outer layer is interfaced with the metallic substrate by a Cu_2O buffer, which is thinner in the case of (111) substrate. In fact, the hexagonal (111) structure develops from the initial oxidation stages, proving that not only CuO , but also Cu_2O prefers to grow in this particular (111) direction. Interestingly, even though the orientation of the growing oxide film is the same, the surface reconstructs distinctly in the way that the (100) substrate accommodates two different small rotational domains, rotated by 90° against each other, what has been not yet reported at RT, while the (111) develops a quasi (2×2) reconstruction. These observations lead to

two main implications. First, they demonstrate the ability of oxygen plasma treatments to grow predictable oxide structures at very mild conditions. This is a very useful characteristic and lends this approach to an application as a novel tool for precision synthesis. Second, our findings also emphasize the necessity to consider surface terminations when dealing with reactive environments. Even with the high reactivity of ionized oxygen, the lattice orientation of the substrate has still a major influence on the entire reaction sequence regarding nucleation, growth mode, grain size and compounds formed. Finally, our work represents an initial step towards the further exploration and utilization of plasmas for the controlled synthesis of oxide phases and tunable restructuring of surfaces.

Chapter 4

In Situ Generated Morphological Motifs on Cu(100) by Pulsed Electroreduction



4 *In situ* generated morphological motifs on Cu(100) by pulsed electroreduction

This chapter is based on content that has been previously published in Arán-Ais, R.M., Scholten, F., Kunze, S., Rizo, R., Roldán Cuenya, B. . *The role of in situ generated morphological motifs and Cu(I) species in C₂₊ product selectivity during CO₂ pulsed electroreduction*. *Nat Energy* 5, 317–325 (2020)⁶⁴. Here, the data is analyzed in more detail and with additional focus on the surface structure. I was solely responsible for the planning and execution of the sample preparation, AFM experiments and subsequent data analysis.

4.1 Introduction

As mentioned in chapter 1.3, it has been shown that the (100) orientated surface of copper single crystals is favorable for the C-C coupling pathway for the production of ethylene in the CO₂RR.^{33,34} We have presented in the previous chapter a study that demonstrated the use of O₂-plasma treatments to obtain Cu(111) and Cu(100) surfaces with tunable Cu/Cu₂O/CuO ratios in a confined volume of the surface. In a previous study on copper foils oxidized by an *ex situ* plasma, it was shown that the selectivity for ethylene can be increased and the onset potential decreased.⁶² In addition, the favorable effect of oxidized surface species towards alcohol selectivity has also been recently noticed.⁶⁶ It has been hypothesized that this is due to a combination of Cu(o) and Cu(I) species on the

surface that favor CO dimerization. The role of Cu(I) species is however a subject of controversy, precisely because the stability of them under reaction conditions is difficult to deduce.^{103–105}

The following study was part of an effort to specifically understand the influence of Cu(I)-species on the catalytic performance of copper catalysts. We used rationally designed pulsed potential sequences to tune the oxide composition and surface structure of the Cu(100) surface. Through carefully designed quasi in-situ XPS and AFM characterization, we could identify the Cu(0) and Cu(I) ratios for a given potential sequence, while simultaneously controlling the surface structure. This allowed us to study their role in the product selectivity and determine a synergistic effect of continuous defect and Cu(I)-species regeneration for C-C coupling pathways.

Here, we will focus on the the morphological aspect related to this study. To adequately assign the effects of the Cu(I) species, a detailed understanding of the surface structure for each potential sequence was needed as well, to avoid wrongfully assigning their influences to that from structural effects. We focused on establishing a methodology based on reproducible, well-defined and clean surfaces that we obtained via surface preparation in UHV. To further exclude unwanted influences due to the exposure to a chemically altering atmosphere, we conducted the electrochemical experiments without exposing the samples to the atmosphere. In parallel we investigated the transformations undergone by a 'perfect' surface when it is exposed to air and electropolishing, which is commonly used to prepare single crystal surfaces for electrochemical studies, to understand whether our UHV prepared surface is stable enough for repeated experiments.

4.2 Experimental Details

Clean, flat Cu(100) single crystal surfaces (MTI Corporation) were prepared in UHV by repeated cycles of Ar⁺-sputtering at 3×10^{-5} mbar with a kinetic energy of 2.5 keV for 15 min to 30 min, followed by annealing to 880 K for 10 min to 15 min. After an electrochemical experiment, the crystal was first briefly electropolished in 85 % H₃PO₄ for 20 s for a coarse cleaning, then rinsed with ultrapure water (18.2 MΩ) and dried in a stream of nitrogen (5N, Air Liquide), before it was introduced to UHV. After preparation in UHV, the sample was then transferred from UHV to the attached chamber under argon atmosphere, and inserted into the electrochemical cell. The setup is described in more detail in chapter 2.

The electrochemical experiments were carried out using an Autolab PGSTAT 302N potentiostat from Metrohm. Measurements were done in a three-electrode configuration, with a Pt-gauze (MaTeck, 3600 mesh cm⁻²) as counterelectrode, leak-free Ag/AgCl reference electrode and the copper sample as the working electrode. The electrolyte was CO₂-saturated (N4.5, Air Liquide) 0.1 M KHCO₃ (99.9 %, Sigma Aldrich), which was previously cleaned from trace metal impurities via a cation-exchange resin (Chelex 100 from Bio-Rad). CO₂ was continuously bubbled through the electrolyte during experiments at a rate of 20 ml min⁻¹, controlled with a mass flow controller (Bronkhorst).

After a measurement in the electrochemical cell, the sample was pulled back into the argon-filled inert gas chamber, and rinsed copiously with argon-saturated ultrapure water (18.2 MΩ) before being dried in an argon stream and then taken out for AFM and SEM measurements. AFM was done in TappingMode on the Bruker Multimode 8 AFM described in chapter 2.

We subjected the samples to pulse sequences (square wave) in 0.1 M KHCO₃ for 1h, where each sequence starts with a 1 s pulse at an anodic potential (E_a) followed by a cathodic pulse of $E_c = -1$ V vs RHE, a potential typical for CO₂RR. The length of the cathodic pulse was varied, as well as the potential of the anodic

pulse. Table 2 summarizes the surface treatments and reaction conditions that were investigated in this study.

Table 2: Tabulated summary of surface treatments and reaction conditions applied to Cu(100).

Surface preparation	Reaction	E_a (vs. RHE)	t_a	E_c (vs. RHE)	t_c
UHV					
UHV/Air					
UHV/air/electropolish					
UHV	1h @ -1.0 V				
UHV	1h pulses	0 V	1 s	-1 V	1 s
UHV	1h pulses	0.4 V	1 s	-1 V	1 s
UHV	1h pulses	0.6V	1 s	-1 V	1 s
UHV	1h pulses	0.8 V	1 s	-1 V	1 s
UHV	1h pulses	0.6 V	1 s	-1 V	0.2 s
UHV	1h pulses	0.6 V	1 s	-1 V	0.5 s
UHV	1h pulses	0.6 V	1 s	-1 V	29 s
UHV	1h pulses + 1h @ -1.0 V	0.6 V	1s	-1V	1s

4.3 Results and Discussion

4.3.1 Influence of atmosphere and electropolishing

Figure 25 (a) shows an overview STM image of the Cu(100) surface following the UHV cleaning procedure described above. A stepped surface with atomically flat terraces was obtained. Figure 25 (b) shows an atomic resolution image obtained on a terrace, which expectedly revealed the (100) plane geometry as depicted in the ball model in (c). Following the outlined experimental cleaning procedure, the crystal morphology could be reliably restored after electrochemical experiments, even on an atomic level. By this, we can ascertain that prior experiments do not influence the results of a subsequent measurement, if the surface is restored according to this workflow.

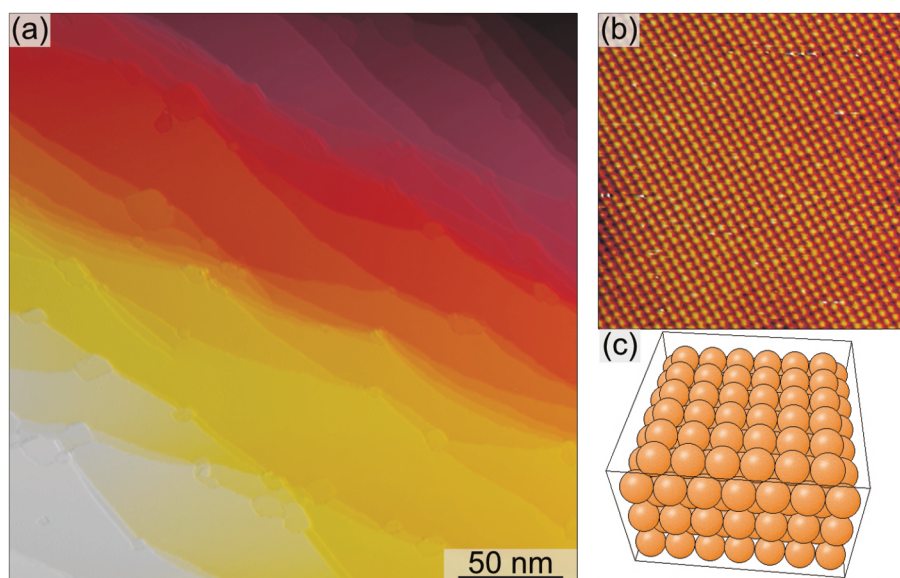


Figure 25: (a) Constant current STM image of the UHV cleaned Cu(100) surface. $U_{bias} = 0.83$ V, $I_t = 0.66$ nA (b) Constant current STM image with atomic resolution from the same measurement as (a). $U_{bias} = 0.41$ V, $I_t = 0.23$ nA. Image size is 8.35 nm \times 8.35 nm. (c) Ball model of a Cu single crystal with a (100) surface termination on top.

After taking the UHV-prepared crystal into atmosphere, no macroscopic or mesoscopic changes to the surface morphology were observed in AFM measurements. The AFM images shown in figure 26 prove that the stepped surface structure is largely retained upon air exposure. On the nanoscale, we see however a surface roughening (figure 26 (b)). We could not determine the atomic structure of these with the limited resolution of TappingMode AFM, and we cannot exclude that this is a result of approaching the resolution limit of our AFM tips, which are themselves several nm wide at their apex with an unknown roughness that is also subject to changes due to the intermittent contact with the sample surface during measurement. Therefore, we want to note that the geometry of the steps and terraces is reliably imaged, but the structures on the terraces themselves should be considered carefully in hindsight of the equipment limitations. In a more recent study, we showed the stepped surface with equivalent sample preparation using an AFM with a higher resolution, and found a reduced roughness on the nanoscale.¹⁰⁶ For the following results however, it should be kept in mind that the shown roughness here should apply to all subsequent images.

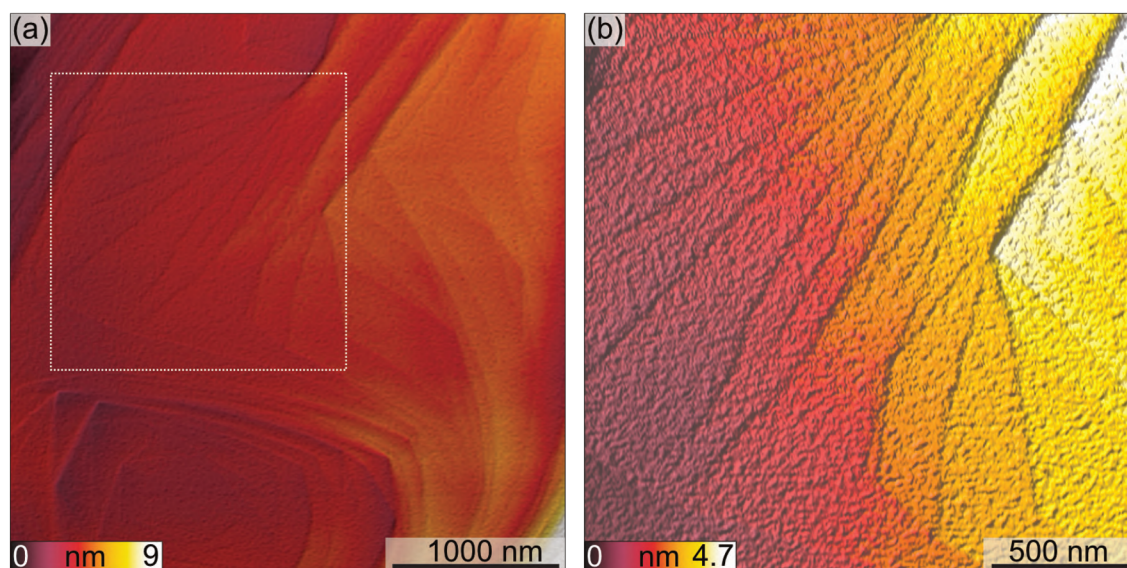


Figure 26: AFM images of the UHV cleaned Cu(100) surface in air. The white box in (a) marks the location of the scan area of (b).

Electrochemical experiments are often done on sample surfaces that were cleaned by short, anodic electropolishing procedures. In the related study, we used electropolished single crystals to run electrochemical experiments for the determination of the product distribution in the CO₂RR.⁶⁴ In order to determine the effects of our electropolishing procedure, we imaged a freshly UHV-prepared Cu(100) crystal after 20 s electropolishing following the procedure outlined in the experimental part. Figure 27 (a) shows the corresponding AFM images. We find that the surface is overall flat, but round depressions of 1 nm to 2 nm height and diameters under 0.3 μm are visible, shown in linescans in figure 27 (c). The surface is also covered with nanoparticles of several nm height, which appear to decorate edges along the depressions. They also arranged along step edges, which are however difficult to identify here due to the limited contrast (along the white arrows). It is reasonable to assume that these particulates are residue crystallites from the electropolishing treatment formed by the salts of the acid (H₃PO₄), which could be resolved by rinsing the sample for a longer time after the polishing procedure. In general however, we find that the short electropolishing of the UHV prepared crystal does not destroy the stepped surface, though it does create a few nm-large defects.

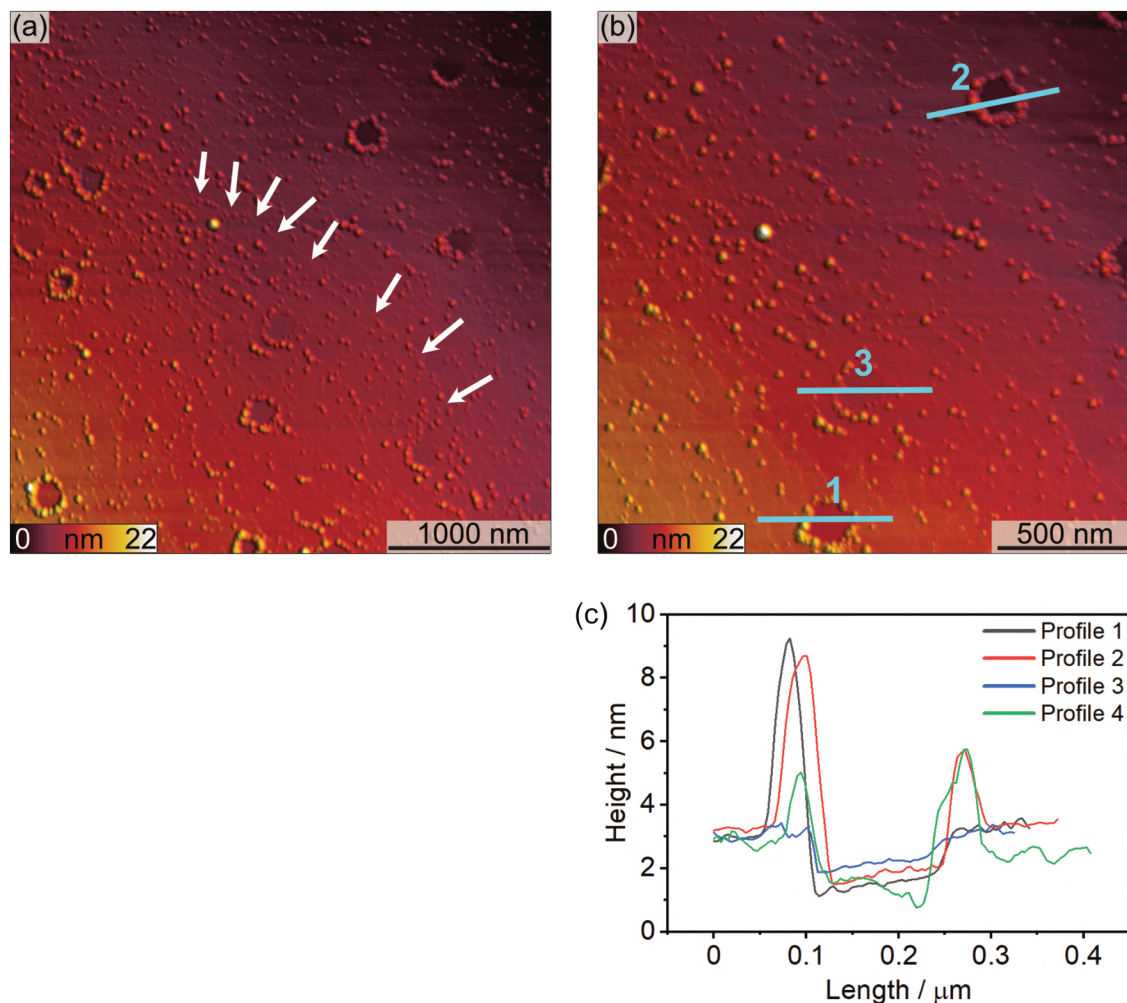


Figure 27: AFM images (a, b) of the UHV-cleaned Cu(100) surface after 20 s electropolishing. The white arrows in (a) indicate the position of a step edge. (c) Height profiles along the numbered lines in (b).

4.3.2 Surface morphology after electrolysis at a fixed potential

The typical potential at which the CO_2RR is observed on Cu(100) is -1 V vs RHE. We therefore chose this value as the cathodic potential for the pulsed potential sequences. To distinguish the origin of the changes in composition and morphology, i.e., whether they are a result of the anodic or cathodic pulse, we investigated the Cu(100) surface after 1 h at a fixed potential of -1 V vs RHE. The AFM images presented in figure 28 show the Cu(100) surface after this treatment. They reveal a surface with a more 'granular' nanostructure compared to the pristine surface. This surface roughness is still comparatively small with an amplitude of ≈ 4 nm and no large corrugations were found. Some larger particles,

likely residue crystallites from the electrolyte that were not removed by washing, are also found on the surface. These are up to 32 nm tall, but we do not assign them as a consequence of the electrolysis.

Unfortunately, it is inconclusive from these images if a stepped structure is retained. The surface appears to be flat and without steps, but they might be obscured due to an effect of the increased roughness, which negatively impacts the plane levelling algorithm during the image processing. In a recent follow-up study, the structure of surfaces prepared in this fashion was unravelled with higher definition.¹⁰⁶

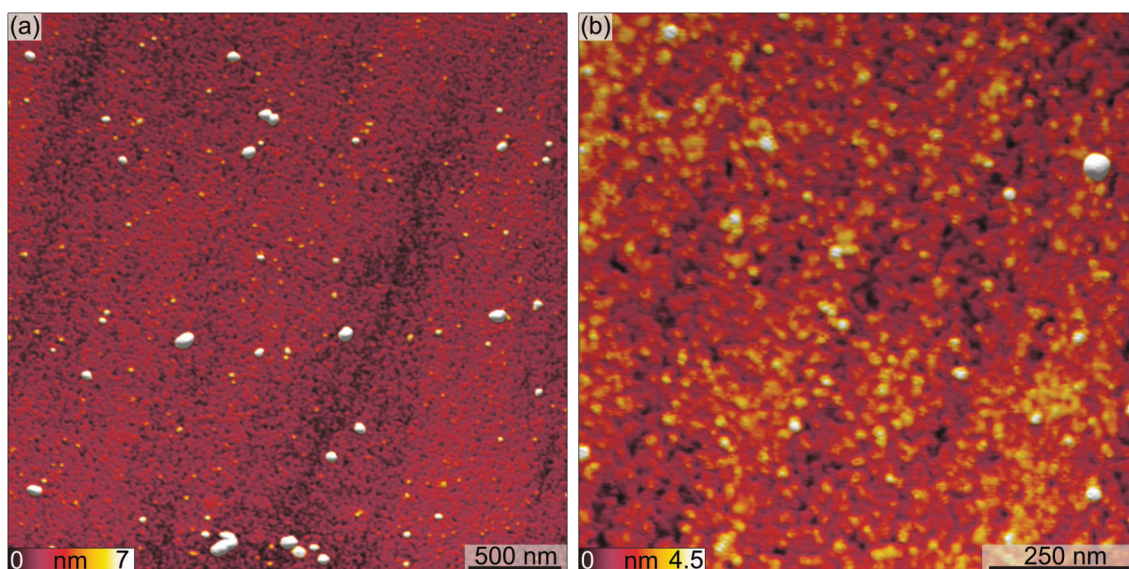


Figure 28: AFM image of a UHV prepared Cu(100) surface after 1 h of electrolysis at a fixed potential of -1 V vs. RHE in 0.1 M KHCO_3 . The crystal was transferred from UHV to the electrochemical cell without exposure to air. The height scale is cut off at 7 nm and 4.5 nm to enhance the contrast towards the nanoroughness of the substrate.

4.3.3 *Potential dependent modifications*

Varying the anodic potential for isochronous pulses was our approach to monitor how different potential regimes alter the surface structure. We conducted experiments with pulsed potential sequences at four anodic potentials: 0 V, 0.4 V, 0.6 V and 0.8 V (vs. RHE). We found that the two higher potentials 0.6 V and 0.8 V result in similar morphologies, as shown in figure 29. Such sequences result in cubic structures of about 30 nm height that densely cover the surface. Since these are fairly oxidative potentials, dissolution of copper into solution during the anodic pulse is likely, with a following cathodic pulse redepositing dissolved copper, which epitaxially forms the cubic structures that densely populate the surface and give rise to a structural motif, which we visualized in a 3D representation in figure 29 (b) and (d). This is similar to previously encountered cube growth on carbon materials from a cuprous solutions.^{107,108} The size of these cubes is not increased on the sample which was exposed to higher anodic potential of 0.8 V. This is in strong agreement with our proposed mechanism, since after a certain potential value, we do not expect significantly higher rates of dissolution during the anodic pulse.

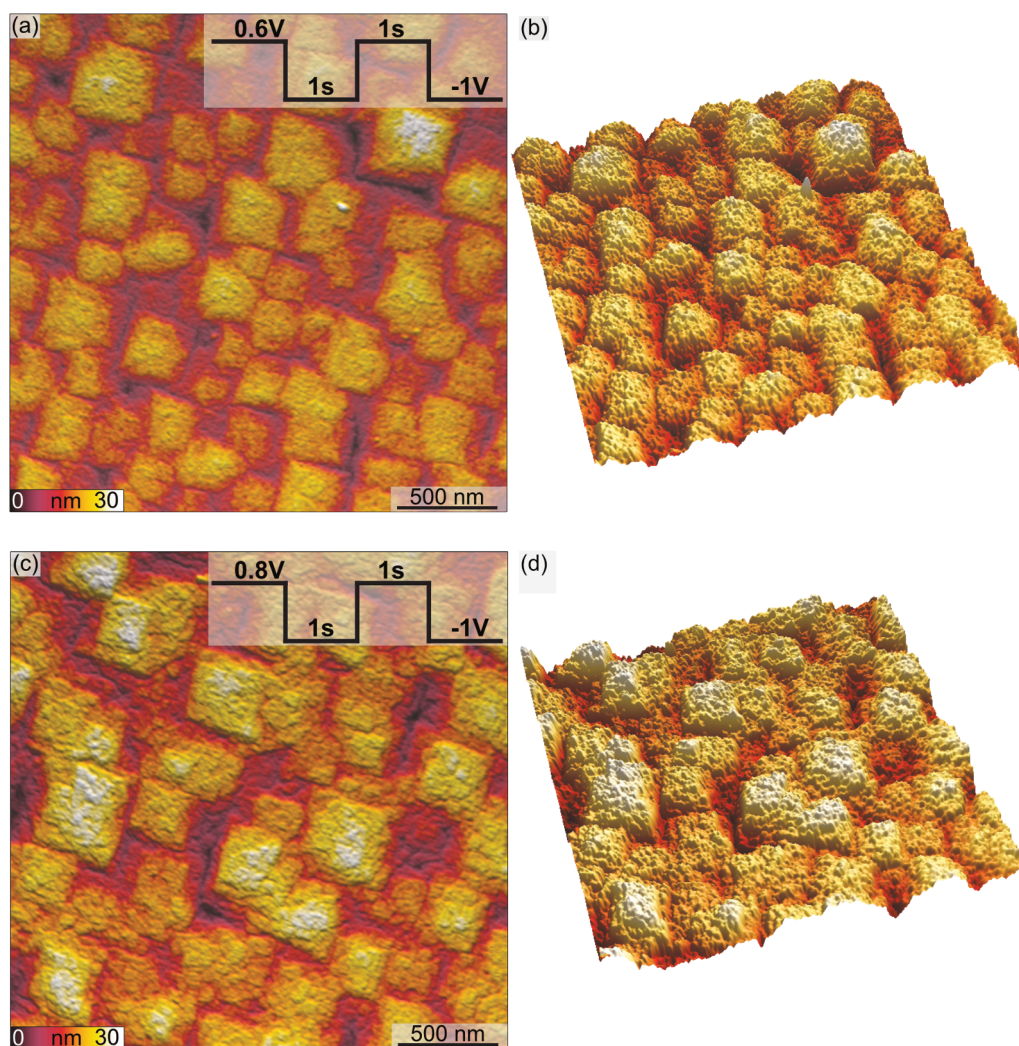


Figure 29: AFM images (a,c) and 3D representations (b,d) of UHV prepared Cu(100) surfaces after 1 h of pulsed potential sequences at anodic potentials of (a,b) 0.6 V vs. RHE and (c,d) 0.8 V vs. RHE in 0.1 M KHCO_3 . The crystals were transferred from UHV to the electrochemical cell without exposure to air.

The two pulse regimes with lower anodic potentials differ from each other and the higher anodic potential pulses. In figure 30 (a) and (b), the case for a sample pulsed at anodic 0 V vs. RHE is shown. We found steps in AFM, and the surface appears granular, but with deeper, meandering grooves and pits. Also, large particles of about 18 nm height are covering the surface. The latter might be due to the amount of pits on the surface, which can stabilize the particles even when rinsed with water. Interestingly, the stepped surface is clearly visible on the sample shown in figure 30 (c) and (d), i.e. the sample treated with an anodic

potentials of 0.4 V vs. RHE. While the surface exhibits similar granular roughness as in the potentiostatic case (fig. 28), we can clearly make out individual steps and terraces.

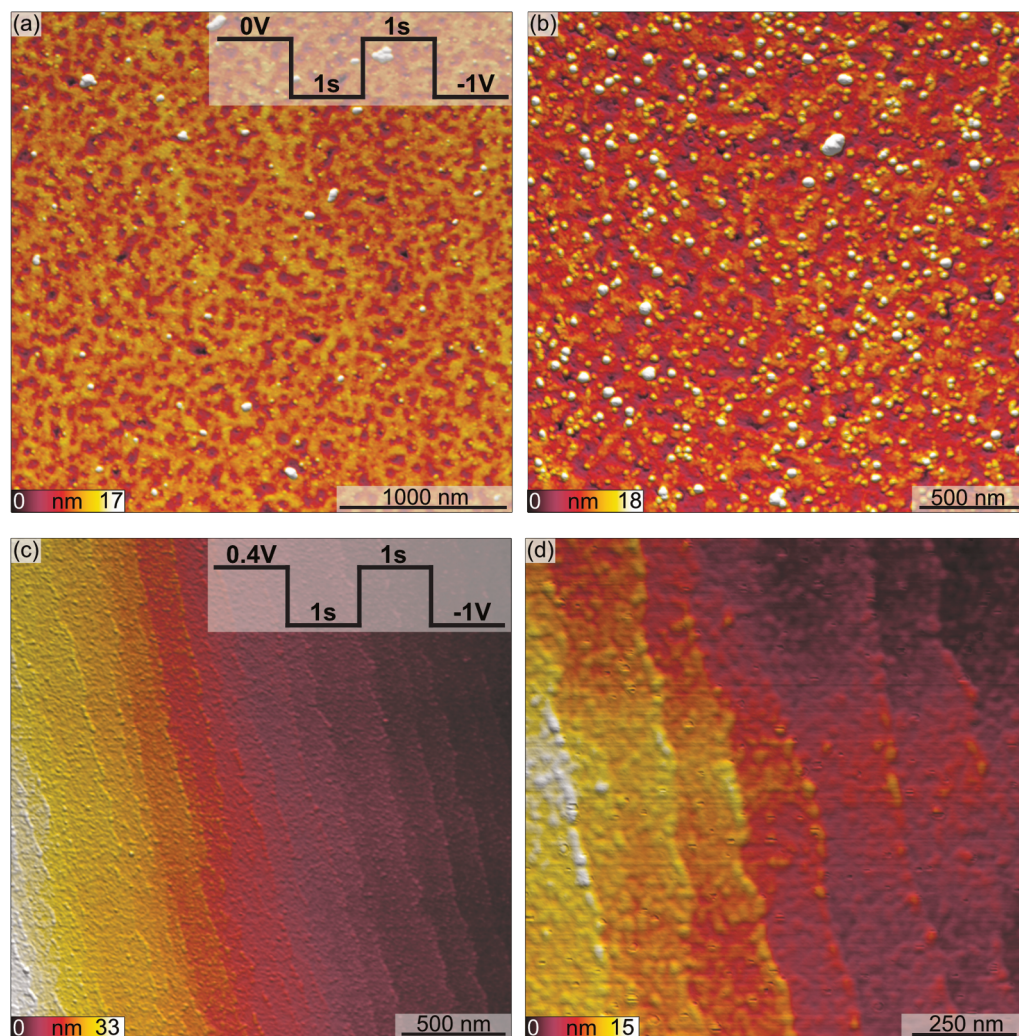


Figure 30: AFM images of UHV-prepared Cu(100) surfaces after 1 h of pulsed potential sequences at anodic potentials of (a,b) 0 V vs. RHE and (c,d) 0.4 V vs. RHE. Each experiment was conducted in 0.1 M KHCO_3 . The crystals were transferred from UHV to the electrochemical cell without exposure to air.

The retained stepped surface of the anodic potential of 0.4 V infers that the processes during cathodic and anodic pulse are balanced against each other around this potential, resulting in an effective equilibrium.

4.3.4 Surface structure dependency on pulse duration

After establishing the potential regimes and their corresponding surface alterations at a fixed pulse duration of 1 s each, we can look into the effect of the length of the pulse, i.e., the duration dependency. We therefore changed the duration of the cathodic pulses, whilst keeping the potentials the same at -1 V vs RHE.

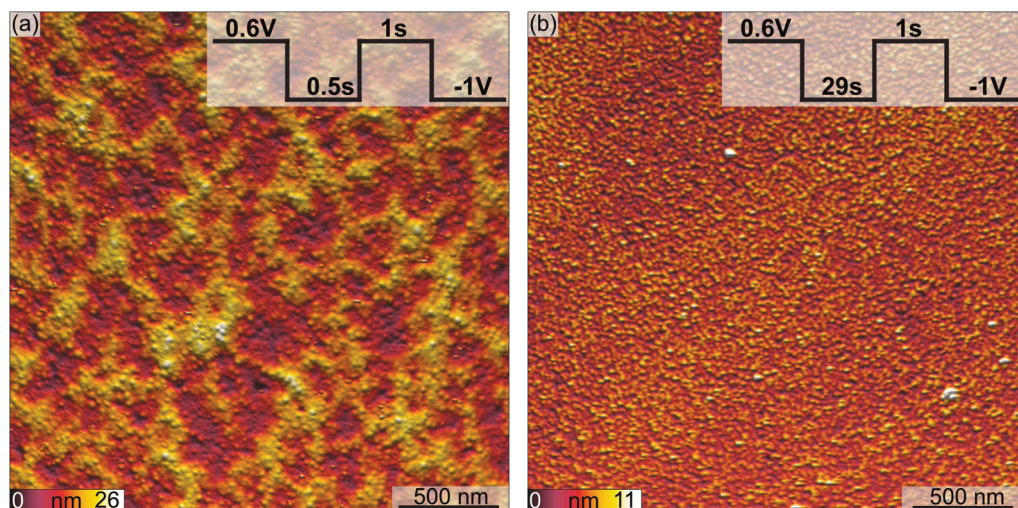


Figure 31: AFM images of UHV prepared Cu(100) surfaces after 1 h of pulsed potential sequences at cathodic potentials durations of (a) 0.5 s and (b) 29 s, with anodic potentials of 0.6 V and cathodic potentials of -1 V vs RHE in 0.1 M KHCO_3 . The crystal was transferred from UHV to the electrochemical cell without exposure to air.

In figure 31, AFM images of samples subjected to shorter (a) and longer (b) anodic pulse regimes are shown. In the case of (a), shorter pulses, we find a granular surface with larger valleys, without the cubic structures seen for the isochronous pulses. On the other hand, very long cathodic pulses of 29 s result in a flat surface equal to that of the potentiostatically treated sample (figure 28), densely covered in granular particles.

4.3.5 *Stability of the cubic motif in CO₂RR conditions*

To understand whether the extreme structural changes for the higher anodic potentials of 0.6 V would affect measurements of the catalyst performance during the CO₂RR, we also investigated the stability of the cubic motif by measuring the surface morphology after a subsequent, 1 h long electrolysis at a fixed potential of −1 V vs. RHE in 0.1 M KHCO₃ to simulate a typical CO₂RR experiment.

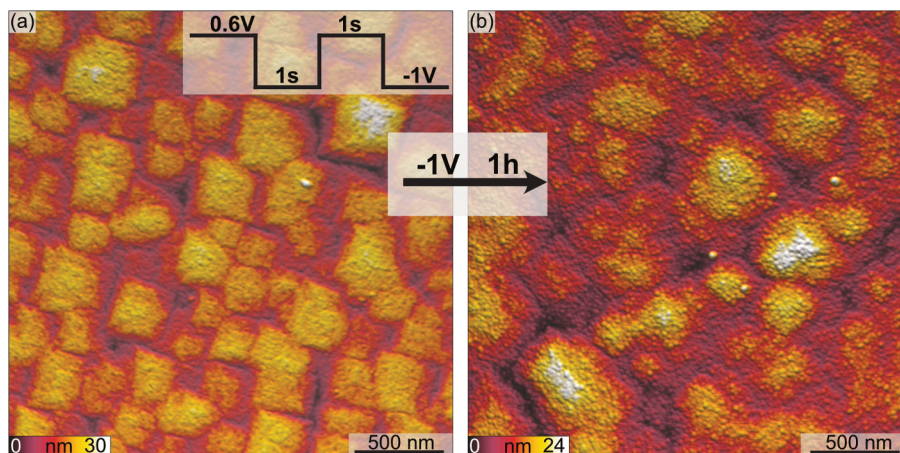


Figure 32: AFM images of the UHV prepared Cu(100) surface after 1 h of (a) pulsed potential sequences at an anodic potential of 0.6 V vs. RHE and (b) immediate subsequent electrolysis at −1 V vs RHE in 0.1 M KHCO₃ for a duration of 1 h. The crystal was transferred from UHV to the electrochemical cell without exposure to air.

We found that, once the cubic motif has formed, it remains semi-stable under CO₂RR conditions. Figure 32 (b) shows the effect of 1 h @ −1 V vs. RHE on the cubic motif. The overall motif is still clearly discernible, although the cubic structures appear to be more diffuse and shallower, with decreased heights. The cubes and the substrate which is visible between individual cubes are covered in granular particles, similar in shape and form as those observed in figure 28. This implies that the granular roughness after CO₂RR is a general consequence, independent of previous surface preparation.

4.4 Summary

Here, we systematically studied the effects of several (electrochemical) treatments on the surface structure of UHV prepared Cu(100). We found that an ideal surface obtained by UHV preparation is stable under ambient conditions, and even after a short electropolishing, the mesostructure of the surface is still discernible. The latter however results in a surface with more defects in the form of pits.

In 0.1 M KHCO_3 , we find that the UHV prepared Cu(100) surface is covered by nanogranular particles after 1 h of CO_2RR at -1 V vs. RHE. This nanogranularity appears not to be dependent on the pre-treatment, but a more generalized consequence of the CO_2RR conditions, since we also see this on strongly pretreated samples that start with a cubic motif.

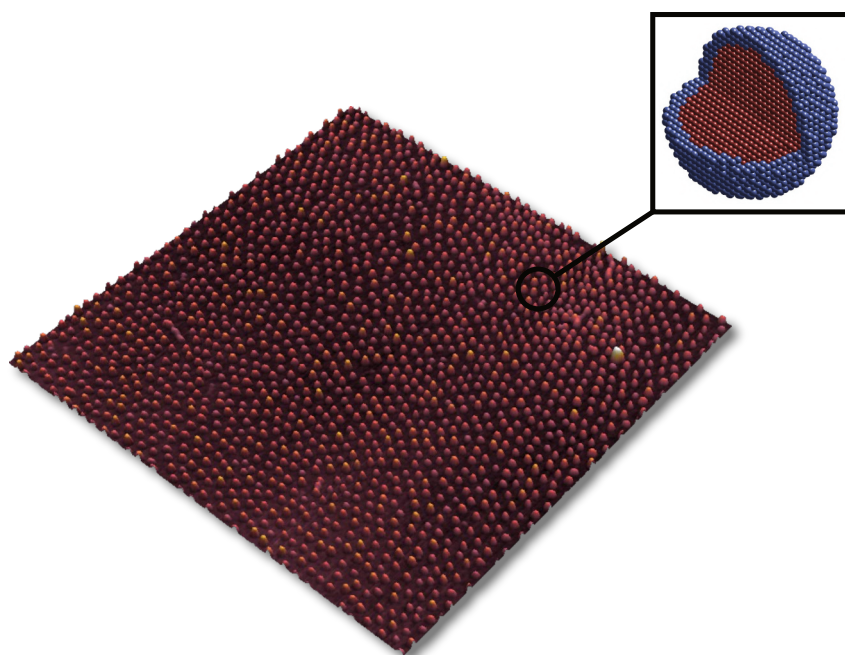
We have identified three groups of potentials for sequences with the same duration of cathodic and anodic pulses of 1 s each. At an anodic potential of 0 V, we find a rough surface with no ordered structure. For 0.4 V, we found that the stepped surface from the UHV preparation is retained, which suggests that with these conditions an equilibrium is reached. The two higher anodic potentials 0.6 V and 0.8 V result in the formation of cubic motifs, with the evolution of 30 nm height cubes that populate the surface.

Anisochronous pulses with shorter or longer cathodic potential durations do not lead to the cubic structures, but rather result in unordered, rough surfaces.

The insights into the induced structural changes of single crystal surfaces we obtained here are valuable results for future experiments on structure-activity studies, and allow to draw more accurate conclusions when their influence is necessary to consider.

Chapter 5

Operando NRIXS and XAFS Investigation of Segregation Phenomena in Fe-Cu and Fe-Ag Nanoparticle Catalysts during CO₂ Electroreduction



5 *Operando* NRIXS and XAFS

Investigation of Segregation

Phenomena in FeCu and FeAg

Nanoparticle Catalysts during CO₂

Electroreduction

The content of this chapter consists of material published in S. Kunze, P. Grosse, M. Bernal Lopez, I. Sinev, I. Zegkinoglou, H. Mistry, J. Timoshenko, M. Y. Hu, J. Zhao, E. E. Alp, S. W. Chee, B. Roldan Cuenya, *Angew. Chem. Int. Ed.* 2020, 59, 22667 .¹⁰⁹

Changes to the structure were made to better fit within the format of this thesis. Specifically, critical content from the supporting information that was referred to in the main text was integrated. Content from the supporting information of secondary importance is available in the appendix in section 9. Furthermore, a paragraph to transition from the previous chapter was added to the introduction of this chapter. No content altering changes were made. TEM measurements were done in cooperation with S. W. Chee. The EC measurements were done in cooperation with M. Bernal Lopez and P. Grosse. NRIXS measurements were done in cooperation with I. Zegkinoglou, I. Sinev, H. Mistry, M. Y. Hu, J. Zhao, E. E. Alp and B. Roldan Cuenya. EXAFS measurements were done in cooperation with M. Bernal Lopez, I. Sinev and P. Grosse, and the analysis carried out under supervision of J. Timoshenko.

5.1 Introduction

While we have demonstrated the use of scanning probe microscopy methods for morphology determination in chapters 3 and 4, there are limits to their application under reaction conditions. The nature of the method limits the structural analysis to the surface, and is further impeded by the fact that rough surfaces cannot be reliably imaged. In addition, measurements with applied potentials are especially difficult once gas evolution occurs, which leads to bubble formation that makes continuous measurements impossible. The probe itself might also induce changes in the local area of interest, such as when a bias is applied between the tip and the surface in electrochemical STM, or laser induced reactions during AFM investigations.

But besides experimental difficulties, there is an inherent aspect to consider: Changes inside a material are not accessible to us by SPM methods. While electrochemical processes revolve around the surface, the near-surface area is also of interest, since it can affect the surface state through electronic effects or strain. In this case, we want to use bimetallic nanoparticles, in sizes that essentially result in the entirety of the particle being 'near surface'. To accurately describe them, we are in need of determining the material distribution inside the particles.

Here, we illustrate the use of a spectroscopy technique instead of microscopy methods to investigate structural changes in bimetallic nanoparticles during an electrochemical reaction. We were able to monitor these even for this complex system. Indeed, one of the most significant challenges in the field of catalysis is the development and optimization of experimental methods that allow the observation of a catalyst while at work.^{110–112} This is especially difficult when nanomaterials are considered under realistic conditions, as for example, when trying to understand atomic segregation phenomena and other structural/chemical modifications at liquid/solid interfaces during an electrochemical process.¹¹³ A number of established methods are not directly applicable under reaction conditions due to decreased electronic mean free paths, scattering or lack of sufficient spatial resolution or chemical sensitivity. The development of additional tech-

niques suitable for *operando* implementation in an electrochemical environment is therefore a subject of high interest.^{114,115}

As described in chapter 2, nuclear resonant inelastic X-ray scattering (NRIXS) is a synchrotron radiation technique that is sensitive to vibrational states of the nuclei of Mössbauer-active isotopes, most commonly ^{57}Fe .¹¹⁶ It can be used to probe vibrational modes of molecular complexes of iron as well as phonons in solid state materials.⁵⁰ Because the vibrational modes of a crystal lattice depend heavily on its structure, it is possible to relate NRIXS data to structural and thermodynamic properties of a material.⁴⁹ Moreover, due to the isotope-specific detection, one can probe only a specific region of a sample if enriched with the Mössbauer-sensitive element, while the overall structure can be inferred indirectly from the contribution of the partial ^{57}Fe -phonon density of states (PDOS).^{48,117} More importantly, this method can be used to investigate a wide range of materials from bulk materials to thin-films and NPs in experiments under extreme conditions such as high-pressure environments or during thermal or electrochemical catalytic reactions.^{118–121}

In the following study, the NRIXS method was used to follow the structural and chemical evolution of small ^{57}Fe -containing bimetallic NPs in a liquid environment under an applied external potential during CO_2RR . XAFS, another synchrotron technique with high sensitivity to elemental and local structural composition was also applied here under reaction conditions in an electrochemical environment to complement the NRIXS insight, including providing information on the Ag and Cu components of the synthesized electrocatalysts.¹²²

Iron-based materials were used in this study due to their applications as heterogeneous catalysts in the field of sustainable energy conversion. Iron is an abundant metal with little environmental impact, though it is unsuitable for CO_2RR in its bulk form, since it favors the parasitic hydrogen evolution reaction (HER).²⁵ Nevertheless, if present in the NP form at the core of nanostructures with a CO_2RR -active thin shell, it could contribute to a decrease in the catalyst price. To date, research on iron-based materials for CO_2RR focuses mainly on molecular complexes, as for example Fe-N-C materials in porphyrin-like

structures.^{123,124} Here, iron is combined with copper and silver within a micellar nanoreactor since these elements are promising for the selective conversion of CO₂ to C₁-C₃ products (Cu) and CO (Ag).²⁵ In this project, the structure and composition of the FeCu and FeAg catalysts during the reaction will be extracted from a synergistic combination of *operando* NRIXS and XAFS measurements and correlated with the selectivity trends of monometallic Cu, Ag and Fe NPs of similar size.

5.2 Experimental Details

Inverse micelle encapsulation was used to prepare colloidal solutions of size-selected, isolated Fe, FeCu, FeAg, Ag and Cu NPs.^{125,126} Two sets of NPs were synthesized by loading a nonpolar/polar diblock copolymer [poly(styrene)-block-poly-(2-vinylpyridine), Polymer Source Inc.] dissolved in toluene with metal salts (⁵⁷FeCl₂ · 2 H₂O, AgNO₃, CuCl₂ · 2 H₂O, FeCl₃). One of the NP sets synthesized contained the isotopically enriched ⁵⁷FeCl₂-salt needed for the NRIXS measurements, Table 1. The enriched iron salt was synthesized from an iron foil with 95 % ⁵⁷Fe isotopic enrichment by adapting a procedure described in the literature.¹²⁷ A 0.2 metal loading (metal/P2VP molecular weight ratio) was used in the synthesis of the micellar samples. Samples for NRIXS and XAFS measurements (⁵⁷Fe, ⁵⁷FeCu, ⁵⁷FeAg) were prepared by impregnating the NP solution on carbon black powder (5wt%). An N₂-plasma treatment was used for polymer removal on the impregnated powders (300 mTorr, 20 W, 5 cycles of 10 min duration) as well as on samples dip-coated on silicon wafers used for the AFM analysis (300 mTorr, 20 W, 20 min). The NP powder (5mg-10mg) was then dispersed in an ethanol/naion solution. The former solution was deposited on a low-porosity carbon paper disc (Sigracet SGL 24 AA, SGL Carbon GmbH) by filtration, during which the catalyst powder stays on one side, bonded by naion, while the other side is not modified. These carbon paper samples were used in order to minimize the signal attenuation for *operando* NRIXS and XAFS measurements, since our cell is designed such that the sample is irradiated from the back, and the subsequent fluorescence signal is also collected from the back. Finally, Fe, FeCu, FeAg, Ag and Cu samples were prepared

for electrochemical characterization in our laboratory by two successive cycles of dip-coating the bimetallic NP solution (nafion-free) on fresh glassy carbon electrodes and subsequent a N_2 plasma treatment (300 mTorr, 20 W, 2x20 min) was employed for polymer removal.

Tapping Mode atomic force microscopy (AFM) (Bruker, Multimode 8) images were acquired on samples supported on $SiO_2/Si(100)$ after polymer removal. The apparent NP height was used to determine the NP size and distribution. We used the Gwyddion software package to analyze the height maps.⁸¹ STEM-EDX measurements of supported micellar NPs, dispersed in ethanol and drop-casted on 5nm amorphous Si TEM windows, were carried out in a JEOL ARM 200F microscope. We employed our XPS setup (SPECS GmbH, a non-monochromatic source, Al K-edge @ 1486.6 eV) to determine the different metal ratios in the bimetallic NPs.

The laboratory-based CO_2 RR characterization was carried out in a gas-tight H-type cell. A Selemion ion exchange membrane (AGC Engineering Co., Ltd.) separated the two compartments, which were filled with 40 ml 0.1 M $KHCO_3$ (Sigma Aldrich, 99.7%). A three-electrode setup with a platinum mesh counter electrode (MaTeck, 3600 cm^{-2}), leak-free Ag/AgCl/3.4 M KCl reference (Innovative Instruments Inc.) and the glassy carbon sample acting as the working electrode (4.4 cm^2 exposed area) were employed. A CO_2 flow of 20 ml min^{-1} was used during the measurements and for purging. The potential was controlled by a Metrohm-Autolab (M204) potentiostat with corrected iR drop. Gas analysis was done online by a Shimadzu 2014 Gas-Chromatograph with HayeSepQ + HayeSepR packed columns and a flame ionization detector (FID) for hydrocarbon separation and detection. An MS-13X column and thermal conductivity detector (TCD) were used for the detection of H_2 , N_2 and O_2 , while CO and CO_2 were methanized before detection by the FID. Liquid products such as formate were analyzed with a high-performance liquid chromatograph (Shimadzu Prominence HPLC) with a NUCLEOGEL SUGAR 810 column and a refractive index detector (RID). Alcohols were analyzed with a liquid GC (Shimadzu 2010 plus) with silica

column and FID. Product selectivities were calculated with product distribution and current data obtained after 1 h of reaction.

Operando XAFS and NRIXS measurements were performed in a home-made electrochemical cell (described in chapter 2). During both measurements, CO₂ was dosed to the electrolyte (0.1 M KHCO₃) solution (20 mL/min) and a potential of -1.1 V vs RHE was applied. The same three-electrode setup as described above was employed. A potentiostat EmStat 3 from PalmSense was used to control the applied potential. The XAFS experiments were performed at the SAMBA beamline at the SOLEIL synchrotron. Data at the K-edges of Cu, Fe and Ag were collected, using a Si(220) monochromator for energy selection. The measurements were performed in fluorescence mode using a 13-channel Ge detector. The NRIXS experiments were performed at the 3-ID-B beamline at the Advanced Photon Source (APS) of the Argonne National Laboratory. The beamline features a monochromatic beam at 14.41 keV with an energy resolution of 1 meV. Analysis of the NRIXS data was done with the PHOENIX software from W. Sturhahn.¹²⁸ XAFS data were processed and analyzed with the ATHENA and ARTEMIS modules of the Demeter software package, using a FEFF6 code.¹²⁹

STEM-EDX measurements of supported micellar NPs, dispersed in ethanol and drop-casted on 5 nm amorphous Si TEM windows (from the supplier TEMwindows), were carried out in a 200 kV JEOL ARM 200F microscope. Pristine 'as-prepared' NPs (deposited and calcinated on nanocrystalline SiO₂) and NPs that were used in the CO₂RR synchrotron experiments (deposited on carbon black powder and bonded with Nafion) were measured. The latter samples were scratched off from the carbon paper electrode, and then drop-casted on the TEM grid.

5.3 Results and Discussion

AFM images of the ^{57}Fe , $^{57}\text{FeCu}$ and $^{57}\text{FeAg}$ NPs and their non-enriched analogues deposited on $\text{SiO}_2/\text{Si}(100)$ are shown in Fig. 33. The corresponding height histograms can be found in figure 34. Well dispersed, size-selected NPs with average size (NP height) under 8 nm were obtained with the micellar synthesis.

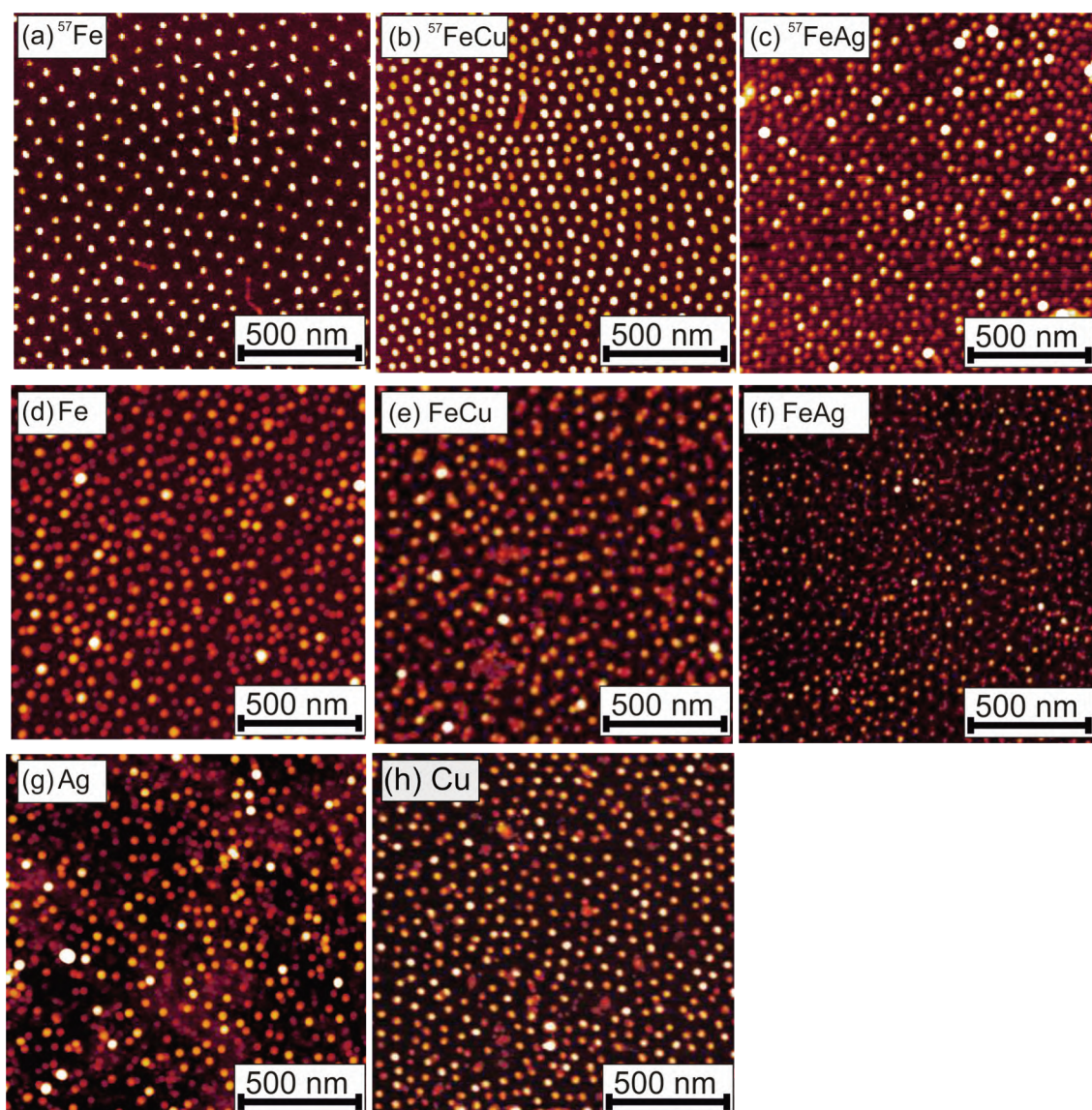


Figure 33: Tapping mode AFM images of: (a) ^{57}Fe , (b) $^{57}\text{FeCu}$, (c) $^{57}\text{FeAg}$ NPs deposited on $\text{SiO}_2/\text{Si}(100)$ after a N_2 plasma treatment for polymer removal. Average particle sizes are: 7.8 nm for ^{57}Fe , 5.2 nm for $^{57}\text{FeCu}$ and 4.2 nm for $^{57}\text{FeAg}$. Panels (d) to (h) show analogous images of the non-enriched NPs.

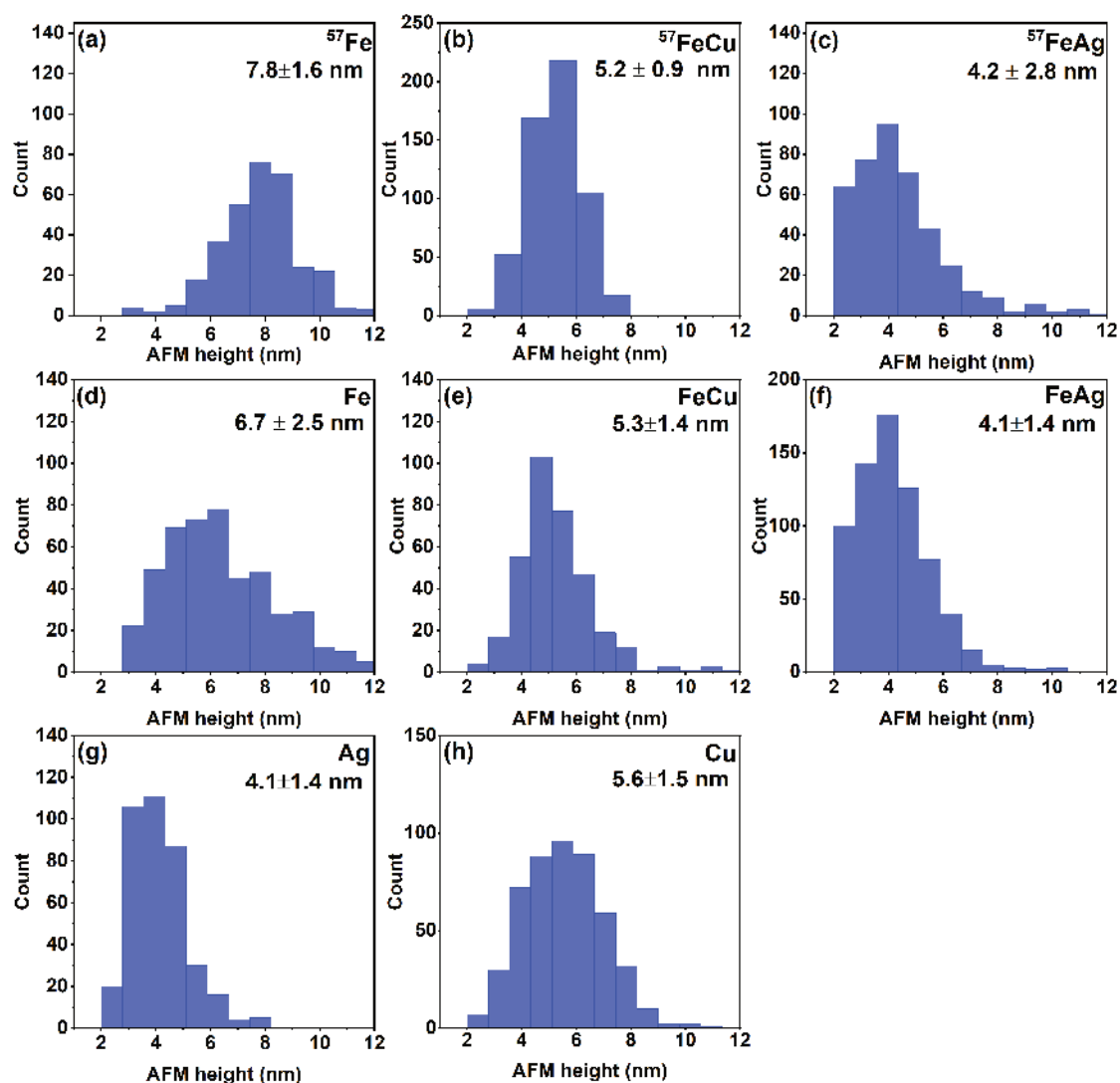


Figure 34: Size histograms of the nanoparticle arrays shown in Fig. 33.

STEM-EDX measurements show that both metals are indeed present in our NPs, as seen in figure 41.

XPS spectra of the Fe-2p region of the as-prepared bimetallic NPs deposited on a SiO₂/Si(100) substrate and the corresponding fits displaying the different Fe oxidation states are shown in Fig. 35. Additional XPS data from the Cu-2p and Ag-3d regions are shown in figure 36. It is evident that the iron in the NPs after synthesis, N₂-plasma treatment and subsequent air exposure is almost completely cationic (Fe²⁺ or Fe³⁺, see Table S1 in the Addendum). A strong Fe-2p satellite is apparent in the FeCu spectrum, which has previously been reported

for oxidized iron in the presence of copper.¹³⁰ The Fe:Cu ratio was calculated as 55:45. The Ag-3s peak in FeAg overlaps with the Fe-2p region, which we compensated for, when we calculated the Fe:Ag ratio of 64:36. Due to the small size of the nanoparticles, we expect the entire particle volume to be probed by XPS.

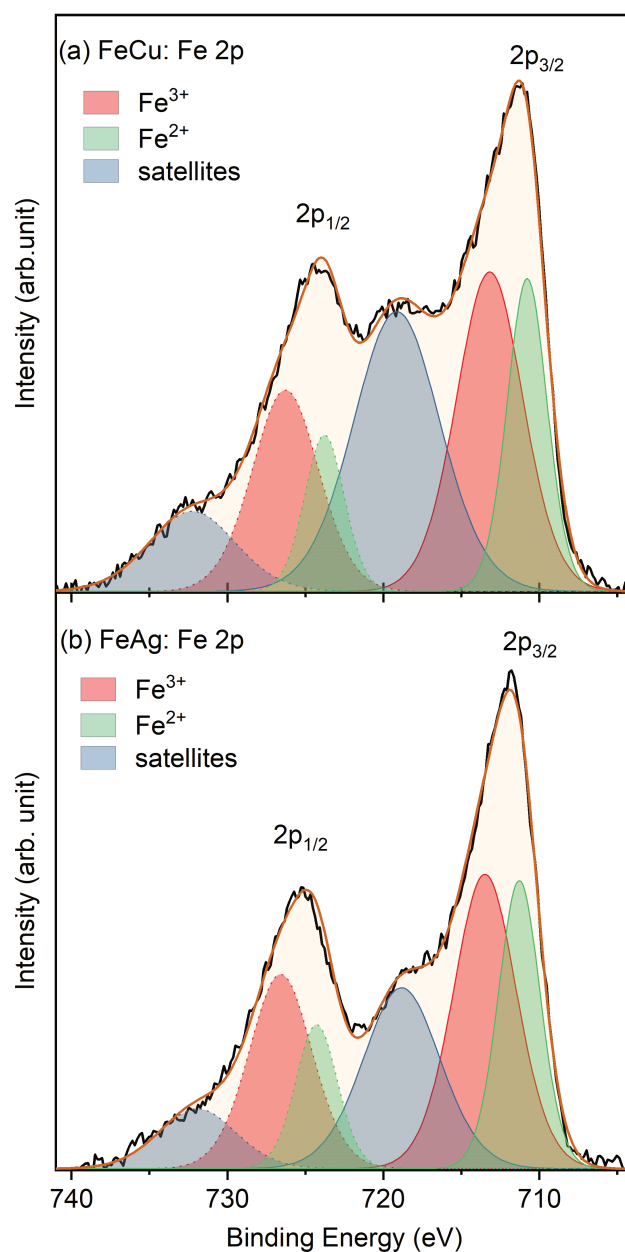


Figure 35: Background-subtracted XPS spectra and corresponding fits of the Fe-2p core level region of as-prepared (a) FeCu and (b) FeAg NPs supported on SiO₂/Si(100).

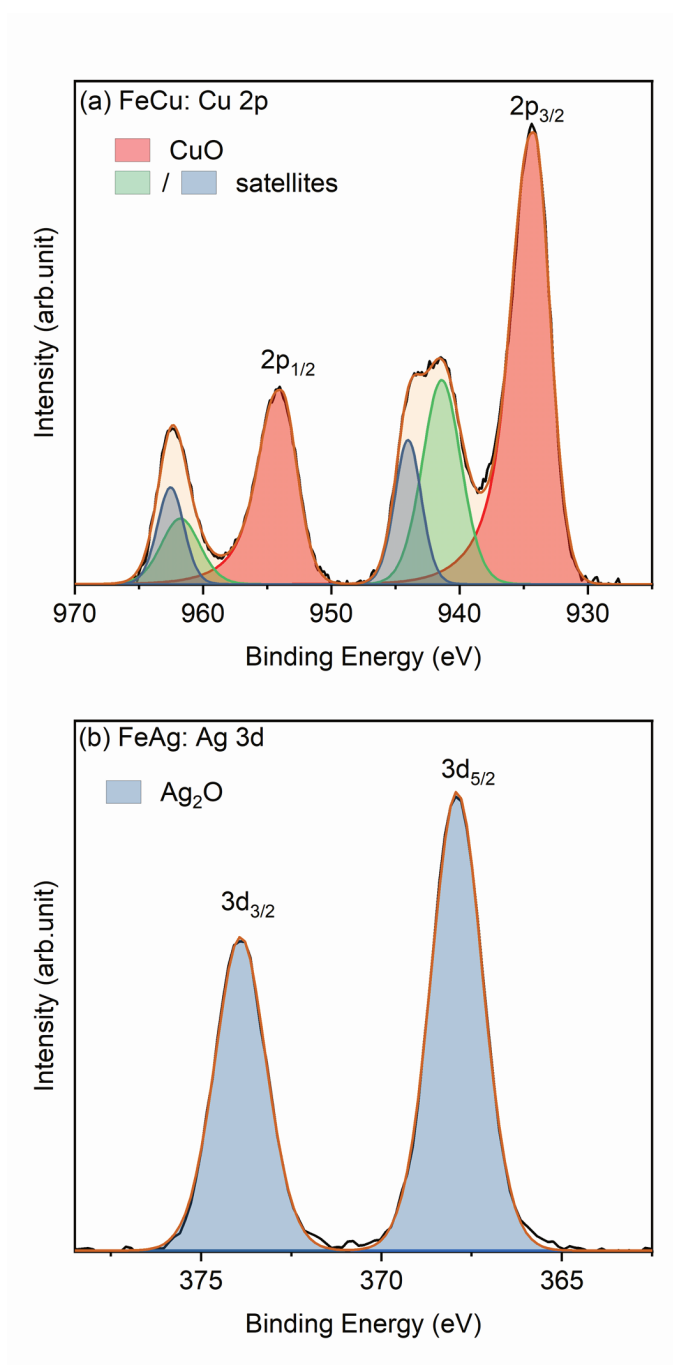


Figure 36: Background-subtracted XPS spectra of the (a) Cu-2p and (b) Ag-3d core level regions of FeCu and FeAg NPs deposited on SiO₂/Si(100).

The product selectivities and current densities of our Fe, FeCu, FeAg, Ag and Cu NP samples are shown in Fig. 37.

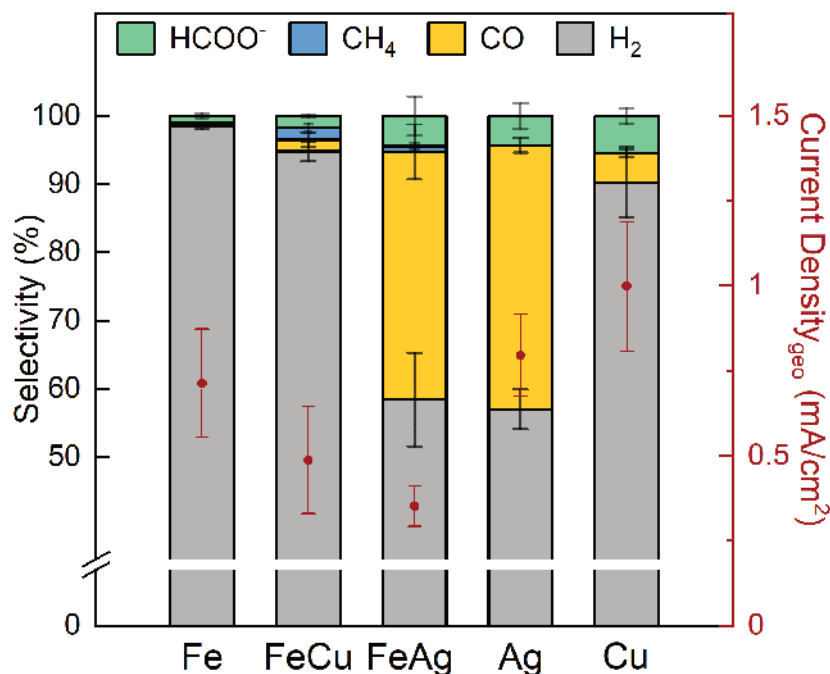


Figure 37: Selectivity for the reaction products of CO₂RR obtained from Fe (6.7 nm), FeCu (5.3 nm), FeAg (4.1 nm), Ag (4.1 nm) and Cu (5.6 nm) NPs after 1h of reaction at -1.1 V vs RHE in CO₂-saturated 0.1 M KHCO₃ and a CO₂ flow of 20 mL/min. Plotted in red are the geometric current densities of each sample (right-hand side red scale).

While hydrogen is the main product for all samples, the selectivities for CO of the FeAg and Ag NPs are similar (36 % and 39 %, respectively) at -1.1 V vs RHE. This similarity is consistent with a core-shell rearrangement of the FeAg NPs under reaction conditions, with Ag at the NP surface and Fe at the core. The FeCu NPs also produce CO, but with a lower selectivity of under 2 %. In contrast to FeCu, both CO and formic acid selectivity are higher in the pure Cu NP sample with 4.2 % and 5.5 %, respectively. This is likely indicative of a more Fe-rich surface in the FeCu NPs. As expected, no higher hydrocarbons or alcohols were detected in either of the FeCu or Cu NP samples, contrary to the case of bulk Cu, due to the enhanced number of low-coordinated surface

sites on small NPs that are known to favor the HER.^{36–38} Methane however is a product for all iron-containing samples here, albeit with very low selectivity ($< 1.7\%$), but not for pure Ag or Cu NPs. Such production might be also affected by the NP size, since bulk iron is not known to yield methane.^{25,124} The methane production in the case of the FeAg samples might be explained due to the presence of an incomplete (non-uniform) Ag-shell, leaving exposed small areas of the Fe core which might lead to a synergistic interaction between Fe and Ag. We observed only low amounts of C1 products typical of bulk Cu electrodes (CH_4 , CO, HCOO^-) for FeCu.²⁵ The pure iron sample produced overwhelmingly hydrogen as its main product, with only traces of formic acid and methane. Besides CO and hydrogen, the silver NPs were also found to produce formic acid (4.3 % selectivity), similar to the FeAg NPs with about 4.4 %.

The current densities normalized to the geometric area of the sample for the Fe, FeCu, FeAg, Ag and Cu NP samples are: 0.71 mA cm^{-2} , 0.49 mA cm^{-2} , 0.35 mA cm^{-2} , 0.79 mA cm^{-2} and 0.99 mA cm^{-2} , respectively. A possible explanation for the lower current density, as well as slightly lower CO selectivity of the FeAg sample as compared to pure Ag, is the compressive strain induced by the smaller iron core on the silver overlayer. A shift of the d-band center away from the Fermi level, caused by compressive strain, is expected to influence the CO bonding strength negatively, leading to a more favorable H_2 production.

NRIXS measurements were carried out before (^{57}Fe , $^{57}\text{FeCu}$ in air) and *operando* under CO_2RR conditions in the electrolyte and under potential control (^{57}Fe , $^{57}\text{FeCu}$ and $^{57}\text{FeAg}$). Fig. 38 shows the corresponding Fe-partial PDOS of these samples.

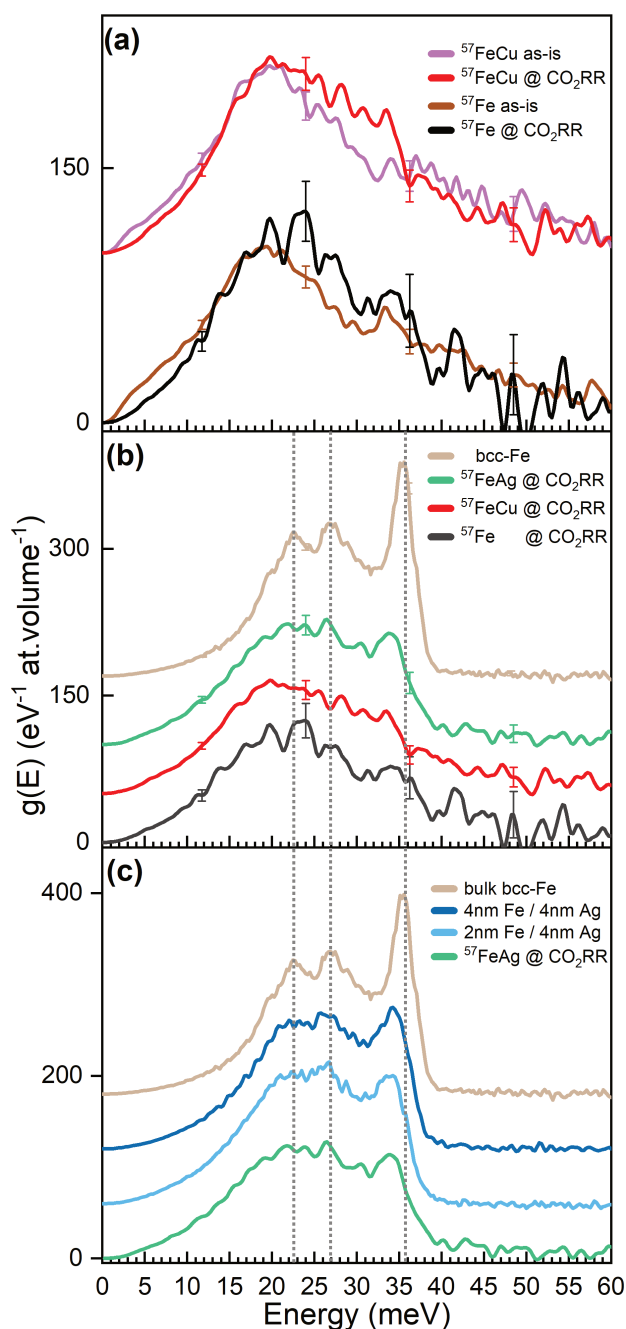


Figure 38: (a) ^{57}Fe -partial PDOS, $g(E)$, obtained from raw NRIXS spectra of ^{57}Fe and $^{57}\text{FeCu}$ NPs in air and under *operando* CO_2RR . The spectra in (b) display the *operando* CO_2RR PDOS data of ^{57}Fe , $^{57}\text{FeCu}$ and $^{57}\text{FeAg}$ NPs together with a bulk bcc-Fe reference foil for comparison.¹¹⁸ (c) ^{57}Fe -partial PDOS of $^{57}\text{FeAg}$ NPs plotted together with thin ^{57}Fe layers deposited on a Ag film (4 nm) reproduced from Ref.¹¹⁸ Representative error bars in different regions of the spectra are also shown. The spectra have been vertically offset for better visibility and the vertical lines indicate the position of the two TA and the LA peaks of bulk bcc-Fe.

The spectrum from a bulk bcc-Fe foil is also shown for reference. The spectra recorded in air indicate enhanced atomic disorder and oxidic Fe features at 41 meV-43 meV that are at least partially reduced under reaction conditions, figure 38(a). The longitudinal acoustic (LA) phonon peak near 36 meV observed in bulk bcc-Fe becomes also visible in the NP phonon spectra under reaction conditions. Nevertheless, it appears shifted to lower phonon energies (by 1.3 meV to 2 meV, see appendix) in both of the bimetallic samples due to the presence of the phononically softer Ag and Cu metals in the Fe environment. Furthermore, significant damping is observed in the LA peak of the three NP samples as compared to that of bulk bcc-Fe due to size-effects. Interestingly, the PDOS of the $^{57}\text{FeAg}$ NP sample shows the most clear resemblance to that of bulk bcc-Fe, since for that sample the LA peak is more prominent and we also see the transverse acoustic (TA) phonon modes, enhanced ordering (as indicated by sharper features), and the absence of oxidic species under the reducing conditions available during CO_2RR . Such observations point towards a significant reduction of the FeO_x species when the potential is applied in parallel to the segregation of Ag to the NP surface and the formation of a protective Ag shell and a “pure” bcc-Fe NP core. For the pure ^{57}Fe NPs we still observe hints of the incomplete FeO_x reduction under reaction conditions and enhanced disorder (smeared lines). The $^{57}\text{FeCu}$ NPs look more disordered and the Fe-partial phonon DOS has a larger deviation with respect to that of pure bcc-Fe, figure 38(b), indicating some degree of Fe-Cu intermixing. Nevertheless, a Cu-rich surface is still expected since the PDOS of this sample is still in close agreement with that of pure bcc-Fe aside from the size-dependent phonon damping and enhanced disorder. Such spectra are also seen for thin Fe layers in the proximity of metals with a lower phonon cut-off energy, as is the case here for both, Cu and Ag.¹²⁰ Overall, the PDOS corresponding to the FeAg and FeCu NP samples acquired under CO_2RR approaches a bcc-Fe structure, not fcc-Fe as could be expected if Fe would be embedded in the fcc-Cu or fcc-Ag matrixes.¹³¹ It should be noted that the relative content of Fe in the as prepared FeCu and FeAg NPs is similar according to XPS, namely 55 % and 64 %.

The Fe/Ag is a layered system known for a low interfacial intermixing. The PDOS of the NPs in this sample displays analogous characteristics to that of a Fe/Ag multilayer interface which was investigated by Roldan et al.¹¹⁸ Fig. 38(c) shows the Fe-partial PDOS data of this FeAg NP sample alongside PDOS data from Ref¹¹⁸. Apart from the overall shape and correspondence to a bcc structure, the position of the LA peak around 35.5 meV and the TA peaks (20 meV-30 meV) of the FeAg NPs are similar to those of the sandwiched Fe/Ag layers with Fe thicknesses of 2 nm - 4 nm. This is in accordance with the average particle size of the FeAg sample of about 4.2 nm (the real size of the iron part is smaller than this due to the bimetallic composition). An analogous comparison of the ⁵⁷FeCu NP sample under *operando* conditions with respect to Fe(1.5 nm)/Cu(4 nm) multilayers from Roldan et al.¹¹⁸ is displayed in the appendix in figure 49. While the LA peaks of the multilayer sample and the ⁵⁷FeCu NPs under *operando* conditions are similarly positioned (34.1 meV vs 33.7 meV) and shaped, corresponding to the bcc-Fe structure, there is a lack of unambiguous structural features in the TA region, indicating high disorder due to the small NP size and phonon softening caused by the Fe-Cu interaction.

XAFS data were also acquired under CO₂RR conditions using the same cell design and samples as in the NRIXS experiments in order to extract complementary information about the chemical state and structure of the samples, including their changes under reaction conditions. In this case, we could gain access not only to the Fe-component of the bimetallic systems, but also to the Ag and Cu constituents.

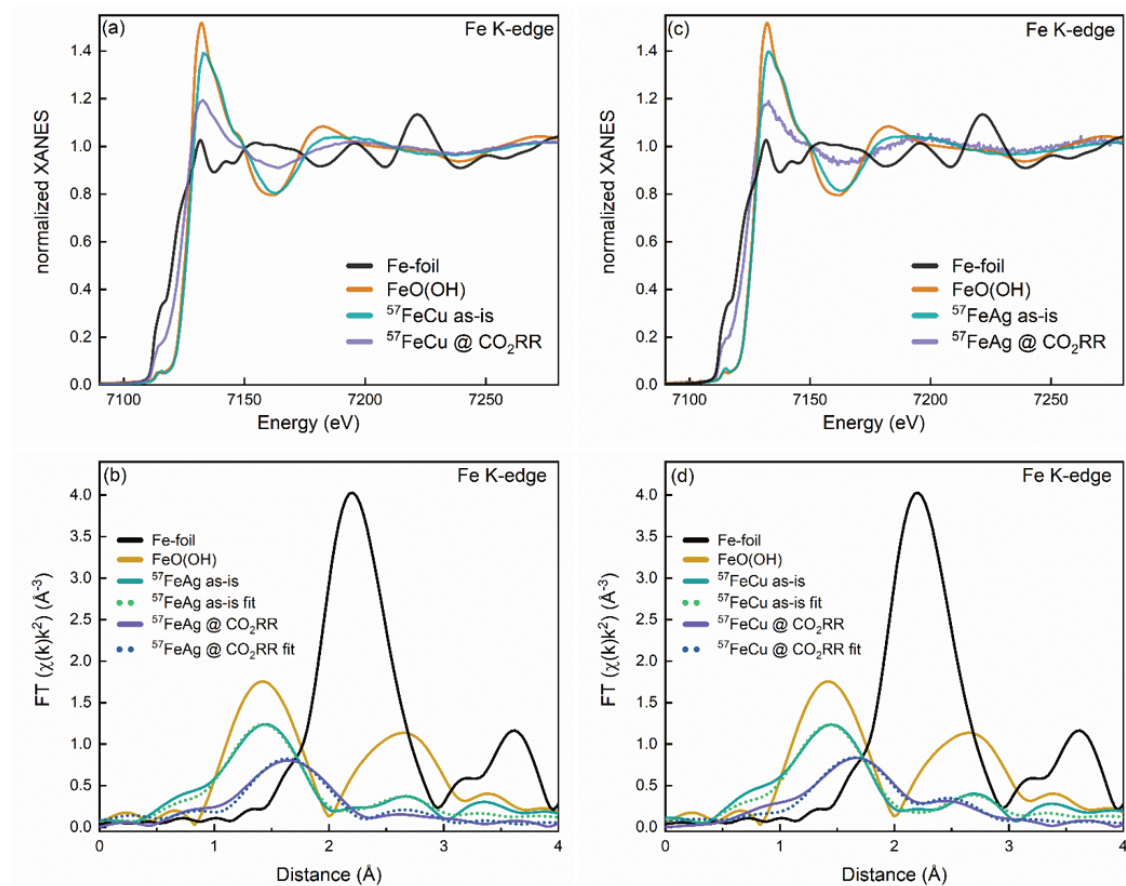


Figure 39: Fe K-edge XANES (a,c) and Fourier-transforms of k^2 -weighted EXAFS data (phase-uncorrected) and the corresponding first-shell fits (dotted lines) (b,d) of $^{57}\text{FeCu}$ and $^{57}\text{FeAg}$ NPs as prepared (as-is) and under CO₂RR conditions at -1.1 V vs RHE in 0.1 M KHCO₃ after 3.5 h ($^{57}\text{FeCu}$) and 1.5 h ($^{57}\text{FeAg}$). Reference spectra from lepidocrocite FeO(OH)¹²⁹ and a bulk iron foil are also shown for comparison.

It is evident from the XANES spectra in Fig. 39 (a) and (c) that the particles are in an oxidized state from the beginning, as they show typical oxidic features. For comparison with our oxidized particles, we chose here to show the spectrum for an iron mineral (lepidocrocite) that consists of a naturally occurring hydroxide/oxide mixture, since the initial particle composition after air exposure is likely a complex mixture as well. From Fig. 39 (b) and (d) we can conclude that the first coordination shell of our oxidized NP samples is similar to that in the reference mineral, but the mean Fe-O distance of 1.81(6) Å in our samples is smaller than the reference value of 2.00 Å.¹³² Table 3 summarizes further relevant parameters extracted from the EXAFS measurements, both for as-prepared samples and samples under CO₂RR conditions. Upon applying a potential of -1.1 V vs RHE, the particles start reducing to a more metallic state. However, we still see a significant contribution from oxidized iron species even under *operando* conditions. Some of these cationic species might also be assigned to iron compounds dissolved into the electrolyte.

We can show a reduction and increase in crystalline order in the iron component of the NP samples under reaction conditions that are in agreement with our previous NRIXS results. The *operando* XAFS measurements were acquired over periods of 1.5 h to 3.5 h of the reaction, while the NRIXS data were acquired over periods of 11 h to 18 h, which might also explain the higher apparent content of iron oxides in the XAFS data. The long acquisition times were needed due to the low count rates in the NRIXS experiment.

Figure 40 displays Cu K-edge (a,b) and Ag K-edge (c,d) XANES and EXAFS data of the ⁵⁷FeCu and ⁵⁷FeAg NP samples. The presence of oxidic copper compounds similar to CuO was observed, and a reduction of copper to the metallic state under *operando* conditions. The average interatomic distances for Cu-O in the as-prepared sample are in line with bulk CuO (Table 3). The time dependence of the reduction process (Fig. 50, appendix) reveals a fast initial CuO reduction, followed by a slower increase over the next 1.5h of the peak in the Fourier-transformed (FT) EXAFS at ca. 2.2 Å that corresponds to a contribution of the metallic Cu phase. For the as-synthesized samples, both XANES and

EXAFS data collected at the Ag K-edge and shown in Fig. 40(c,d), and indicate the presence of stable AgCl compounds due to residual Cl from the synthesis procedure. Upon applying the CO₂RR potential, a clear increase of the metallic silver contribution (peak in the FT-EXAFS at ca. 2.7 Å) is seen, and no other components could be fitted. There is no contribution from Fe-Ag scattering paths, and the Fe-Fe and Ag-Ag distances do not hint towards intermixing of Fe and Ag either, since they are in line with those for the corresponding bulk materials. In the case of the ⁵⁷FeCu sample, the Cu-Cu distance agrees with those in bulk Cu, while the Fe-Fe distance of 2.48(5) Å is in line with that of bulk Fe at 2.47(1) Å.¹³³

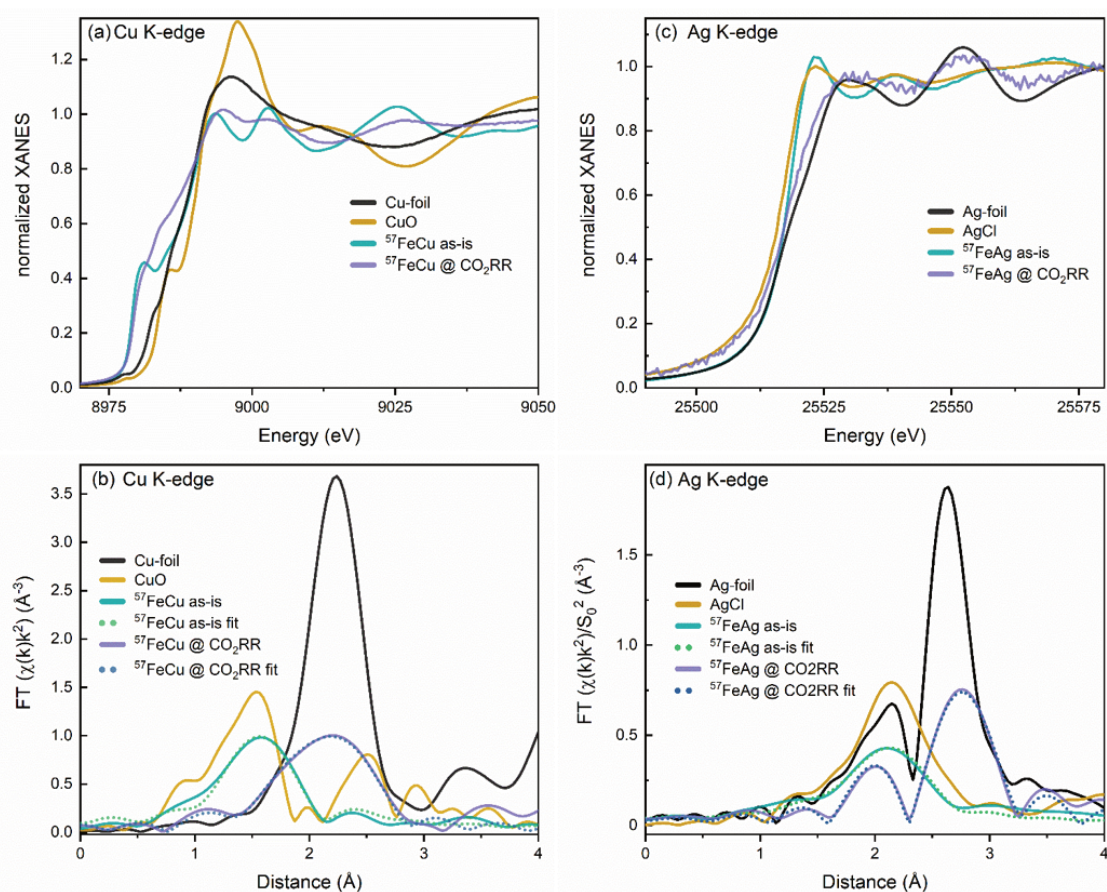


Figure 40: Cu K-edge (a,b) and Ag K-edge (c,d) XANES (a,c) and Fourier-transforms of k₂-weighted EXAFS data (phase-uncorrected) (b,d) of ⁵⁷FeCu and ⁵⁷FeAg NP samples in as-prepared state (as-is) and under CO₂RR conditions (-1.1 V vs RHE in 0.1 M KHCO₃ after 1.5 h (⁵⁷FeCu) and 2.5 h (⁵⁷FeAg)) Reference spectra from CuO, Cu-foil, AgCl¹²⁹ and a Ag-foil are shown for comparison.

After careful evaluation of the *operando* structural and chemical information extracted from two complementary synchrotron X-ray methods (XAFS and NRIXS), we demonstrate a significant reduction of iron oxide to metallic species under reaction conditions, accompanied by a structural transformation from an amorphous or atomically disordered phase to a crystalline structure. We observed a similar transformation for the secondary metals in the bimetallic NP samples via XAFS; a clear reduction of CuO to Cu in $^{57}\text{FeCu}$, and even more pronounced, AgCl to Ag transformation in $^{57}\text{FeAg}$. NRIXS served to distinguish segregated Fe-Ag and Fe-Cu phases (the present case) from alloyed structures, since we only detected a bcc-like Fe structure typical for a segregated Ag shell with bcc-Fe NP core. A small degree of Fe-Cu intermixing is obtained for the $^{57}\text{FeCu}$ sample from the XAFS data analysis. The bcc-Fe phase also predominates the NRIXS signal. Both these findings suggest the predominant segregation of both metals in our samples under CO_2RR conditions.

It should be noted that the X-ray-based spectroscopic methods employed here for the characterization of our nanosized electrocatalysts (NRIXS and XAS) also have limitations that need to be considered for the interpretation of the data obtained. For instance, both methods are bulk-sensitive ensemble-averaging techniques, i.e. the measured signal is an average of contributions from all metal species, residing both at the surface and in the core regions of all NPs within the X-ray irradiated sample area. Therefore, meaningful composition information can only be obtained when applied to multimetallic samples with an homogeneous inter- and intraparticle composition and chemical state. In addition, the interpretation of structural characteristics extracted from X-ray spectroscopy methods will be further hindered when wide nanoparticle size and shape distributions are available in the as prepared samples.^{115,134} This is even more relevant when *operando* catalysis studies are undertaken, since in that case the coexistence of particles of different size and shape evolving under reaction conditions is common. Therefore, the interpretation of structural information extracted from XAS and NRIXS in terms of 3D structural motifs for inhomogeneous systems should be carried out with extreme care, and must

rely on complementary insight from additional techniques such as microscopy methods and theoretical modelling.

In the present study, we combined AFM, TEM, XPS, NRIXS and XAS to gain insight into the evolution of the structure and composition of homogeneously dispersed size and shape-controlled FeCu and FeAg NPs during CO₂RR. We remark here that for the FeAg NPs, the EDX line profiles acquired after reaction (figure 41) extend further outwards as compared to the Fe profiles, which suggests some degree of Ag segregation to the surface. For the FeCu NPs, the line profiles indicate more even mixing of the two elements. These STEM-EDX results are however limited because of the difficulty of obtaining high quality and contaminant-free images in the presence of the Nafion NP binder and carbon support, which strongly interacts with the electron beam, resulting in the need of employing short acquisition times. Nevertheless, the microscopy data are consistent with the X-ray spectroscopy and selectivity data regarding the segregation behavior in the FeCu and FeAg NPs.

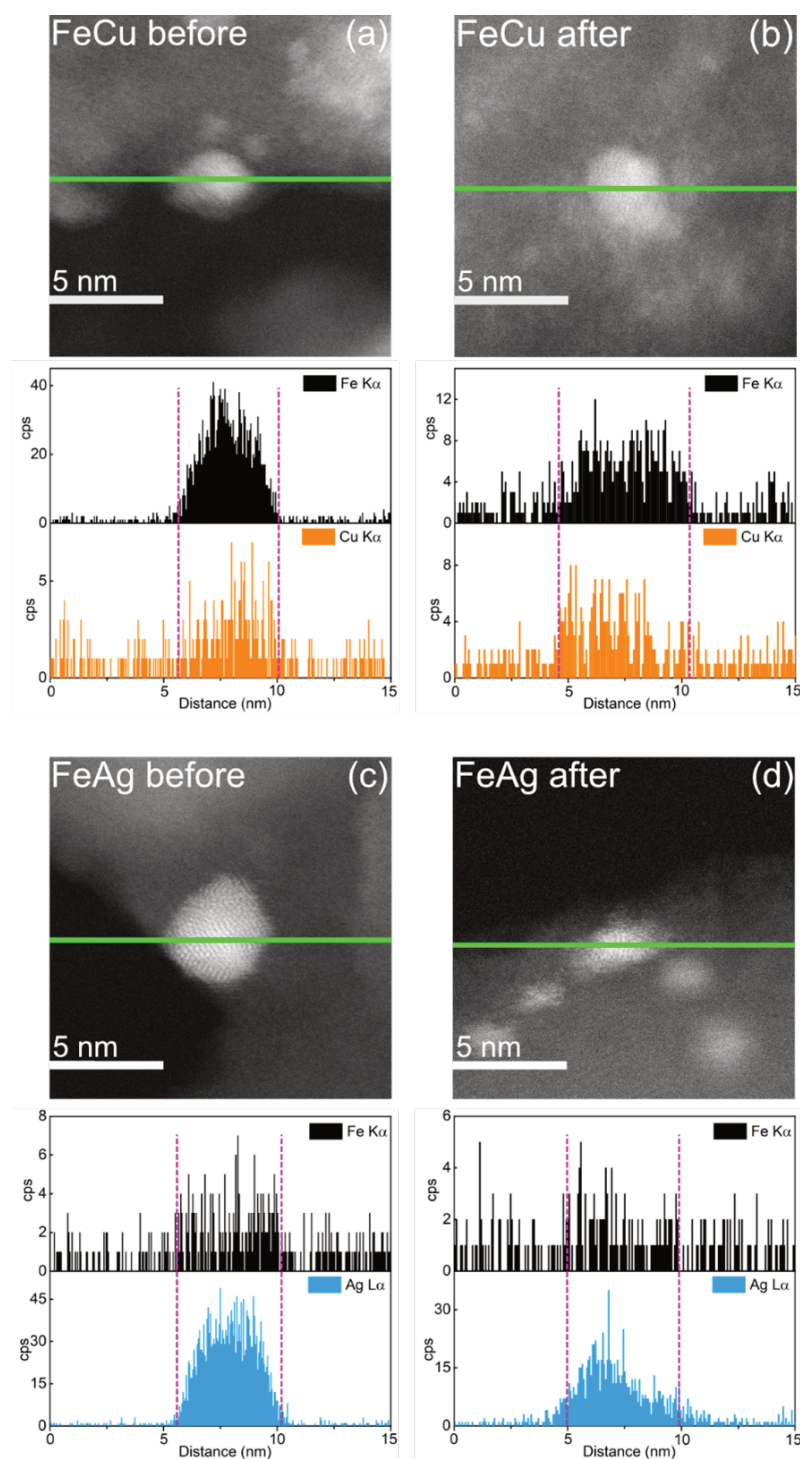


Figure 41: STEM images and EDX line cans (green horizontal lines) of micellar FeCu and FeAg NPs supported on nanocrystalline SiO₂ (a and c) and on carbon powder (b and d). Images (a) and (c) were obtained before the reaction and (b) and (d) after CO₂RR. Violet lines are reference lines to guide the eye.

According to the respective surface energies and atomic sizes, the formation of an either Cu or Ag shell and a bcc-Fe core is expected.^{98,135,136} For instance, we have previously shown the segregation of copper to the surface of CuNi NPs under reducing conditions ($\text{CO}_2 + \text{CO} + \text{H}_2$).¹³⁷ This is in good agreement with the electrochemical behavior observed here for the FeAg NPs, which was found to be reminiscent of pure silver. The trend was not as clear for the FeCu sample, where size effects already demonstrated for pure Cu NPs will also lead to an increase of the H_2 production with decreasing NP size at the expense of CO and hydrocarbons. Therefore, for the Fe-Cu system, we cannot discard the possibility of having Cu-rich and Fe-rich regions coexisting at the NP surface, which would also explain the increased H_2 production (taking place over the exposed Fe component) as compared to the selectivity obtained in similarly sized monometallic Cu NPs.

Although the present nanosized catalysts do not display an outstanding activity or selectivity for CO_2RR , in line with previous studies for small NPs which also favor H_2 -evolution,^{36–38} this study serves to provide fundamental insight into the dynamic behavior of electrocatalysts under reaction conditions. Furthermore, it illustrates a powerful combination of X-ray based synchrotron techniques for the characterization of the structural and chemical evolution of electrocatalysts that, when available hand in hand with reactivity data, allows one to gain in depth understanding of the structural motifs and chemical compositions responsible for specific selectivity trends.

Table 3: Coordination numbers (CN) and interatomic distances (R), derived from the fit of EXAFS data of samples $^{57}\text{FeCu}$ and $^{57}\text{FeAg}$ at the Fe, Cu and Ag K-edges. The data were measured in air (as-is) and *operando* during CO_2RR at -1.1 V vs RHE in 0.1 M KHCO_3 after 1.5 h to 3.5 h . The uncertainty of the last digit is given in parentheses. Additional parameters and fit results are shown in the appendix in tables 6 and 7. A single Fe-Fe scattering path was used to fit the overlapping contributions from the first two coordination shells in bcc Fe due to the limited resolution in R-space as a result of the short Fe K-edge spectrum.

Sample	Treatment	CN	R(Å)	CN	R(Å)	CN	R(Å)	CN	R(Å)
$^{57}\text{FeCu}$		Cu-O		Cu-Cu		Fe-O		Fe-Fe	
	As is	2.3(3)	1.95(1)			6.9(2.1)	1.81(6)		
	Operando	0.7(6)	1.95(3)	4.2(1.2)	2.56(1)	2.3(1.2)	1.81(4)	1.5(0.9)	2.48(5)
		Ag-Cl		Ag-Ag		Fe-O		Fe-Fe	
$^{57}\text{FeAg}$	As is	4.6(6)	2.81(1)			6.7(1.6)	1.81(2)		
	Operando			5.4(7)	2.941(1)	2 (1)	1.81(4)	1(1)	2.48(6)
Bulk	Cu foil ¹³⁸			12	2.566				
	CuO ¹³⁹	4	1.95(1)						
	Ag foil ¹⁴⁰			12	2.883(7)				
	AgCl ¹⁴¹	6	2.79(1)						
	FeO(OH) ¹³¹					6	2.00		
	Fe foil ¹³³							8+6	2.47(1)

5.4 Summary

This study demonstrates the dynamic transformations undergone by FeCu and FeAg NPs during the electrochemical reduction of CO_2 . In particular, *operando* NRIXS and XAFS data revealed the formation of an Ag shell surrounding a bcc-Fe core. On the other hand, more intermixing was observed for the FeCu NPs, and the presence of separated Fe and Cu regions on the NP surface under reaction conditions could not be excluded. Interestingly, a similar CO production was observed for the thin Ag-shell in the FeAg NPs as compared to pure Ag NPs, which indicates the optimization of the use of the noble metal. Overall, and due to the small NP size, the production of H_2 was, however, favored, especially in the Fe and FeCu samples. Finally, this work emphasizes that *operando* experiments

are a very valuable tool to link catalytic properties to structure and composition of electrocatalysts under realistic working conditions.

6 Conclusion and Outlook

Here we have explored the structure and composition of copper single crystals and bimetallic nanoparticles in the context of energy conversion. The scope of the research projects gradually expanded: From UHV studies of copper surface preparations on an atomic scale, to quasi ideal Cu(100) electrodes subjected to electrochemical experiments under exclusion of air, and lastly to bimetallic nanoparticle ensembles under reaction conditions. We were interested in the characterisation of structure and composition of our materials under changing, but controlled conditions.

First, it was shown here that a low-pressure oxygen plasma treatment of Cu(100) and Cu(111) surfaces at RT results in the growth of three-dimensional copper oxide islands, surrounded by O-induced Cu₂O surface reconstructions. The composition of the surface oxides in the islands was determined by XPS and NEXAFS, and we traced the time dependent evolution of the constituting Cu₂O and CuO species. On both surface orientations, prolonged exposure to the plasma leads to coalescing islands and eventually a closed oxide thin film. Interestingly, we found significant differences in the evolution of the islands and oxides formation; on Cu(100), we found initially fewer islands of lower height than on Cu(111), and in addition only Cu₂O was found until later stages of plasma exposure. On Cu(111) on the other hand, Cu₂O and CuO grew simultaneously. At the mild conditions here at low pressure and room temperature, the formation of CuO is a clear difference to the otherwise necessary high temperatures required. In that sense, we have proven in our study that using an O₂-plasma treatment makes both oxide species accessible in a confined volume close to the surface. Future projects related to plasma oxidation may utilize the insights we gained here to precisely fabricate surface oxides of a

defined composition, and we anticipate uses of this approach for key fields in energy conversion and corrosion.

In the second project, we explored the morphology of pristine Cu(100) surfaces when subjected to pulsed potential treatments in KHCO_3 without air contact to the sample prior to the electrochemical experiment. We found dramatic surface transformations in certain potential windows, and correlation to the duration of the anodic and cathodic pulses. Large, cubic structures were formed when the potential was switched between 0.6 V (0.8 V) and -1 V vs. RHE for 1 s each, over a duration of 1 h. Interestingly we also found that the subsequent, 1h long electrolysis at -1V (corresponding to CO_2RR conditions) results in flattening of the cubic structures and a few nm tall granular structures on the surface. This granular structure was indeed also found when the surface was treated at the same potentiostatic conditions but without prior pulse treatment, indicating that the potentiostatic conditions lead to the same surface over time. These results allow us to make more accurate conclusions regarding when the effects of surface morphology need to be distinguished from other effects, such as oxidation state. With the identification of potential windows and the corresponding morphology changes, the increased surface area and roughness can be accounted for in order to not lead to misleading conclusions.

Lastly, we expanded the scope of our investigated systems to a nanoparticle ensemble under reaction conditions. We used NRIXS and XAFS measurements to gain insight into the structure and surface composition of FeCu and FeAg nanoparticles during the CO_2RR and to extract correlations with their catalytic performance. The formation of a core-shell structure during CO_2RR in the case of FeAg NPs was inferred from the analysis of the operando NRIXS data and XAFS measurements. Electrochemical analysis of the FeAg NPs revealed a faradaic selectivity of 36% for CO in 0.1 M KHCO_3 at -1.1 V vs RHE, similar to that of pure Ag NPs. In contrast, a predominant selectivity towards H_2 evolution is obtained in the case of the FeCu NPs, analogous to the results for pure Fe NPs. While the catalytic performance is not particularly competitive for practical applications, we showed a viable indirect approach to structure determination

of a complex system even under reaction conditions via spectroelectrochemical NRXS. In principle, this approach can be used for other reactions and materials with Mössbauer-active isotopes.

7 Bibliography

- ¹I. Adopted, “Climate change 2014 synthesis report”, IPCC: Geneva, Switzerland (2014).
- ²T. R. Anderson, E. Hawkins, and P. D. Jones, “Co₂, the greenhouse effect and global warming: from the pioneering work of arrhenius and callendar to today’s earth system models”, *Endeavour* **40**, 178–187 (2016).
- ³R. Coma, M. Ribes, E. Serrano, E. Jiménez, J. Salat, and J. Pascual, “Global warming-enhanced stratification and mass mortality events in the mediterranean”, *Proceedings of the National Academy of Sciences* **106**, 6176–6181 (2009).
- ⁴R. L. Peters, “Effects of global warming on forests”, *Forest Ecology and Management* **35**, 13–33 (1990).
- ⁵S. Alfonso, M. Gesto, and B. Sadoul, “Temperature increase and its effects on fish stress physiology in the context of global warming”, *Journal of Fish Biology* (2020).
- ⁶T. K. Matthews, R. L. Wilby, and C. Murphy, “Communicating the deadly consequences of global warming for human heat stress”, *Proceedings of the National Academy of Sciences* **114**, 3861–3866 (2017).
- ⁷K. S. Lackner, “A guide to co₂ sequestration”, *Science* **300**, 1677–1678 (2003).
- ⁸A. Yamasaki, “An overview of co₂ mitigation options for global warming—emphasizing co₂ sequestration options”, *Journal of chemical engineering of Japan* **36**, 361–375 (2003).
- ⁹W. J. J. Huijgen and R. N. J. Comans, “Carbon dioxide sequestration by mineral carbonation. literature review”, (2003).

- ¹⁰K. R. Hein, "Future energy supply in europe—challenge and chances", *Fuel* **84**, 1189–1194 (2005).
- ¹¹J. Twidell and T. Weir, *Renewable energy resources* (Routledge, 2015).
- ¹²O. Ellabban, H. Abu-Rub, and F. Blaabjerg, "Renewable energy resources: current status, future prospects and their enabling technology", *Renewable and Sustainable Energy Reviews* **39**, 748–764 (2014).
- ¹³K. Chapman, "The international petrochemical industry", (1991).
- ¹⁴V. B. Samuel, P. Agamuthu, and M. Hashim, "Indicators for assessment of sustainable production: a case study of the petrochemical industry in malaysia", *Ecological Indicators* **24**, 392–402 (2013).
- ¹⁵M. T. Ravanchi and S. Sahebdehfar, "Carbon dioxide capture and utilization in petrochemical industry: potentials and challenges", *Applied Petrochemical Research* **4**, 63–77 (2014).
- ¹⁶G. Singhal, G. Renger, S. Sopory, K. Irrgang, et al., *Concepts in photobiology: photosynthesis and photomorphogenesis* (Springer Science & Business Media, 2012).
- ¹⁷D. Pletcher, "The cathodic reduction of carbon dioxide—what can it realistically achieve? a mini review", *Electrochemistry Communications* **61**, 97–101 (2015).
- ¹⁸G. W. Crabtree, M. S. Dresselhaus, and M. V. Buchanan, "The hydrogen economy", *Physics today* **57**, 39–44 (2004).
- ¹⁹V. A. Medvedev, J. Cox, and D. D. Wagman, *Codata key values for thermodynamics* (Hemisphere Publishing Corporation New York, 1989).
- ²⁰M. Binnewies and E. Milke, *Thermochemical data of elements and compounds* (Wiley-VCH, 1999).
- ²¹P. Sabatier and J. Senderens, "Comptes rendus des séances de l'académie des sciences, section vi-chimie", Paris: Imprimerie Gauthier-Villars (1902).
- ²²F. Fischer and H. Tropsch, "Über die direkte synthese von erdöl-kohlenwasserstoffen bei gewöhnlichem druck. (erste mitteilung)", *Berichte der deutschen chemischen Gesellschaft (A and B Series)* **59**, 830–831 (1926).

- ²³T. Lin, K. Gong, C. Wang, Y. An, X. Wang, X. Qi, S. Li, Y. Lu, L. Zhong, and Y. Sun, "Fischer-tropsch synthesis to olefins: catalytic performance and structure evolution of Co_2C -based catalysts under a CO_2 environment", *ACS Catalysis* **9**, 9554–9567 (2019).
- ²⁴Y. Hori, K. Kikuchi, and S. Suzuki, "Production of CO and CH_4 in electrochemical reduction of CO_2 at metal electrodes in aqueous hydrogencarbonate solution", *Chemistry Letters* **14**, 1695–1698 (1985).
- ²⁵Y. Hori, H. Wakebe, T. Tsukamoto, and O. Koga, "Electrocatalytic process of CO selectivity in electrochemical reduction of CO_2 at metal electrodes in aqueous media", *Electrochimica Acta* **39**, 1833–1839 (1994).
- ²⁶J. Masa, C. Andronescu, and W. Schuhmann, "Electrocatalysis as the nexus for sustainable renewable energy: the gordian knot of activity, stability, and selectivity", *Angewandte Chemie International Edition* **59**, 15298–15312 (2020).
- ²⁷S. Nitopi, E. Bertheussen, S. B. Scott, X. Liu, A. K. Engstfeld, S. Horch, B. Seger, I. E. Stephens, K. Chan, C. Hahn, et al., "Progress and perspectives of electrochemical CO_2 reduction on copper in aqueous electrolyte", *Chemical reviews* **119**, 7610–7672 (2019).
- ²⁸R. P. Janssonius, L. M. Reid, C. N. Virca, and C. P. Berlinguette, "Strain engineering electrocatalysts for selective CO_2 reduction", *ACS Energy Letters* **4**, 980–986 (2019).
- ²⁹H. Liu, J. Liu, and B. Yang, "Computational insights into the strain effect on the electrocatalytic reduction of CO_2 to CO on Pd surfaces", *Physical Chemistry Chemical Physics* **22**, 9600–9606 (2020).
- ³⁰C. Kim, F. Dionigi, V. Beermann, X. Wang, T. Möller, and P. Strasser, "Alloy nanocatalysts for the electrochemical oxygen reduction (orr) and the direct electrochemical carbon dioxide reduction reaction (CO_2RR)", *Advanced Materials* **31**, 1805617 (2019).
- ³¹K. Liu, M. Ma, L. Wu, M. Valenti, D. Cardenas-Morcoso, J. P. Hofmann, J. Bisquert, S. Gimenez, and W. A. Smith, "Electronic effects determine the selectivity of planar Au-Cu bimetallic thin films for electrochemical CO_2 reduction", *ACS applied materials & interfaces* **11**, 16546–16555 (2019).

- ³²J. Frese, *Electrochemical reduction of CO₂ at solid electrodes* (Elsevier: Amsterdam, 1993).
- ³³J. Christophe, T. Doneux, and C. Buess-Herman, "Electroreduction of carbon dioxide on copper-based electrodes: activity of copper single crystals and copper–gold alloys", *Electrocatalysis* **3**, 139–146 (2012).
- ³⁴Y. Hori, I. Takahashi, O. Koga, and N. Hoshi, "Electrochemical reduction of carbon dioxide at various series of copper single crystal electrodes", *Journal of Molecular Catalysis A: Chemical* **199**, 39–47 (2003).
- ³⁵C. Schlaup and S. Horch, "In-situ STM study of phosphate adsorption on Cu (111), Au (111) and Cu/Au (111) electrodes", *Surface Science* **608**, 44–54 (2013).
- ³⁶R. Reske, H. Mistry, F. Behafarid, B. R. Cuenya, and P. Strasser, "Particle Size Effects in the Catalytic Electroreduction of CO₂ on Cu Nanoparticles", *Journal of the American Chemical Society* **136**, 6978–6986 (2014).
- ³⁷H. Mistry, R. Reske, Z. Zeng, Z.-J. Zhao, J. Greeley, P. Strasser, and B. R. Cuenya, "Exceptional Size-Dependent Activity Enhancement in the Electroreduction of CO₂ over Au Nanoparticles", *Journal of the American Chemical Society* **136**, 16473–16476 (2014).
- ³⁸H. S. Jeon, I. Sinev, F. Scholten, N. J. Divins, I. Zegkinoglou, L. Pielsticker, and B. R. Cuenya, "Operando Evolution of the Structure and Oxidation State of Size-Controlled Zn Nanoparticles during CO₂ Electroreduction", *Journal of the American Chemical Society* **140**, 9383–9386 (2018).
- ³⁹I. Takahashi, O. Koga, N. Hoshi, and Y. Hori, "Electrochemical reduction of CO₂ at copper single crystal Cu (s)-[n(111)×(111)] and Cu (s)-[n(110)×(100)] electrodes", *Journal of Electroanalytical Chemistry* **533**, 135–143 (2002).
- ⁴⁰A. K. Engstfeld, T. Maagaard, S. Horch, I. Chorkendorff, and I. E. Stephens, "Polycrystalline and single-crystal Cu electrodes: influence of experimental conditions on the electrochemical properties in alkaline media", *Chem.-Eur. J* **24**, 17743–17755 (2018).
- ⁴¹G. Binnig and H. Rohrer, "Scanning tunneling microscopy", *Surface Science* **126**, 236–244 (1983).

- ⁴²E. Meyer, H. J. Hug, and R. Bennewitz, *Scanning probe microscopy: the lab on a tip* (Springer Science & Business Media, 2003).
- ⁴³S. Morita, F. J. Giessibl, E. Meyer, and R. Wiesendanger, *Noncontact atomic force microscopy: volume 3* (Springer, 2015).
- ⁴⁴P. Eaton and P. West, *Atomic force microscopy* (Oxford university press, 2010).
- ⁴⁵P. Van der Heide, "X-ray photoelectron spectroscopy", *An Introduction to Principles and Practices* (2011).
- ⁴⁶I. Chorkendorff and J. W. Niemantsverdriet, *Concepts of modern catalysis and kinetics* (John Wiley & Sons, 2017).
- ⁴⁷J. W. Niemantsverdriet, *Spectroscopy in catalysis* (Wiley Online Library, 2007).
- ⁴⁸U. Bergmann, W. Sturhahn, D. E. Linn, F. E. Jenney, M. W. W. Adams, K. Rupnik, B. J. Hales, E. E. Alp, A. Mayse, and S. P. Cramer, "Observation of Fe-H/D Modes by Nuclear Resonant Vibrational Spectroscopy", *Journal of the American Chemical Society* **125**, 4016–4017 (2003).
- ⁴⁹M. Y. Hu, T. S. Toellner, N. Dauphas, E. E. Alp, and J. Zhao, "Moments in nuclear resonant inelastic x-ray scattering and their applications", *Physical Review B* **87**, 064301 (2013).
- ⁵⁰W. Sturhahn, "Nuclear resonant spectroscopy", *Journal of Physics: Condensed Matter* **16**, S497 (2004).
- ⁵¹M. Y. Hu, W. Sturhahn, T. S. Toellner, P. D. Mannheim, D. E. Brown, J. Zhao, and E. E. Alp, "Measuring velocity of sound with nuclear resonant inelastic x-ray scattering", *Physical Review B* **67**, 094304 (2003).
- ⁵²S. Kelly, "Basics of exafs data analysis", Electronic resource (2009).
- ⁵³G. Vlaica and L. Olivi, "Exafs spectroscopy: a brief introduction", *Croatica chemica acta* **77**, 427–433 (2004).
- ⁵⁴F. Jona, J. Strozier Jr, and W. Yang, "Low-energy electron diffraction for surface structure analysis", *Reports on Progress in Physics* **45**, 527 (1982).
- ⁵⁵A. Mittiga, E. Salza, F. Sarto, M. Tucci, and R. Vasanthi, "Heterojunction solar cell with 2% efficiency based on a cu2o substrate", *Applied Physics Letters* **88**, 163502 (2006).

- ⁵⁶L. Olsen, F. Addis, and W. Miller, "Experimental and theoretical studies of cu₂o solar cells", *Solar cells* **7**, 247–279 (1982).
- ⁵⁷N. L. Reddy, S. Emin, V. D. Kumari, and S. Muthukonda Venkatakrishnan, "Cu₂O quantum dots decorated tio₂ nanocomposite photocatalyst for stable hydrogen generation", *Industrial & Engineering Chemistry Research* **57**, 568–577 (2018).
- ⁵⁸Y. Zhang, B. Deng, T. Zhang, D. Gao, and A.-W. Xu, "Shape effects of cu₂o polyhedral microcrystals on photocatalytic activity", *The Journal of Physical Chemistry C* **114**, 5073–5079 (2010).
- ⁵⁹M. Ma, K. Djanashvili, and W. A. Smith, "Selective electrochemical reduction of co₂ to co on cuo-derived cu nanowires", *Physical Chemistry Chemical Physics* **17**, 20861–20867 (2015).
- ⁶⁰C. W. Li, J. Ciston, and M. W. Kanan, "Electroreduction of carbon monoxide to liquid fuel on oxide-derived nanocrystalline copper", *Nature* **508**, 504–507 (2014).
- ⁶¹M. Löffler, P. Khanipour, N. Kulyk, K. J. Mayrhofer, and I. Katsounaros, "Insights into liquid product formation during carbon dioxide reduction on copper and oxide-derived copper from quantitative real-time measurements", *ACS catalysis* **10**, 6735–6740 (2020).
- ⁶²H. Mistry, A. S. Varela, C. S. Bonifacio, I. Zegkinoglou, I. Sinev, Y.-W. Choi, K. Kisslinger, E. A. Stach, J. C. Yang, P. Strasser, et al., "Highly selective plasma-activated copper catalysts for carbon dioxide reduction to ethylene", *Nature communications* **7**, 1–9 (2016).
- ⁶³F. Scholten, I. Sinev, M. Bernal, and B. Roldan Cuenya, "Plasma-modified dendritic cu catalyst for co₂ electroreduction", *ACS catalysis* **9**, 5496–5502 (2019).
- ⁶⁴R. M. Aran-Ais, F. Scholten, S. Kunze, R. Rizo, and B. Roldan Cuenya, "The role of in situ generated morphological motifs and cu (i) species in c₂+ product selectivity during co₂ pulsed electroreduction", *Nature Energy* **5**, 317–325 (2020).

- ⁶⁵F. Dattila, R. García-Muelas, and N. López, "Active and selective ensembles in oxide-derived copper catalysts for CO₂ reduction", *ACS Energy Letters* **5**, 3176–3184 (2020).
- ⁶⁶S.-C. Lin, C.-C. Chang, S.-Y. Chiu, H.-T. Pai, T.-Y. Liao, C.-S. Hsu, W.-H. Chiang, M.-K. Tsai, and H. M. Chen, "Operando time-resolved x-ray absorption spectroscopy reveals the chemical nature enabling highly selective CO₂ reduction", *Nature communications* **11**, 1–12 (2020).
- ⁶⁷C. Gattinoni and A. Michaelides, "Atomistic details of oxide surfaces and surface oxidation: the example of copper and its oxides", *Surface Science Reports* **70**, 424–447 (2015).
- ⁶⁸K. Lahtonen, M. Hirsimäki, M. Lampimäki, and M. Valden, "Oxygen adsorption-induced nanostructures and island formation on Cu(100): bridging the gap between the formation of surface confined oxygen chemisorption layer and oxide formation", *The Journal of chemical physics* **129**, 124703 (2008).
- ⁶⁹M. Lampimäki, K. Lahtonen, M. Hirsimäki, and M. Valden, "Nanoscale oxidation of Cu (100): oxide morphology and surface reactivity", *The Journal of chemical physics* **126**, 034703 (2007).
- ⁷⁰M. Z. Baykara, M. Todorović, H. Mönig, T. C. Schwendemann, Ö. Ünverdi, L. Rodrigo, E. I. Altman, R. Pérez, and U. D. Schwarz, "Atom-specific forces and defect identification on surface-oxidized Cu (100) with combined 3d-AFM and STM measurements", *Physical Review B* **87**, 155414 (2013).
- ⁷¹L. Dubois, "Oxygen chemisorption and cuprous oxide formation on Cu (111): a high resolution EELS study", *Surface Science* **119**, 399–410 (1982).
- ⁷²A. Soon, M. Todorova, B. Delley, and C. Stampfl, "Oxygen adsorption and stability of surface oxides on Cu (111): a first-principles investigation", *Physical Review B* **73**, 165424 (2006).
- ⁷³F. Wiame, V. Maurice, and P. Marcus, "Initial stages of oxidation of Cu (111)", *Surface science* **601**, 1193–1204 (2007).

- ⁷⁴J. J. Navarro, S. Tosoni, J. P. Bruce, L. Chaves, M. Heyde, G. Pacchioni, and B. Roldan Cuenya, "Structure of a silica thin film on oxidized cu (111): conservation of the honeycomb lattice and role of the interlayer", *The Journal of Physical Chemistry C* **124**, 20942–20949 (2020).
- ⁷⁵F. Jensen, F. Besenbacher, E. Laegsgaard, and I. Stensgaard, "Oxidation of cu (111): two new oxygen induced reconstructions", *Surface Science Letters* **259**, L774–L780 (1991).
- ⁷⁶C. Zheng, J. Cao, Y. Zhang, and H. Zhao, "Insight into the oxidation mechanism of a cu-based oxygen carrier (cu → cu₂O → cuO) in chemical looping combustion", *Energy & Fuels* **34**, 8718–8725 (2020).
- ⁷⁷K. Fujita, D. Ando, M. Uchikoshi, K. Mimura, and M. Isshiki, "New model for low-temperature oxidation of copper single crystal", *Applied surface science* **276**, 347–358 (2013).
- ⁷⁸A. Stadnichenko, A. Sorokin, and A. Boronin, "Xps, ups, and stm studies of nanostructured cuo films", *Journal of Structural Chemistry* **49**, 341–347 (2008).
- ⁷⁹T. Schmidt, H. Marchetto, P. L. Lévesque, U. Groh, F. Maier, D. Preikszas, P. Hartel, R. Spehr, G. Lilienkamp, W. Engel, et al., "Double aberration correction in a low-energy electron microscope", *Ultramicroscopy* **110**, 1358–1361 (2010).
- ⁸⁰T. Schmidt, A. Sala, H. Marchetto, E. Umbach, and H.-J. Freund, "First experimental proof for aberration correction in xpeem: resolution, transmission enhancement, and limitation by space charge effects", *Ultramicroscopy* **126**, 23–32 (2013).
- ⁸¹D. Nečas and P. Klapetek, "Gwyddion: an open-source software for SPM data analysis", *Open Physics* **10**, 181–188 (2012).
- ⁸²I. Horcas, R. Fernández, J. Gomez-Rodriguez, J. Colchero, J. Gómez-Herrero, and A. Baro, "Wsxm: a software for scanning probe microscopy and a tool for nanotechnology", *Review of scientific instruments* **78**, 013705 (2007).
- ⁸³F. Jensen, F. Besenbacher, E. Laegsgaard, and I. Stensgaard, "Dynamics of oxygen-induced reconstruction of cu (100) studied by scanning tunneling microscopy", *Physical Review B* **42**, 9206 (1990).

- ⁸⁴H. Mönig, M. Todorovic, M. Z. Baykara, T. C. Schwendemann, L. Rodrigo, E. I. Altman, R. Perez, and U. D. Schwarz, "Understanding scanning tunneling microscopy contrast mechanisms on metal oxides: a case study", *ACS nano* **7**, 10233–10244 (2013).
- ⁸⁵T. T. Ly, T. Lee, S. Kim, Y.-J. Lee, G. Duvjir, K. Jang, K. Palotás, S.-Y. Jeong, A. Soon, and J. Kim, "Growing ultrathin Cu_2O films on highly crystalline Cu (111): a closer inspection from microscopy and theory", *The Journal of Physical Chemistry C* **123**, 12716–12721 (2019).
- ⁸⁶A. Önsten, M. Göthelid, and U. O. Karlsson, "Atomic structure of Cu_2O (111)", *Surface Science* **603**, 257–264 (2009).
- ⁸⁷R. Zhang, L. Li, L. Frazer, K. B. Chang, K. R. Poepelmeier, M. K. Chan, and J. R. Guest, "Atomistic determination of the surface structure of Cu_2O (111): experiment and theory", *Physical Chemistry Chemical Physics* **20**, 27456–27463 (2018).
- ⁸⁸T. Matsumoto, R. a. A. Bennett, P. Stone, T. Yamada, K. Domen, and M. Bowker, "Scanning tunneling microscopy studies of oxygen adsorption on Cu (111)", *Surface science* **471**, 225–245 (2001).
- ⁸⁹E. Bauer, "Low energy electron microscopy", *Reports on Progress in Physics* **57**, 895 (1994).
- ⁹⁰T. Fujita, Y. Okawa, Y. Matsumoto, and K.-i. Tanaka, "Phase boundaries of nanometer scale $\text{c}(2\times 2)\text{-O}$ domains on the Cu (100) surface", *Physical Review B* **54**, 2167 (1996).
- ⁹¹X. Lian, P. Xiao, S.-C. Yang, R. Liu, and G. Henkelman, "Calculations of oxide formation on low-index Cu surfaces", *The Journal of chemical physics* **145**, 044711 (2016).
- ⁹²C. Devlin, Y. Sato, and S. Chiang, "Morphology of the Cu_2O surface oxide phase formed on Cu (100) at high temperature", *Journal of Applied Physics* **105**, 123534 (2009).
- ⁹³M. Henzler, "Leed studies of surface imperfections", *Applications of Surface Science* **11**, 450–469 (1982).

- ⁹⁴M. Wuttig, R. Franchy, and H. Ibach, "Structural models for the cu (100)(2 × $\sqrt{2}$) r45-o phase", *Surface Science* **224**, L979–L982 (1989).
- ⁹⁵M. Wuttig, R. Franchy, and H. Ibach, "Oxygen on cu (100)-a case of an adsorbate induced reconstruction", *Surface Science* **213**, 103–136 (1989).
- ⁹⁶R. Judd, P. Hollins, and J. Pritchard, "The interaction of oxygen with cu (111): adsorption, incorporation and reconstruction", *Surface science* **171**, 643–653 (1986).
- ⁹⁷K. H. Schulz and D. F. Cox, "Photoemission and low-energy-electron-diffraction study of clean and oxygen-dosed cu₂O (111) and (100) surfaces", *Physical Review B* **43**, 1610 (1991).
- ⁹⁸H. L. Skriver and N. M. Rosengaard, "Surface energy and work function of elemental metals", *Physical Review B* **46**, 7157–7168 (1992).
- ⁹⁹K. Moritani, M. Okada, Y. Teraoka, A. Yoshigoe, and T. Kasai, "Reconstruction of cu (111) induced by a hyperthermal oxygen molecular beam", *The Journal of Physical Chemistry C* **112**, 8662–8667 (2008).
- ¹⁰⁰A. Gloystein and N. Nilius, "Copper oxidation on pt (111)-more than a surface oxide?", *The Journal of Physical Chemistry C* **123**, 26939–26946 (2019).
- ¹⁰¹M. Greiner, T. Jones, B. Johnson, T. Rocha, Z.-J. Wang, M. Armbrüster, M. Willinger, A. Knop-Gericke, and R. Schlögl, "The oxidation of copper catalysts during ethylene epoxidation", *Physical Chemistry Chemical Physics* **17**, 25073–25089 (2015).
- ¹⁰²K. Schweinar, S. Beeg, C. Hartwig, C. R. Rajamathi, O. Kasian, S. Piccinin, M. J. Prieto, L. C. Tanase, D. M. Gottlob, T. Schmidt, et al., "Formation of a 2d meta-stable oxide by differential oxidation of agcu alloys", *ACS applied materials & interfaces* **12**, 23595–23605 (2020).
- ¹⁰³F. Cavalca, R. Ferragut, S. Aghion, A. Eilert, O. Diaz-Morales, C. Liu, A. L. Koh, T. W. Hansen, L. G. Pettersson, and A. Nilsson, "Nature and distribution of stable subsurface oxygen in copper electrodes during electrochemical CO₂ reduction", *The Journal of Physical Chemistry C* **121**, 25003–25009 (2017).

- ¹⁰⁴A. Eilert, F. Cavalca, F. S. Roberts, J. Osterwalder, C. Liu, M. Favaro, E. J. Crumlin, H. Ogasawara, D. Friebe, L. G. Pettersson, et al., "Subsurface oxygen in oxide-derived copper electrocatalysts for carbon dioxide reduction", *The journal of physical chemistry letters* **8**, 285–290 (2017).
- ¹⁰⁵A. J. Garza, A. T. Bell, and M. Head-Gordon, "Is subsurface oxygen necessary for the electrochemical reduction of CO₂ on copper?", *The journal of physical chemistry letters* **9**, 601–606 (2018).
- ¹⁰⁶G. H. Simon, C. S. Kley, and B. Roldan Cuenya, "Potential-dependent morphology of copper catalysts during CO₂ electroreduction revealed by in situ atomic force microscopy", *Angewandte Chemie International Edition* (2020).
- ¹⁰⁷P. Grosse, D. Gao, F. Scholten, I. Sinev, H. Mistry, and B. Roldan Cuenya, "Dynamic changes in the structure, chemical state and catalytic selectivity of Cu nanocubes during CO₂ electroreduction: size and support effects", *Angewandte Chemie International Edition* **57**, 6192–6197 (2018).
- ¹⁰⁸P. Grosse, A. Yoon, C. Rettenmaier, S. W. Chee, and B. R. Cuenya, "Growth dynamics and processes governing the stability of electrodeposited size-controlled cubic Cu catalysts", *The Journal of Physical Chemistry C* **124**, 26908–26915 (2020).
- ¹⁰⁹S. Kunze, P. Grosse, M. Bernal Lopez, I. Sinev, I. Zegkinoglou, H. Mistry, J. Timoshenko, M. Y. Hu, J. Zhao, E. E. Alp, et al., "Operando nrxs and xafs investigation of segregation phenomena in Fe-Cu and Fe-Ag nanoparticle catalysts during CO₂ electroreduction", *Angewandte Chemie* **132**, 22856–22863 (2020).
- ¹¹⁰M. A. Bañares, "Operando methodology: combination of in situ spectroscopy and simultaneous activity measurements under catalytic reaction conditions", *Catalysis Today* **100**, 71–77 (2005).
- ¹¹¹H. Topsøe, "Developments in operando studies and in situ characterization of heterogeneous catalysts", *Journal of Catalysis* **216**, 155–164 (2003).
- ¹¹²B. M. Weckhuysen, "Determining the active site in a catalytic process: Operando spectroscopy is more than a buzzword", *Physical Chemistry Chemical Physics* **5**, 4351 (2003).

- ¹¹³K. J. J. Mayrhofer, V. Juhart, K. Hartl, M. Hanzlik, and M. Arenz, "Adsorbate-induced surface segregation for core-shell nanocatalysts.", *Angewandte Chemie (International ed. in English)* **48**, 3529–31 (2009).
- ¹¹⁴Y.-W. Choi, H. Mistry, and B. R. Cuenya, "New insights into working nanostructured electrocatalysts through operando spectroscopy and microscopy", *Current Opinion in Electrochemistry* **1**, 95–103 (2017).
- ¹¹⁵A. I. Frenkel, J. A. Rodriguez, and J. G. Chen, "Synchrotron Techniques for In Situ Catalytic Studies: Capabilities, Challenges, and Opportunities", *ACS Catalysis* **2**, 2269–2280 (2012).
- ¹¹⁶W. Sturhahn, T. S. Toellner, E. E. Alp, X. Zhang, M. Ando, Y. Yoda, S. Kikuta, M. Seto, C. W. Kimball, and B. Dabrowski, "Phonon Density of States Measured by Inelastic Nuclear Resonant Scattering", *Physical Review Letters* **74**, 3832–3835 (1995).
- ¹¹⁷B. R. Cuenya, L. K. Ono, J. R. Croy, K. Paredis, A. Kara, H. Heinrich, J. Zhao, E. E. Alp, A. T. DelaRiva, A. Datye, E. A. Stach, and W. Keune, "Size-dependent evolution of the atomic vibrational density of states and thermodynamic properties of isolated Fe nanoparticles", *Physical Review B* **86**, 165406 (2012).
- ¹¹⁸B. R. Cuenya, W. Keune, R. Peters, E. Schuster, B. Sahoo, U. v. Hörsten, W. Sturhahn, J. Zhao, T. S. Toellner, E. E. Alp, and S. D. Bader, "High-energy phonon confinement in nanoscale metallic multilayers", *Physical Review B* **77**, 165410 (2008).
- ¹¹⁹B. Fultz, C. C. Ahn, E. E. Alp, W. Sturhahn, and T. S. Toellner, "Phonons in Nanocrystalline 57Fe", *Physical Review Letters* **79**, 937–940 (1997).
- ¹²⁰W. Keune, S. Hong, M. Y. Hu, J. Zhao, T. S. Toellner, E. E. Alp, W. Sturhahn, T. S. Rahman, and B. R. Cuenya, "Influence of interfaces on the phonon density of states of nanoscale metallic multilayers: Phonon confinement and localization", *Physical Review B* **98**, 024308 (2018).
- ¹²¹I. Zegkinoglou, A. Zendegani, I. Sinev, S. Kunze, H. Mistry, H. S. Jeon, J. Zhao, M. Y. Hu, E. E. Alp, S. Piontek, M. Smialkowski, U.-P. Apfel, F. Körmann, J. Neugebauer, T. Hickel, and B. R. Cuenya, "Operando phonon studies of the protonation mechanism in highly active hydrogen evolution reaction

- pentlandite catalysts”, *Journal of the American Chemical Society*, **10.1021/jacs.7b07902** (2017).
- ¹²²A. D. Handoko, F. Wei, Jenndy, B. S. Yeo, and Z. W. Seh, “Understanding heterogeneous electrocatalytic carbon dioxide reduction through operando techniques”, *Nature Catalysis* **1**, 922–934 (2018).
- ¹²³N. Leonard, W. Ju, I. Sinev, J. Steinberg, F. Luo, A. S. Varela, B. R. Cuenya, and P. Strasser, “The chemical identity, state and structure of catalytically active centers during the electrochemical CO₂ reduction on porous Fe-nitrogen-carbon (Fe-N-C) materials”, *Chemical Science* **9**, 5064–5073 (2018).
- ¹²⁴T. N. Huan, N. Ranjbar, G. Rousse, M. T. Sougrati, A. Zitolo, V. Mougél, F. Jaouen, and M. Fontecave, “Electrochemical reduction of CO₂ catalyzed by Fe-N-C materials: a structure-selectivity study”, *ACS Catalysis*, **10.1021/acscatal.6b03353** (2017).
- ¹²⁵B. Roldan Cuenya, J. R. Croy, S. Mostafa, F. Behafarid, L. Li, Z. Zhang, J. C. Yang, Q. Wang, and A. I. Frenkel, “Solving the structure of size-selected Pt nanocatalysts synthesized by inverse micelle encapsulation”, *Journal of the American Chemical Society* **132**, 8747–8756 (2010).
- ¹²⁶B. R. Cuenya, J. R. Croy, S. Mostafa, F. Behafarid, L. Li, Z. Zhang, J. C. Yang, Q. Wang, and A. I. Frenkel, “Solving the Structure of Size-Selected Pt Nanocatalysts Synthesized by Inverse Micelle Encapsulation”, *Journal of the American Chemical Society* **132**, 8747–8756 (2010).
- ¹²⁷W. G. T. D. L. JR, *Iron(ii) halides*, English (1973).
- ¹²⁸W. Sturhahn, “CONUSS and PHOENIX: Evaluation of nuclear resonant scattering data”, *Hyperfine Interactions* **125**, 149–172 (2000).
- ¹²⁹B. Ravel and M. Newville, “ATHENA , ARTEMIS , HEPHAESTUS : data analysis for X-ray absorption spectroscopy using IFEFFIT”, *Journal of Synchrotron Radiation* **12**, 537–541 (2005).
- ¹³⁰H. d. Daas, M. Passacantando, L. Lozzi, S. Santucci, and P. Picozzi, “The interaction of Cu(100)-Fe surfaces with oxygen studied by X-ray photoelectron spectroscopy”, *Surface Science* **317**, 295–302 (1994).

- ¹³¹U. Gonser, C. Meechan, A. Muir, and H. Wiedersich, "Determination of néel temperatures in fcc iron", *Journal of Applied Physics* **34**, 2373–2378 (1963).
- ¹³²S. L. Heath, J. M. Charnock, C. D. Garner, and A. K. Powell, "Extended x-ray absorption fine structure (exafs) studies of hydroxo (oxo) iron aggregates and minerals, and a critique of their use as models for ferritin", *Chemistry–A European Journal* **2**, 634–639 (1996).
- ¹³³J. A. Varnell, E. C. M. Tse, C. E. Schulz, T. T. Fister, R. T. Haasch, J. Timoshenko, A. I. Frenkel, and A. A. Gewirth, "Identification of carbon-encapsulated iron nanoparticles as active species in non-precious metal oxygen reduction catalysts", *Nature Communications* **7**, 12582 (2016).
- ¹³⁴W. Li, Z. J. Coppens, L. V. Besteiro, W. Wang, A. O. Govorov, and J. Valentine, "Circularly polarized light detection with hot electrons in chiral plasmonic metamaterials", *Nature communications* **6**, 1–7 (2015).
- ¹³⁵L. Vitos, A. Ruban, H. Skriver, and J. Kollár, "The surface energy of metals", *Surface Science* **411**, 186–202 (1998).
- ¹³⁶S. G. Wang, E. K. Tian, and C. W. Lung, "Surface energy of arbitrary crystal plane of bcc and fcc metals", *Journal of Physics and Chemistry of Solids* **61**, 1295–1300 (2000).
- ¹³⁷I. Zegkinoglou, L. Pielsticker, Z.-K. Han, N. J. Divins, D. Kordus, Y.-T. Chen, C. Escudero, V. Pérez-Dieste, B. Zhu, Y. Gao, et al., "Surface segregation in cuni nanoparticle catalysts during co₂ hydrogenation: the role of co in the reactant mixture", *The Journal of Physical Chemistry C* **123**, 8421–8428 (2019).
- ¹³⁸J. Timoshenko, S. Roese, H. Hövel, and A. I. Frenkel, "Silver clusters shape determination from in-situ XANES data", *Radiation Physics and Chemistry*, [10.1016/j.radphyschem.2018.11.003](https://doi.org/10.1016/j.radphyschem.2018.11.003) (2018).
- ¹³⁹A. Patlolla, P. Baumann, W. Xu, S. D. Senanayake, J. A. Rodriguez, and A. I. Frenkel, "Characterization of Metal-Oxide Catalysts in Operando Conditions by Combining X-ray Absorption and Raman Spectroscopies in the Same Experiment", *Topics in Catalysis* **56**, 896–904 (2013).

- ¹⁴⁰J. Timoshenko, A. Halder, B. Yang, S. Seifert, M. J. Pellin, S. Vajda, and A. I. Frenkel, "Subnanometer Substructures in Nanoassemblies Formed from Clusters under a Reactive Atmosphere Revealed Using Machine Learning", *The Journal of Physical Chemistry C* **122**, 21686–21693 (2018).
- ¹⁴¹Y. T. Tan and K. J. Lushington, "Local atomic environment in silver chlorobromides from exafs", *Journal of Physics and Chemistry of Solids* **54**, 309–314 (1993).
- ¹⁴²M. C. Biesinger, "Advanced analysis of copper x-ray photoelectron spectra", *Surface and Interface Analysis* **49**, 1325–1334 (2017).
- ¹⁴³E. Wiberg, *Lehrbuch der anorganischen chemie* (Walter de Gruyter GmbH & Co KG, 2019).

List of Figures

Figure 1	Top-view of the SPM Aarhus 150 NAP reaction cell with open lid and position of the components. Note that the halogen lamp is inside the cutout of the lid and not visible from this angle. A: KolibriSensor or STM tip. B: Thermocouples. C: Cell gaskets and differential pumping holes. D:	19
Figure 2	Bruker MultiMode 8 atomic force microscope.	22
Figure 3	Qualitative depiction of photoelectron (left) and Auger electron emission (right). Left: Absorption of X-ray photon, emission of photoelectron. Right: Ionized atom; relaxation to lower energy state by transition of a higher shell electron to the core hole. The released energy induces the ejection of an Auger electron.	23
Figure 4	Photograph of the UHV system 1 'Bochum'. (A) Loadlock. (B) Preparation chamber (C) Analysis Chamber with XPS system (D) SPM Chamber.	26
Figure 5	Photograph of the UHV system 2 'MOKE'. (A) Loadlock. (B) Preparation chamber (C) EC-Cell transfer/loadlock chamber (UHV) and inert gas chamber (glass) containing the EC cell proper (D) Analysis Chamber with XPS system (E) STM Chamber.	27

- Figure 6 Double rail style sample holder for UHV experiments. **A:** Thermocouple contacts. **B:** Screws and washers to hold the sample. **C:** Holder head to lock and unlock the sample with the transfer rods. **D:** Sample base plate. **E:** Holder rails. 28
- Figure 7 Detailed view of the manipulator head. **A:** Thermocouple contacts. **B:** Clamps. **C:** E-beam filament. **D:** Plate mount for the sample holder. 29
- Figure 8 Plasma source inside preparation chamber with O₂ plasma ignited **A:** Plasma source exit with visible glow discharge. **B:** Manipulator head. 29
- Figure 9 The EC-Cell side of the MOKE system. **A:** Loadlock chamber for the transfer of samples from the UHV side to EC side, and vice versa. **B:** Inert gas chamber interfacing the loadlock (UHV side) and EC cell. The EC cell itself is not attached here. 30
- Figure 10 Vertical view of the EC-cell. **A:** Cell opening towards the sample side. **B:** Drain for electrolyte. **C:** Counter electrode (CE), Pt-mesh. **D:** Gas-in. **E:** Reference electrode (RE), Ag/AgCl (3M KCl). **D:** Gas-out. 32

- Figure 11 Schematic of an NRIXS experiment: **(A):** The synchrotron radiation is pulsed in bunches of 70 ps width with a separation of 153 ns. **Monochromatization:** A series of monochromators cuts the energy distribution in the incoming beam down to 1 meV, focused around the main excitation energy for ^{57}Fe , 14.41 keV. **Detection:** An avalanche photodiode detects the fluorescence response after the sample is irradiated. **(B):** Electronic and nuclear scattering intensities on a timescale. At $t = 0$, a pulse of synchrotron radiation excites the sample. Electron relaxation is immediate when compared to the nuclear response, which enables separation of electronic and nuclear contributions. **(C):** The raw NRIXS spectrum contains the elastic center peak (from the Mössbauer effect) and the inelastic side bands, which can be interpreted as phonon annihilation and creation. Similar to the Stokes and Anti-Stokes bands in Raman spectroscopy, the phonon creation contributes slightly more intensity. **(D):** The (partial) phonon density of states can be extracted from the raw spectrum. 35
- Figure 12 Different regions in an unnormalized X-ray absorption (XAS) spectrum. 37
- Figure 13 Schematic of the acrylic electrochemical cell for operando XAFS and NRIXS measurements. It is configured for a three electrode setup with the sample as the working electrode **(A)**, a leak-free Ag/AgCl (3M KCl) reference electrode **B** and a platinum mesh counter electrode **C**. A gas inlet is located on the top side **(D)**. **Right:** Configuration of the cell in relation to the beam during measurement. This cell is designed for fluorescence mode operation, where the sample is irradiated from the backside and the fluorescence is detected. Cell image made by Philipp Grosse. 38

- Figure 14 Nanoparticle synthesis via inverse micelle encapsulation and subsequent preparation of a monolayer of free standing nanoparticles on a substrate. **A:** Mixing of polymer and metal salt in toluene. **B:** Formation of inverse micelles. **C:** Dip coating, with inverse micelles attaching to the substrate. **D:** Free standing nanoparticles after removal of the polymer shell. 40
- Figure 15 SMART microscope at the BESSY II synchrotron. **A:** Specimen analysis chamber. **B:** Preparation chamber with the attached MPS plasma source **C:** 41
- Figure 16 STM images of the clean (0 s) Cu(100) (a-d) and Cu(111) (e-h) surfaces and those after the initial oxide growth following the exposure to an O₂-plasma at RT, 3×10^{-5} mbar for the times indicated. The lateral sizes of all images are 50 nm x 50 nm. The height scales are cut off at 1.2 nm and 2.3 nm to equalize each tile. Imaging parameters for a-d: U=-0.6 V to -1.5 V, $I_t = 115$ pA - 222 pA. Imaging parameters for e-h: U = -1.5 V, $I_t = 155$ pA - 289 pA. 47
- Figure 17 STM images of the (a,b) Cu(100) and (c,d) Cu(111) surfaces after 30 s plasma exposure at at RT, 3×10^{-5} mbar O₂. (a) Overview of Cu(100). (b) Area marked with the white rectangle in (a). Imaging parameters U = -0.6 V to -0.6 V, $I_t = 155$ pA. (c) Overview of Cu(111) and (d) zoom on the area around the island marked with the white rectangle in (c). Imaging parameters: U= -0.9 V, $I_t = 115$ pA. Green and white markers highlight key features of the surface morphology. 48
- Figure 18 STM images of the (a) Cu(100) and (b) Cu(111) surface after 120 s plasma exposure at RT and 3×10^{-5} mbar. In (a), marked with green shapes are key features discussed in the text. Imaging parameters: (a) U= -0.9 V, $I_t = 155$ pA (b) U = -1.5 V, $I_t = 115$ pA 49

- Figure 19 Profiles of line scans on the islands shown in figures 16 and 18 for 30 s and 120 s plasma exposure at RT and 3×10^{-5} mbar O_2 . In (a) and (b), Cu(100). In (c) and (d), Cu(111). The inserts show the position of the line scans corresponding to the graphs. The baselines (dotted) used for the determination of the apparent heights at the positions marked with arrows are also shown. 50
- Figure 20 LEEM images recorded before and after 30 s of O_2 plasma treatment of the Cu(100) and Cu(111) surface, top and bottom row, respectively. (a) clean Cu(100), electron energy $E = 20$ eV; (b) Cu(100) after plasma treatment, $E = 2.3$ eV; (c) clean Cu(111), $E = 20$ eV; (d) Cu(111) after plasma treatment, $E = 2.4$ eV. The O_2 pressure during the plasma exposure was 4×10^{-4} mbar. Note that the images do not represent the same local area on the sample. 52
- Figure 21 LEED images acquired on the Cu(100) and Cu(111) after different exposures to in situ O_2 plasma treatment, starting from the clean crystals (left), after 10 s, 180 s and finally after 1800 s of total oxidation time (right) performed in 4×10^{-4} mbar O_2 . The kinetic energy is 42 eV in all LEED patterns, except for the last column, where the energy is 32 eV. The dashed lines represent the unit cells of Cu crystals (in red), the $c(2 \times 2)$ reconstruction on Cu(100) (yellow square), unit cells of the two rotational domains on Cu(100) (green and purple, on top), respectively quasi (2×2) reconstruction and unit cell of $Cu_2O(111)$ (green, at the bottom). 53

- Figure 22 Cu LMM AES spectra measured before and after different in situ O₂-plasma exposures at 3×10^{-5} mbar of (a),(b) Cu(100) and (c),(d) Cu(111) single crystal surfaces. The content of the different Cu species was determined by fitting and deconvolution of the Cu LMM signal (b and d). The corresponding fits are shown in the appendix in figure 42. The connecting lines are meant as guides for the eyes. 57
- Figure 23 NEXAFS after *in situ* oxygen plasma treatment of Cu(100) and Cu(111) at 4×10^{-4} mbar O₂, top and bottom row respectively. (a, c) Cu L-edge NEXAFS data at different doses. (b, d) The analysis displays the content of metallic Cu, Cu₂O and CuO versus oxygen plasma treatment time. The O₂ pressure during the plasma exposure was 4×10^{-4} mbar. 59
- Figure 24 Oxide film growth on Cu(100) (a-c) and on Cu(111) (d-f) by oxygen plasma treatment at 4×10^{-4} mbar. (a) and (d) raw data and fitting of the NEXAFS composition using a damping model. (b and e) Schematic of the oxidation model showing the initial metallic copper surface, the intermediate state with a complete Cu₂O film on the Cu(100) crystal and a mixture of Cu₂O and CuO for the Cu(111) surface. As a final state, the CuO film overgrows the Cu₂O film. (c, f) exhibit the sample depth profile over the plasma exposure time using a damping model. After 30 s the Cu₂O film keeps a constant thickness and is overgrown by the CuO film whereas the growth rate is damped over dosage. 61

- Figure 25 (a) Constant current STM image of the UHV cleaned Cu(100) surface. $U_{bias} = 0.83$ V, $I_t = 0.66$ nA (b) Constant current STM image with atomic resolution from the same measurement as (a). $U_{bias} = 0.41$ V, $I_t = 0.23$ nA. Image size is 8.35 nm x 8.35 nm. (c) Ball model of a Cu single crystal with a (100) surface termination on top. 71
- Figure 26 AFM images of the UHV cleaned Cu(100) surface in air. The white box in (a) marks the location of the scan area of (b). 72
- Figure 27 AFM images (a, b) of the UHV-cleaned Cu(100) surface after 20 s electropolishing. The white arrows in (a) indicate the position of a step edge. (c) Height profiles along the numbered lines in (b). 74
- Figure 28 AFM image of a UHV prepared Cu(100) surface after 1 h of electrolysis at a fixed potential of -1 V vs. RHE in 0.1 M KHCO_3 . The crystal was transferred from UHV to the electrochemical cell without exposure to air. The height scale is cut off at 7 nm and 4.5 nm to enhance the contrast towards the nanoroughness of the substrate. 75
- Figure 29 AFM images (a,c) and 3D representations (b,d) of UHV prepared Cu(100) surfaces after 1 h of pulsed potential sequences at anodic potentials of (a,b) 0.6 V vs. RHE and (c,d) 0.8 V vs. RHE in 0.1 M KHCO_3 . The crystals were transferred from UHV to the electrochemical cell without exposure to air. 77
- Figure 30 AFM images of UHV-prepared Cu(100) surfaces after 1 h of pulsed potential sequences at anodic potentials of (a,b) 0 V vs. RHE and (c,d) 0.4 V vs. RHE. Each experiment was conducted in 0.1 M KHCO_3 . The crystals were transferred from UHV to the electrochemical cell without exposure to air. 78

Figure 31	AFM images of UHV prepared Cu(100) surfaces after 1 h of pulsed potential sequences at cathodic potentials durations of (a) 0.5 s and (b) 29 s, with anodic potentials of 0.6 V and cathodic potentials of -1 V vs RHE in 0.1 M KHCO_3 . The crystal was transferred from UHV to the electrochemical cell without exposure to air.	79
Figure 32	AFM images of the UHV prepared Cu(100) surface after 1 h of (a) pulsed potential sequences at an anodic potential of 0.6 V vs. RHE and (b) immediate subsequent electrolysis at -1 V vs RHE in 0.1 M KHCO_3 for a duration of 1 h. The crystal was transferred from UHV to the electrochemical cell without exposure to air.	80
Figure 33	Tapping mode AFM images of: (a) ^{57}Fe , (b) $^{57}\text{FeCu}$, (c) $^{57}\text{FeAg}$ NPs deposited on $\text{SiO}_2/\text{Si}(100)$ after a N_2 plasma treatment for polymer removal. Average particle sizes are: 7.8 nm for ^{57}Fe , 5.2 nm for $^{57}\text{FeCu}$ and 4.2 nm for $^{57}\text{FeAg}$. Panels (d) to (h) show analogous images of the non-enriched NPs.	89
Figure 34	Size histograms of the nanoparticle arrays shown in Fig. 33.	90
Figure 35	Background-subtracted XPS spectra and corresponding fits of the Fe-2p core level region of as-prepared (a) FeCu and (b) FeAg NPs supported on $\text{SiO}_2/\text{Si}(100)$	91
Figure 36	Background-subtracted XPS spectra of the (a) Cu-2p and (b) Ag-3d core level regions of FeCu and FeAg NPs deposited on $\text{SiO}_2/\text{Si}(100)$	92
Figure 37	Selectivity for the reaction products of CO_2RR obtained from Fe (6.7 nm), FeCu (5.3 nm), FeAg (4.1 nm), Ag (4.1 nm) and Cu (5.6 nm) NPs after 1h of reaction at -1.1 V vs RHE in CO_2 -saturated 0.1 M KHCO_3 and a CO_2 flow of 20 mL/min. Plotted in red are the geometric current densities of each sample (right-hand side red scale).	93

- Figure 38 (a) ^{57}Fe -partial PDOS, $g(E)$, obtained from raw NRIXS spectra of ^{57}Fe and $^{57}\text{FeCu}$ NPs in air and under *operando* CO_2RR . The spectra in (b) display the *operando* CO_2RR PDOS data of ^{57}Fe , $^{57}\text{FeCu}$ and $^{57}\text{FeAg}$ NPs together with a bulk bcc-Fe reference foil for comparison.¹¹⁸ (c) ^{57}Fe -partial PDOS of $^{57}\text{FeAg}$ NPs plotted together with thin ^{57}Fe layers deposited on a Ag film (4 nm) reproduced from Ref.¹¹⁸ Representative error bars in different regions of the spectra are also shown. The spectra have been vertically offset for better visibility and the vertical lines indicate the position of the two TA and the LA peaks of bulk bcc-Fe. . 95
- Figure 39 Fe K-edge XANES (a,c) and Fourier-transforms of k2-weighted EXAFS data (phase-uncorrected) and the corresponding first-shell fits (dotted lines) (b,d) of $^{57}\text{FeCu}$ and $^{57}\text{FeAg}$ NPs as prepared (as-is) and under CO_2RR conditions at -1.1 V vs RHE in 0.1 M KHCO_3 after 3.5 h ($^{57}\text{FeCu}$) and 1.5 h ($^{57}\text{FeAg}$). Reference spectra from lepidocrocite $\text{FeO}(\text{OH})$ ¹²⁹ and a bulk iron foil are also shown for comparison. 98
- Figure 40 Cu K-edge (a,b) and Ag K-edge (c,d) XANES (a,c) and Fourier-transforms of k2-weighted EXAFS data (phase-uncorrected) (b,d) of $^{57}\text{FeCu}$ and $^{57}\text{FeAg}$ NP samples in as-prepared state (as-is) and under CO_2RR conditions (-1.1 V vs RHE in 0.1 M KHCO_3 after 1.5 h ($^{57}\text{FeCu}$) and 2.5 h ($^{57}\text{FeAg}$)) Reference spectra from CuO , Cu-foil, AgCl ¹²⁹ and a Ag-foil are shown for comparison. 100
- Figure 41 STEM images and EDX line cans (green horizontal lines) of micellar FeCu and FeAg NPs supported on nanocrystalline SiO_2 (a and c) and on carbon powder (b and d). Images (a) and (c) were obtained before the reaction and (b) and (d) after CO_2RR . Violet lines are reference lines to guide the eye.103

- Figure 42 Cu LMM spectra and fitted components on (a) Cu(100) and (b) Cu(111) after indicated duration of plasma treatment at RT in 3×10^{-5} mbar O₂. 142
- Figure 43 LEEM I-V curves showing the MEM-LEEM transition during the initial oxidation steps on (a) Cu(100) single crystal, respectively (b) Cu(111) single crystal plasma treatment was done at RT in 3×10^{-5} mbar O₂. 143
- Figure 44 Work function measurements during the oxide films grown on Cu(100) (black) and Cu(111) (red). 144
- Figure 45 NEXAFS spectra measured at different stages of plasma treatment. (a) Cu L edge, respectively (b) O K edge NEXAFS spectra of the initial metallic surface and after 10 s, 180 s and 1800 s of plasma oxidation at 4×10^{-4} mbar O₂, proving characteristic fingerprints of different copper oxide species. In the case of image (b), the spectrum measured for the clean sample was used for the normalization of the files, and therefore is not shown 145
- Figure 46 Example of fitting the components: The experimental curve (dark blue) is fitted by a sum of the NEXAFS components of Cu⁰, Cu⁺ and Cu²⁺ (black, red and green curves, respectively). The residual in the bottom exhibits the quality of the fit, whereas the emphasis is put on the range of the first three maxima. The data shows the NEXAFS measurement of the Cu(111) surface after an overall 30 min treatment with oxygen plasma. 146
- Figure 47 Fitting of the XPS data with the same model as applied for the NEXAFS data. Plasma treatment was done at 3×10^{-5} mbar O₂. Fitting parameters are given in Table 4 . 148

Figure 48	a) and d) Fitting the time dependence of the NEXAFS components with the linear (dashed lines) and the damping model (dashed dotted lines) for plasma treatment on Cu(100) and Cu(111), left and right column respectively. Plasma treatment was done at 4×10^{-4} mbar O ₂ . b) and e) display the thickness of the growing CuO (red) and Cu ₂ O (green) film. A schematic model for the film growth is given in the bottom. The fitting parameters are listed in table 5	150
Figure 49	⁵⁷ Fe-partial PDOS of ⁵⁷ FeCu plotted together with 1.5 nm thin Fe layers deposited on Cu films (4 nm) reproduced from Roldan et al. ¹¹⁸ The spectra were vertically offset for better legibility.	154
Figure 50	Fourier-transformed EXAFS data at different times after starting the measurement under CO ₂ RR conditions. The total measurement time was about 1 h. Individual spectra shown here correspond to a binned group of spectra over a time of 15 min each.	155
Figure 51	The final product ⁵⁷ FeCl ₂ · 2 H ₂ O, synthesized from ⁵⁷ Fe-foil. Note the faint blue hue characteristic for the dihydrate.	159

List of Tables

Table 1	Products and half-cell potentials of several CO ₂ reduction reactions.	11
Table 2	Tabulated summary of surface treatments and reaction conditions applied to Cu(100).	70
Table 3	Coordination numbers (CN) and interatomic distances (R), derived from the fit of EXAFS data of samples ⁵⁷ FeCu and ⁵⁷ FeAg at the Fe, Cu and Ag K-edges. The data were measured in air (as-is) and <i>operando</i> during CO ₂ RR at −1.1 V vs RHE in 0.1 M KHCO ₃ after 1.5 h to 3.5 h. The uncertainty of the last digit is given in parentheses. Additional parameters and fit results are shown in the appendix in tables 6 and 7. A single Fe-Fe scattering path was used to fit the overlapping contributions from the first two coordination shells in bcc Fe due to the limited resolution in R-space as a result of the short Fe K-edge spectrum.	105
Table 4	Parameters extracted from the fitting of the composition evolution of Cu, Cu ₂ O and CuO species as function of exposure time at 3×10^{-5} mbar of oxygen for Cu(100) and Cu(111).	148
Table 5	Parameters extracted from the fitting of the composition evolution of Cu, Cu ₂ O and CuO species as function of exposure time at 3×10^{-5} mbar of oxygen for Cu(100) and Cu(111).	151

Table 6	Detailed fitting parameters: R-range, k-range and Rbkg (the frequency cutoff used to separate the background contribution) of the EXAFS fits.	155
Table 7	EXAFS Debye-Waller factor (σ^2) and fit quality ("R-factor", as reported by Artemis program) of the EXAFS fits.	156

8 Appendix for Plasma-assisted Oxidation of Cu(100) and Cu(111)

8.1 Cu LMM deconvolution

In order to quantify the composition of the plasma treated surfaces, we performed peak fitting of the Cu LMM spectra on a Shirley background, based on the procedure and using the constraints outlined in Biesinger, M. C. (2017).¹⁴² The obtained fit curves are shown in figure 42. The binding energies were referenced to the most intense LMM peak assumed to correspond to metallic Cu. We used the six most intense peaks of the metallic Cu, and four peaks for Cu₂O and CuO each. The peak shapes are modelled with mixed Gaussian-Lorentzian (GL) line shapes. One should note that quantification of copper in different oxidation states is quite challenging, and we want to emphasize that the overall trend of the oxidation process is the aspect of interest here. The Cu LMM data from XPS measurements along the fitted components is shown in figure 42.

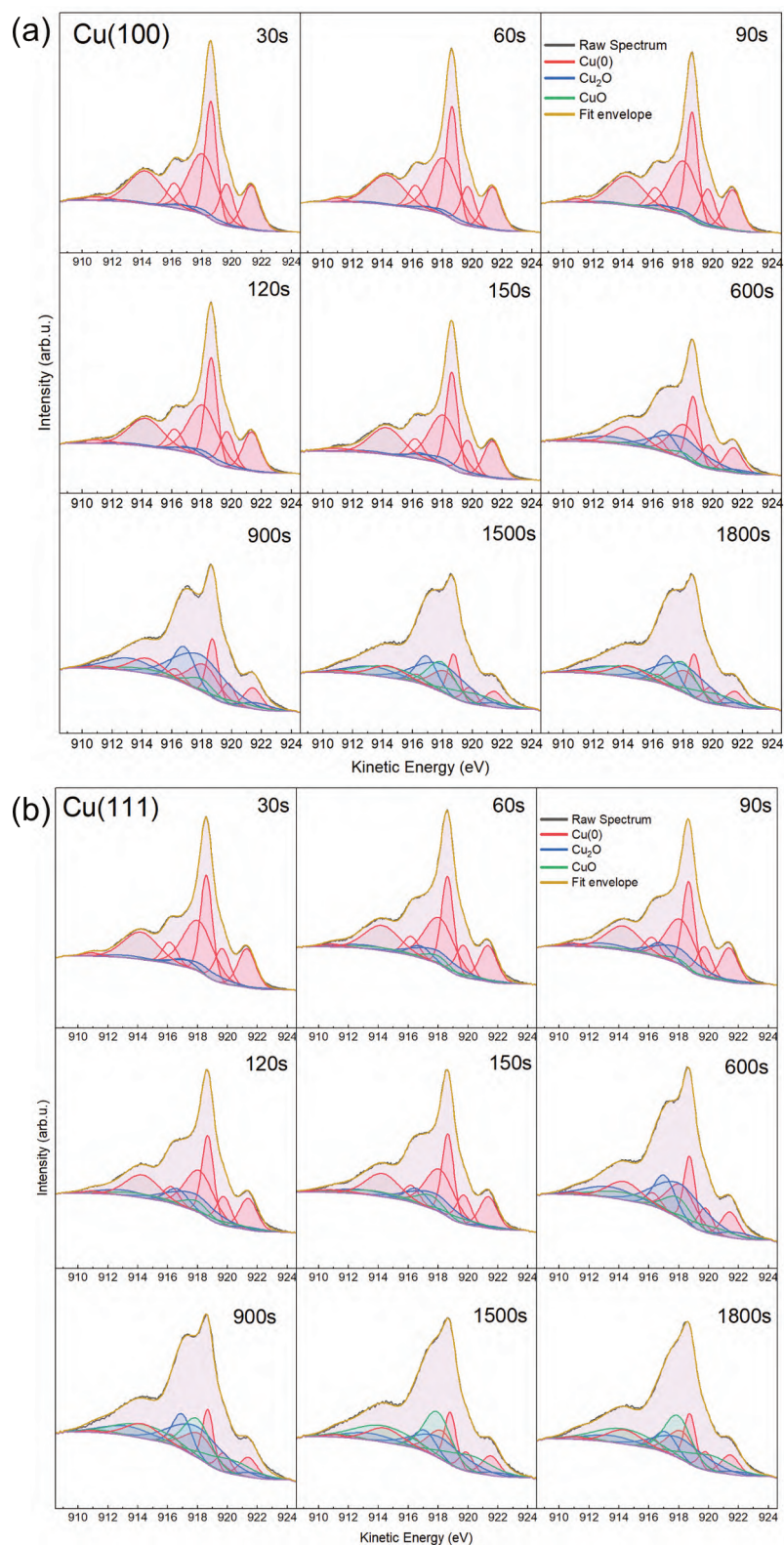


Figure 42: Cu LMM spectra and fitted components on (a) Cu(100) and (b) Cu(111) after indicated duration of plasma treatment at RT in 3×10^{-5} mbar O₂.

8.2 Work function measurements

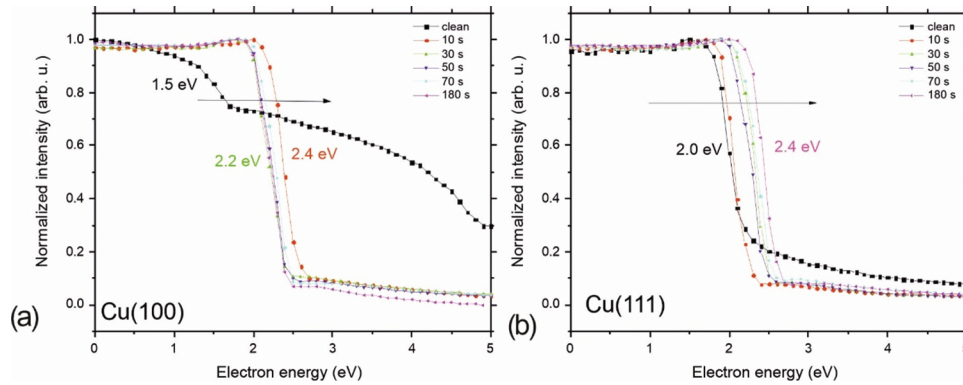


Figure 43: LEEM I-V curves showing the MEM-LEEM transition during the initial oxidation steps on (a) Cu(100) single crystal, respectively (b) Cu(111) single crystal plasma treatment was done at RT in 3×10^{-5} mbar O_2 .

The LEEM I-V curves allow the determination of the MEM-LEEM transition value, which represents the value at which the electron kinetic energy can overcome the potential energy of the surface and penetrate, therefore, into the bulk. Due to this effect, the MEM-LEEM transition values are directly related with the surface. The transition energy of the clean surface is used to be calibrated to the known work function by an energy offset, which is used also all further measurements. Additionally, we determined the change in surface work function (WF) due to plasma induced oxidation. Therefore, the image intensity has been recorded in dependence on the sample voltage (LEEM I-V) around the MEM-LEEM transition, e.g. from the voltage range where all electrons are reflected in front of the surface up to voltages where the electrons can overcome the surface potential and are partially reflected within the crystal. Considering that the MEM-LEEM transition can be correlated with the surface WF, one can track WF changes as function of the overall plasma treatment time. Fig. 44 presents the WF variation as determined from the I-V curves represented in Fig. 43 for both crystal orientations during the incipient steps, using the WF of pristine Cu(100) at 4.65 eV, respectively 4.94 eV for Cu(111) as references.

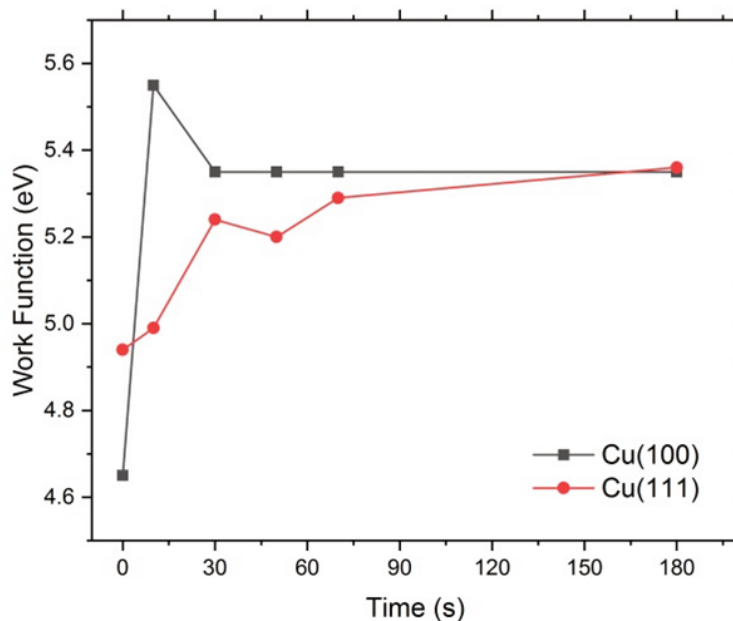


Figure 44: Work function measurements during the oxide films grown on Cu(100) (black) and Cu(111) (red).

For the two Cu surface orientations there is already a significant difference between the initial, i.e. clean state, and the first plasma treatment of 10 s in 4×10^{-4} mbar O_2 . The WF suffers a shift of +0.9 eV on Cu(100), which can be correlated also with the formation of the $c(2 \times 2)$ superstructure, as observed in LEED (see Fig. 21), while the (111) crystal does not show, interestingly, a reasonable shift. This difference points out not only the intrinsic nature between the two orientations but could also indicate different initial oxidation behaviour. Upon further dosage, the WF on Cu(100) gets stabilized to 5.35 eV. In the case of Cu(111), even though it does not show any further change after the first treatment, there is a gradual shift of +0.4 eV up to a total treatment of 180 s at 4×10^{-4} mbar O_2 , which translates to a WF value of 5.34 eV, the same as obtained for Cu(100) surface. The work function of the oxide surface is in good agreement with published values in the range between 5.3 and 5.5 eV. The comparison of the two curves in figure 44 proves that the gradual dosage of oxygen plasma on the two orientations with initially different WF equalizes the values to 5.35 eV, indicating that in both cases the same kind of oxide surface is formed at the end.

8.3 O K-edge NEXAFS

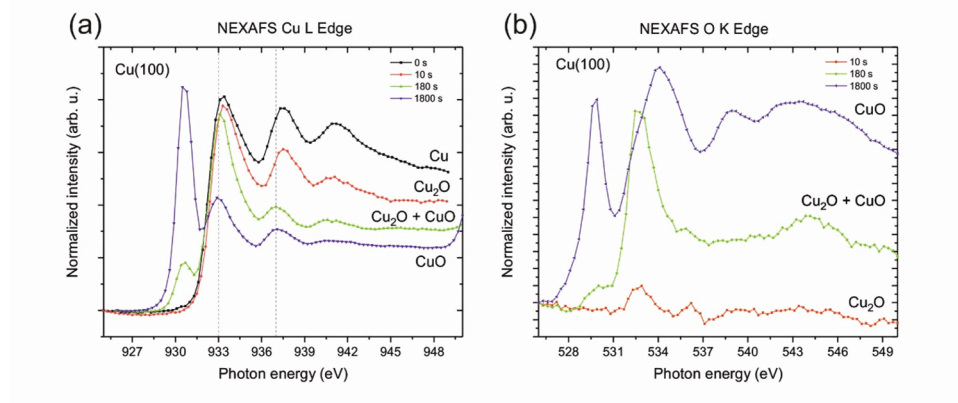


Figure 45: NEXAFS spectra measured at different stages of plasma treatment. (a) Cu L edge, respectively (b) O K edge NEXAFS spectra of the initial metallic surface and after 10 s, 180 s and 1800 s of plasma oxidation at 4×10^{-4} mbar O_2 , proving characteristic fingerprints of different copper oxide species. In the case of image (b), the spectrum measured for the clean sample was used for the normalization of the files, and therefore is not shown

8.4 Composition Analysis of NEXAFS spectra

The analysis of the Cu L edge NEXAFS spectra implies the initial state of the crystal as being metallic and that the further spectra are a linear combination of characteristic spectra of metallic copper (Cu^0), Cu_2O (Cu^+) and CuO (Cu^{2+}) at a certain exposure time t :

$$I(t) = \sum_{i=1}^3 a_i(t) I_i(Cu^i) = a_1 I_1(Cu^0) + a_2 I_2(Cu^+) + a_3 I_3(Cu^{2+}) \quad (7)$$

where a_i represents normalized weighting factors at a certain time, such that $a_1 + a_2 + a_3 = 1$. They correspond to the "composition" of Cu^0 , Cu^+ and Cu^{2+} in the spectra in figure 23

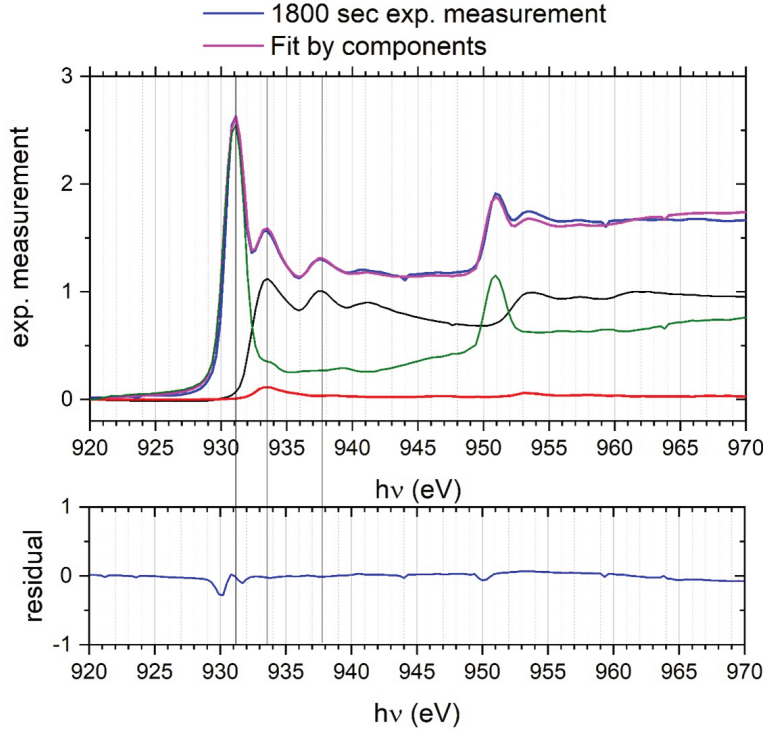


Figure 46: Example of fitting the components: The experimental curve (dark blue) is fitted by a sum of the NEXAFS components of Cu^0 , Cu^+ and Cu^{2+} (black, red and green curves, respectively). The residual in the bottom exhibits the quality of the fit, whereas the emphasis is put on the range of the first three maxima. The data shows the NEXAFS measurement of the $\text{Cu}(111)$ surface after an overall 30 min treatment with oxygen plasma.

8.5 Model of Copper oxide formation for Cu(100)

The model presented in the main text assumes that the Cu_2O is growing after the initial oxidation steps, until a certain thickness δ is reached, above which the growth is continued on a thickness Δ as CuO . Starting with the assumption that each Cu atom from the depth z contributes with an intensity $I_0 e^{(-\frac{z}{\Gamma})}$, it yields the following terms for the three contribution:

$$I_{\text{Cu}^{2+}} = n_{2+} I_0 (1 - e^{(-\frac{z}{\Gamma})}) \quad (8)$$

$$I_{\text{Cu}^+} = n_+ I_0 (1 - e^{(-\frac{\delta}{\Gamma})}) e^{(-\frac{\Delta}{\Gamma})} \quad (9)$$

$$I_{\text{Cu}^0} = n_0 I_0 (1 - e^{(-\frac{\delta+\Delta}{\Gamma})}) \quad (10)$$

where Γ represents the mean free path length of the electrons at the detected energy which is assumed to be the same for all three copper species. n_0 , n_+ and n_{2+} are atomic concentrations of copper in the metallic, the Cu_2O and CuO phase. The intensity I_0 is assumed to be identical for all Cu atoms. The normalization of the intensity with the total intensity

$$I_{total} = I_{Cu^0} + I_{Cu^+} + I_{Cu^{2+}} \quad (11)$$

yields in the three normalized intensities which describe the intensity composition of figure 9a and d and is used in formula eq1

$$a_{Cu^{2+}} = \frac{I_{Cu^{2+}}}{I_{total}} \quad (12)$$

$$a_{Cu^+} = \frac{I_{Cu^+}}{I_{total}} \quad (13)$$

$$a_{Cu^0} = \frac{I_{Cu^0}}{I_{total}} \quad (14)$$

It is to be noted that the sum of three components gives:

$$a_{Cu^{2+}} + a_{Cu^+} + a_{Cu^0} = 1 \quad (15)$$

8.6 Composition fit of XPS data

Analogous to the fit of the NEXAFS data the XPS composition data were fitted with the damping model. Fig 47 shows the experimental data with the model fit.

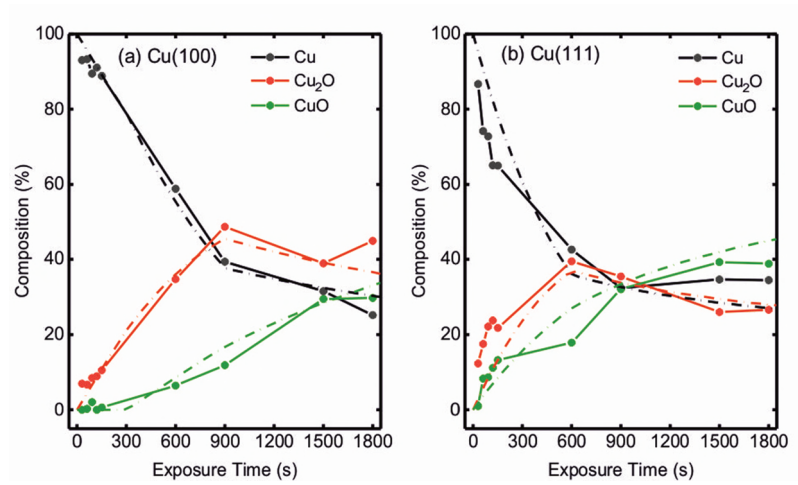


Figure 47: Fitting of the XPS data with the same model as applied for the NEXAFS data. Plasma treatment was done at 3×10^{-5} mbar O₂. Fitting parameters are given in Table 4

Table 4: Parameters extracted from the fitting of the composition evolution of Cu, Cu₂O and CuO species as function of exposure time at 3×10^{-5} mbar of oxygen for Cu(100) and Cu(111).

Cu(100)	
Mean free path length	2 nm
Thickness of buried Cu ₂ O	2.2 nm
Initial oxidation rate of CuO	0.0008 nm/s
Effective oxidation length (damping)	1.75 nm
Cu(111)	
Mean free path length	2 nm
Thickness of buried Cu ₂ O	2 nm
Initial oxidation rate of CuO	0.002 nm/s
Effective oxidation length (damping)	0.8 nm

8.7 Correlation between film thickness and plasma exposure time

The growth of the Cu_2O film can be described as a linear increase between 0 to thickness δ within 30 s (at 4×10^{-4} mbar), the value above which the thickness remains constant. The CuO starts to grow on top from $t=30$ s on. The time dependence of thickness δ of this growing CuO film might be described by two models:

1. Simple linear model: $\Delta(t) = R \times t$, with R being the constant oxidation rate of CuO
2. Damping model, in which the oxidation rate is damped by the thickness of the film

In both cases, the damping of the composition in Fig. 23(b) and (d) is fitted over the full exposure time of exposure time of 1800 s (at 4×10^{-4} mbar O_2). We make the remark that it was not yet considered that the copper layers expand in volume when the oxygen is incorporated into copper, which means that the oxide grows into the bulk, but also increases the height (see next subsection). The damping model considers that the film grows with dosage according to the following rate equation:

$$\frac{d\Delta}{dt} = R e^{(-\frac{\Delta}{\Lambda})} \quad (16)$$

where R is the initial oxidation rate, i.e. the oxidized film thickness per time. Nevertheless, the oxidation is hindered when the film gets thicker. The damping of the process is described by the exponential factor with Λ being the effective oxidation length. Considering the starting condition $\Delta(t=0 \text{ s}) = 0 \text{ nm}$, i.e. no oxide film in the beginning, the solution of the rate equation is:

$$\Delta(t) = \Lambda \ln\left(1 + \frac{R}{\Lambda} t\right) \quad (17)$$

For $Rt \ll \Lambda$ or small values of t this formula can be approximated as $\Delta(t) = Rt$, which is just the expected initial linear behaviour. Figure 48 shows clearly that

fitting with the damping model describes the time dependence of the NEXAFS components much better than the linear model.

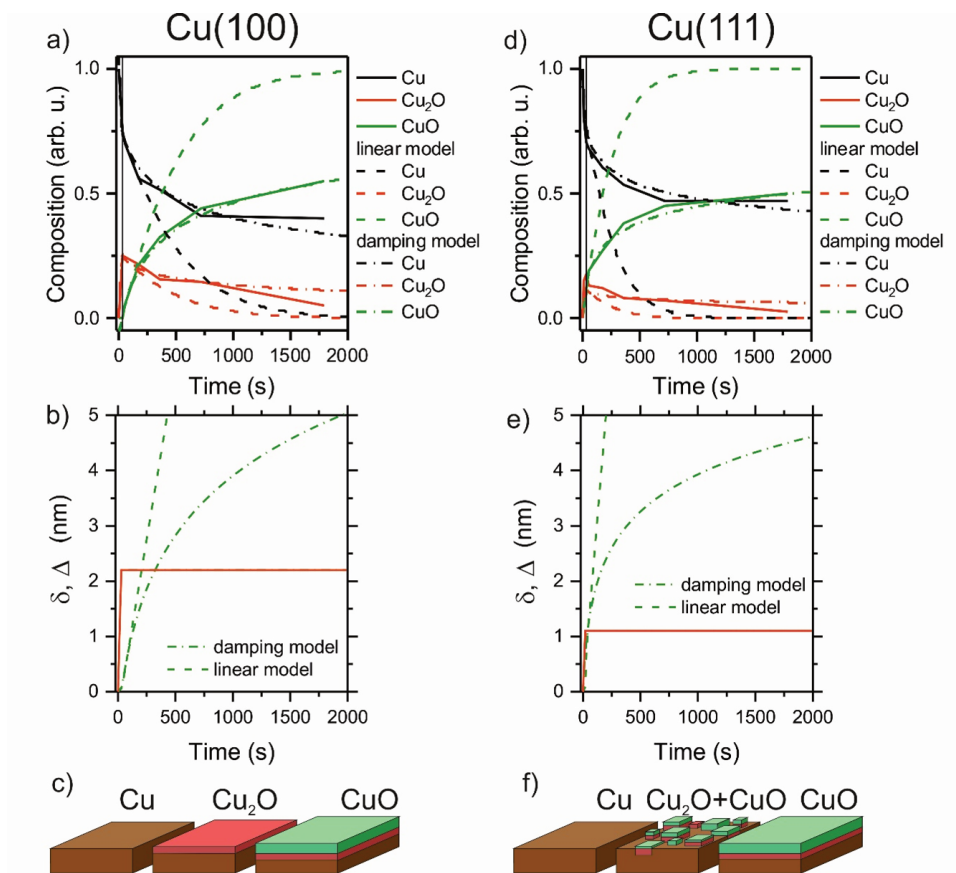


Figure 48: a) and d) Fitting the time dependence of the NEXAFS components with the linear (dashed lines) and the damping model (dashed dotted lines) for plasma treatment on Cu(100) and Cu(111), left and right column respectively. Plasma treatment was done at 4×10^{-4} mbar O₂. b) and e) display the thickness of the growing CuO (red) and Cu₂O (green) film. A schematic model for the film growth is given in the bottom. The fitting parameters are listed in table 5

Table 5: Parameters extracted from the fitting of the composition evolution of Cu, Cu₂O and CuO species as function of exposure time at 3×10^{-5} mbar of oxygen for Cu(100) and Cu(111).

	Linear model	Damping model
Cu(100)		
Mean free path length	$\Gamma=5$ nm	$\Gamma=5$ nm
Thickness of buried Cu ₂ O	$\delta=2.2$ nm	$\delta=2.2$ nm
Initial oxidation rate of CuO	$R=0.0125$ nm/s	$R=0.015$ nm/s
Effective oxidation length (damping)		$\Lambda=1.75$ nm
Cu(111)		
Mean free path length	$\Gamma=5$ nm	$\Gamma=5$ nm
Thickness of buried Cu ₂ O	$d=1.1$ nm	$d=1.1$ nm
Initial oxidation rate of CuO	$R=0.025$ nm/s	$R=0.05$ nm/s
Effective oxidation length (damping)		$\Lambda=1$ nm

9 Appendix for Operando NRIXS and XAFS Investigation of Segregation phenomena in FeCu and FeAg nanoparticle catalysts during CO_2 electroreduction

9.1 Fitting of XPS spectra

All binding energies were referenced against the 2s peak of $\text{SiO}_2/\text{Si}(100)$. For peak fitting, Shirley backgrounds were used, and Gaussian-Lorentzian (GL) line shapes. Quantitative information of the ratio between different elements and for one element the relative contribution of different oxidation states were extracted from the analysis of the respective areas in the XPS spectra. The area of each element was previously corrected with the relative sensitivity factors RSF (tabulated values specific for each XPS instrument).

9.2 Additional NRIXS data

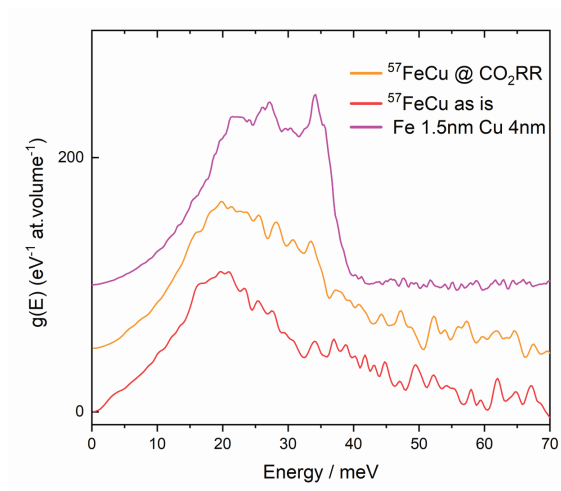


Figure 49: ^{57}Fe -partial PDOS of $^{57}\text{FeCu}$ plotted together with 1.5 nm thin Fe layers deposited on Cu films (4 nm) reproduced from Roldan et al.¹¹⁸ The spectra were vertically offset for better legibility.

9.3 Supplementary EXAFS Information

All EXAFS spectra shown are displayed phase-uncorrected. Fitting was performed using the Artemis software.¹²⁹ Photoelectron scattering phases and amplitudes were calculated using the built-in FEFF-6 code and employing bulk metal models to simulate the phases and amplitudes of the metal-metal bonds in the reduced samples, CuO and FeO(OH) models to simulate the phases and amplitudes for the metal-oxygen bonds, and an AgCl model for the Ag-Cl bond description. The fitting parameters were the coordination numbers (CN), interatomic distances R , disorder factors σ^2 for metal-oxygen, metal-chloride and metal-metal bonds, as well as the correction to photoelectron reference energy ΔE_0 . The amplitude reduction factor due to many-electron excitations (S^2_0 factor) was obtained in the fits of reference materials (corresponding metal foils). Due to the short length of the spectra acquired and, hence, limited resolution in R -space, we included only a single path to model the overlapping metal-metal contributions from the first two coordination shells in bcc-type iron. Fitting was

carried out in R-space. The R-ranges used for fitting, and the k-ranges used for Fourier transformation, are reported in Table 6.

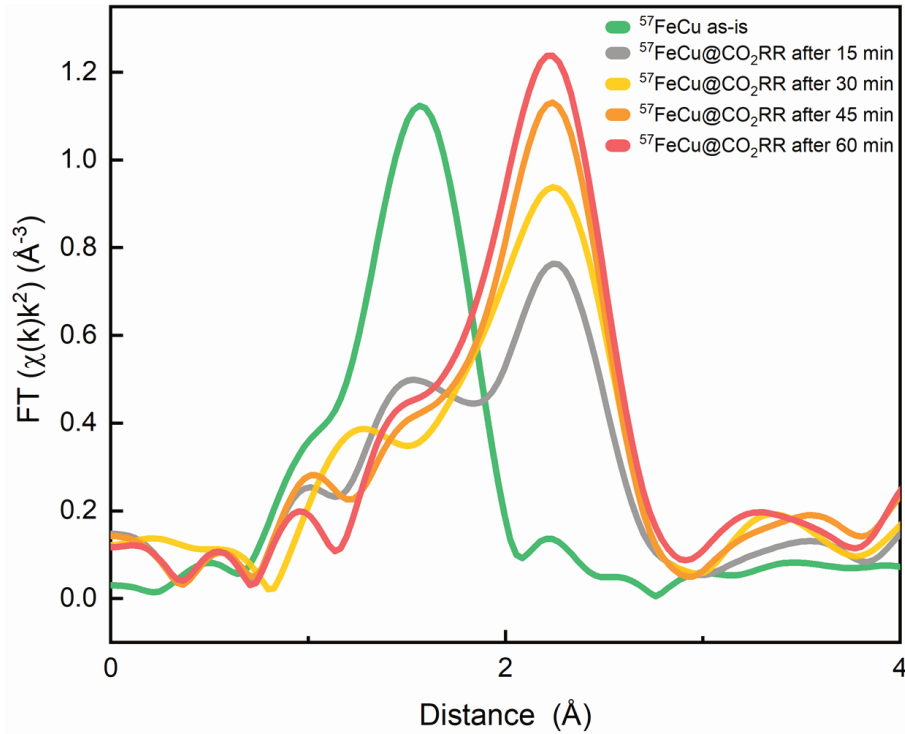


Figure 50: Fourier-transformed EXAFS data at different times after starting the measurement under CO₂RR conditions. The total measurement time was about 1 h. Individual spectra shown here correspond to a binned group of spectra over a time of 15 min each.

Table 6: Detailed fitting parameters: R-range, k-range and R_{bkg} (the frequency cutoff used to separate the background contribution) of the EXAFS fits.

Spectrum	R-range Å	k-range (Å ⁻¹)	R _{bkg} (Å)
Cu K-edge in ⁵⁷ FeCu as-is	1.0-3.0	3.0-9.0	1.0
Cu K-edge in ⁵⁷ FeCu CO ₂ RR	1.0-3.0	3.0-9.0	1.0
Fe K-edge in ⁵⁷ FeCu as-is	1.0-3.0	3.0-9.0	1.0
Fe K-edge in ⁵⁷ FeCu operando	1.0-3.0	3.0-9.0	1.0
Ag K-edge in ⁵⁷ FeAg as-is	1.0-3.2	3.0-9.0	1.0
Ag K-edge in ⁵⁷ FeAg operando	1.0-3.2	3.0-9.0	1.0
Fe K-edge in ⁵⁷ FeAg as-is	1.0-3.0	3.0-9.0	1.0
Fe K-edge in ⁵⁷ FeAg operando	1.0-3.0	3.0-9.0	1.0

Table 7: EXAFS Debye-Waller factor (σ^2) and fit quality ("R-factor", as reported by Artemis program) of the EXAFS fits.

Spectrum	$\sigma^2 / \text{\AA}^2$	R-factor (%)
⁵⁷ FeAg as-is		
Ag-Cl	0.018 ± 0.002	2.71
Fe-O	0.011 ± 0.003	1.96
⁵⁷ FeAg operando		
Ag-Ag	0.009 ± 0.001	2.86
Fe-Fe	0.008 ± 0.013	2.67
Fe-O	0.002 ± 0.005	2.04
⁵⁷ FeCu as-is		
Cu-O	0.003 ± 0.002	1.99
Fe-O	0.023 ± 0.023	2.76
⁵⁷ FeCu operando		
Cu-Cu	0.008 ± 0.015	2.53
Cu-O	0.006 ± 0.003	1.94
Fe-Fe	0.008 ± 0.004	2.03
Fe-O	0.004 ± 0.007	2.61

9.4 Synthesis of ⁵⁷FeCl₂ · 2 H₂O

Here, the synthesis of the isotopically enriched nanoparticle samples is discussed. I expand here on material that was discussed previously in my work. While isotope-labeled compounds for the life sciences (proteins, DNA, RNA) and stable isotopes in its elemental form (usually foils) are readily available, commercial supply of isotope-enriched metal salts is both rare and expensive.

Since elemental iron cannot be used for inverse micellar encapsulation, a corresponding iron salt had to be synthesized. For this method, I used iron chloride successfully in the past. It was therefore chosen as the target product.

One should note however that the hydrates are much easier to work with than the anhydrides, which is also a consideration when synthesizing the salt.

Iron chloride is the trivial name for both FeCl_2 and FeCl_3 and their hydrates, which contain Fe(II) or Fe(III), respectively. Both salts are viable for the proposed method; however, synthesis of a clean product starting from the foil is a challenge, if acceptable yields, purity and costs are to be achieved at the same time. Storage also needs to be planned in advance, since one of the main obstacles during synthesis is the rapid oxidation of Fe(II) to Fe(III) in air. Sunlight and moisture accelerate this process. Both compounds are also fairly hygroscopic, depending on the amount of crystal water that is already absorbed; the anhydrous forms will absorb air moisture immediately upon contact. Storage under inert atmosphere (e.g., in a glove box) or vacuum is necessary to keep a pure sample of any of the two salts.¹⁴³

Pathways based on the elements ($\text{Cl}_2(\text{g})$ and $\text{Fe}(\text{s})$) require very high temperatures up to 1000°C , which requires special precautions and equipment. Therefore, a more complex route was chosen that could be done with the present equipment: Solvation of the iron foil in concentrated hydrochloric acid under inert atmosphere and subsequent heating under vacuum to obtain the dihydrate $\text{FeCl}_2 \cdot 2\text{H}_2\text{O}$.

The target product requires stringent observation of temperature and pressure during reaction and drying, in addition to a carefully maintained screen of inert gas during and after reaction to prevent partial oxidation.¹²⁷ One might argue that a complete oxidation of all iron ions to Fe(III) by addition of H_2O_2 would alleviate all problems regarding stoichiometry; while I agree that it seems a plausible option, two considerations lead to my decision to opt for the more challenging product. First, the amount of isotope enriched iron foil was very small, and every additional step increases the risk of an accident or an unforeseen reaction. Second, concerns to introduce impurities of FeOCl arose when trial runs with normal iron foil were done following this procedure. Taking this into account, running the reaction towards the dichloride seemed to be the more reliable option.

Concentrated hydrochloric acid and sodium bicarbonate (both p.a.) were purchased from SigmaAldrich. A schlenk tube was connected to a schlenk line with Ar supply (AirLiquide, 99.995 %) and membrane pump vacuum ($p < 10$ mbar), which was preceded by a cold trap (liquid N_2 cooled) to freeze out corrosive vapours before the pump. The tube was capped with a PTFE tube leading into a washing bottle with a 3 mol $NaHCO_3$ solution to neutralize HCl vapour. The tube was placed in an agitated silicon oil bath on a hot plate and stirrer. Temperature was controlled electronically via thermosensor of the hot plate. 260 mg of ^{57}Fe foil were put into the schlenk tube under inert gas flow. 5 ml HCl (37%) were added in steps of 1 ml. For 1 h, no reaction was observed. Temperature was subsequently increased to 72 °C while vigorously stirring, until bubbles started to form at the iron surface, indicating the start of the reaction. The reaction mixture was kept at the aforementioned conditions for 7 h. The gas flow of the inert gas was controlled by inspecting the bubbles inside the washing bottle; it was made sure that there was a steady flow of gas from the schlenk tube to the washing bottle. After 7 h, the heating was stopped and the reaction mixture allowed to cool down over a time of 45 min. The argon flow was slightly increased and the PTFE tube and cap removed and replaced by a distillation bridge (Liebig condenser variant) with an attached 50 ml round bottom flask. The distillation bridge was also connected to a vacuum line. The inert gas flow was stopped by closing the valve at the schlenk tube, and vacuum was slowly and gradually opened at the distillation bridge. Rapid evaporation of HCl upon opening the vacuum was observed. After all HCl was evaporated, temperature was slowly increased to 80 °C until all liquid was evaporated. A residue formed on the bottom of the flask, gradually changing colour from green to a very pale blue (see figure 51). The schlenk flask was flooded with argon after closing off the vacuum, and quickly disconnected and closed off to be transferred to a glove box.

The obtained product weighed 350 mg. In terms of $^{57}FeCl_2 \cdot 2 H_2O$, this corresponds to 63 % of the theoretical yield, which is well within the literature reports(70 %, ¹²⁷).

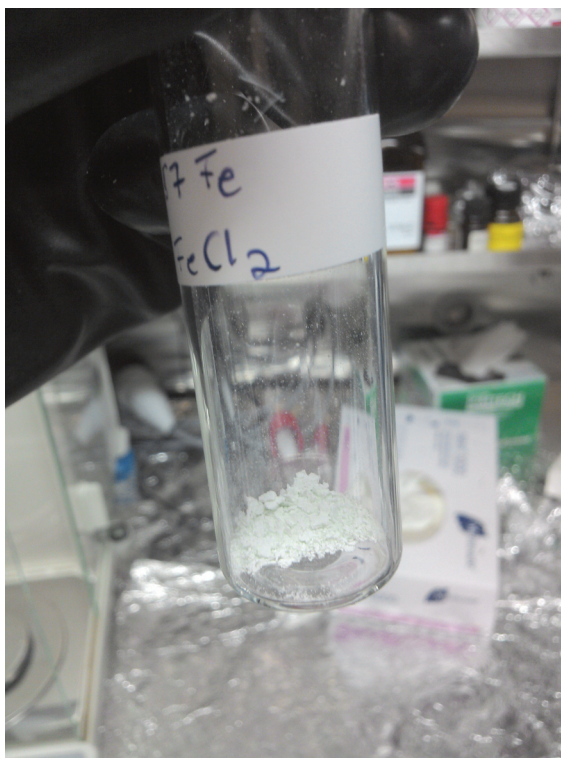


Figure 51: The final product $^{57}\text{FeCl}_2 \cdot 2\text{H}_2\text{O}$, synthesized from ^{57}Fe -foil. Note the faint blue hue characteristic for the dihydrate.

9.5 Synthesis of Nanoparticles

9.5.1 *Synthesis of Fe nanoparticles*

Two 10 ml screw cap vials were cleaned with toluene and dried in a fume hood. 25 mg of an PV2P-PS block copolymer were put into one vial and solvated in 5 ml toluene (FischerScientific, p.a.) by stirring overnight. The vial was shielded from light by tightly wrapping it in aluminium foil. In a glove box (N_2 atmosphere), 4 mg of the previously synthesized $^{57}\text{FeCl}_2 \cdot 2\text{H}_2\text{O}$ were weighed into the other vial. 5 ml toluene were added and the dispersion vigorously stirred overnight after initial sonication for 10 min. Next day, the solvated polymer was quickly added to the metal salt dispersion and stirred for 72 h while wrapped in aluminum foil.

9.5.2 *Synthesis of CuFe nanoparticles*

Two 10 ml screw cap vials were cleaned with toluene and dried in a fume hood. 25 mg of an PV2P-PS block copolymer were put into one vial and solvated in 5 ml toluene (FischerScientific, p.a.) by stirring overnight. The vial was shielded from light by tightly wrapping it in aluminium foil. In a glove box (N_2 atmosphere), 3 mg of the previously synthesized $^{57}\text{FeCl}_2 \cdot 2\text{H}_2\text{O}$ and 1 mg of $\text{CuCl}_2 \cdot 2\text{H}_2\text{O}$ were weighed into the other vial. 5 ml toluene were added and the dispersion vigorously stirred overnight after initial sonication for 10 min. Next day, the solvated polymer was quickly added to the metal salt dispersion and stirred for 72 h while wrapped in aluminum foil.

9.5.3 *Synthesis of AgFe nanoparticles*

Two 10 ml screw cap vials were cleaned with toluene and dried in a fume hood. 25 mg of an PV2P-PS block copolymer were put into one vial and solvated in 5 ml toluene (FischerScientific, p.a.) by stirring overnight. The vial was shielded from light by tightly wrapping it in aluminium foil. In a glove box (N_2 atmosphere), 2 mg of the previously synthesized $^{57}\text{FeCl}_2 \cdot 2\text{H}_2\text{O}$ and 1 mg of AgCl were weighed into the other vial. 5 ml toluene were added and the dispersion vigorously stirred overnight after initial sonication for 10 min. Next day, the solvated polymer was quickly added to the metal salt dispersion and stirred for 72 h while wrapped in aluminum foil.

9.5.4 *Synthesis of Pt nanoparticles*

Two 10 ml screw cap vials were cleaned with toluene and dried in a fume hood. 25 mg of an PV2P-PS block copolymer were put into one vial and solvated in 5 ml toluene (FischerScientific, p.a.) by stirring overnight. The vial was shielded from light by tightly wrapping it in aluminium foil. In a glove box (N_2 atmosphere), 2 mg of $\text{H}_2\text{PtCl}_6 \cdot 6\text{H}_2\text{O}$ were weighed into the other vial. 5 ml toluene were added and the dispersion vigorously stirred overnight after initial sonication for 10 min. Next day, the solvated polymer was quickly added to the metal salt dispersion and stirred for 72 h while wrapped in aluminum foil.

10 List of Publications

- 1. Plasma-assisted Oxidation of Cu(100) and Cu(111)**
S Kunze, L Tanase, M Prieto, P Grosse, F Scholten, L d S Caldas, T Schmidt, B Roldan Cuenya, to be submitted to Chemical Science, 2021
- 2. Crystallographic Orientation Dependence of Surface Segregation and Alloying on PdCu Catalysts for CO₂ Hydrogenation**
L Pielsticker, I Zegkinoglou, Z-K Han, J J Navarro, S Kunze, O Karshioğlu, S V Levchenko, B Roldan Cuenya The Journal of Physical Chemistry Letters, 12 (10), 2570-2575, 2021
- 3. The role of in situ generated morphological motifs and Cu(I) species in C₂₊ product selectivity during CO₂ pulsed electroreduction**
R M Arán-Ais, F Scholten, S Kunze, R Rizo, B Roldán Cuenya Nature Energy, 5, 317-325 (2020), 2020
- 4. In-situ structure and catalytic mechanism of NiFe and CoFe layered double hydroxides during oxygen evolution**
F Dionigi, Z Zeng, I Sinev, T Merzdorf, S Deshpande, M Bernal Lopez, and S Kunze, I Zegkinoglou, H Sarodnik, D Fan, A Bergmann, J Drnec, J F de Araujo, M Gliech, D Teschner, J Zhu, W-X Li, J Greeley, B Roldan Cuenya, P Strasser, Nature Communications, 11(1), 1-10, 2020
- 5. Operando NRIXS and XAFS Investigation of Segregation Phenomena in Fe-Cu and Fe-Ag Nanoparticle Catalysts during CO₂ Electroreduction.**
S Kunze, P Grosse, M T Bernal Lopez, I Sinev, I Zegkinoglou, H Mistry, J Timoshenko, M Y Hu, J Zhao, E E Alp, S W Chee, B Roldan Cuenya, Angewandte Chemie Int Ed, 132(50), 22856-22863, 2020

6. Prism-Shaped Cu Nanocatalysts for Electrochemical CO₂ Reduction to Ethylene

H S Jeon, S Kunze, F Scholten, B Roldan Cuenya ACS Catalysis, 8 (1), 531-535, 2018

7. Highly active single-layer MoS₂ catalysts synthesized by swift heavy ion irradiation

L Madauß, I Zegkinoglou, A Zendegani, H Vázquez Muiños, Y-W Choi, S Kunze, M-Q Zhao, C H Naylor, P Ernst, E Pollmann, O Ochedowski, H Lebius, A Benyagoub, B Ban-d'Etat, A T C Johnson, F Djurabekova, B Roldan Cuenya, M Schleberger Nanoscale, 10, 22908-22916, 2018

8. Operando Phonon Studies of the Protonation Mechanism in Highly Active Hydrogen Evolution Reaction Pentlandite Catalysts

I Zegkinoglou, A Zendegani, I Sinev, S Kunze, H Mistry, H S Jeon, J Zhao, M Y Hu, E E Alp, S Piontek, M Smialkowski, U-P Apfel, F Körmann, J Neugebauer, T Hickel, B Roldan Cuenya Journal of the American Chemical Society, 139 (41), 14360-14363, 2017

11 Curriculum Vitae

Personal

Name: Sebastian Kunze

Date of birth: 24.10.1990

Place of birth: Herdecke

Education

04.2017 - present Ph.D. Chemistry
Ruhr-University Bochum
Fritz-Haber-Institute Berlin

10.2014 - 12.2016 M.Sc. Chemistry
Ruhr-University Bochum

10.2011 - 09.2014 B.Sc. Chemistry
Ruhr-University Bochum

10.2010 - 09.2011 B.Sc. Bio-Engineering
Technical University Dortmund (no degree)

08.2001 - 06.2010 Abitur
Geschwister-Scholl-Gymnasium Wetter (Ruhr)

Eidesstattliche Versicherung

Hiermit versichere ich an Eides statt, dass ich die eingereichte Dissertation selbständig und ohne unzulässige fremde Hilfe verfasst, andere als die in ihr angegebene Literatur nicht benutzt und dass ich alle ganz oder annähernd übernommenen Textstellen sowie verwendete Grafiken, Tabellen und Auswertungsprogramme kenntlich gemacht habe. Außerdem versichere ich, dass die vorgelegte elektronische mit der schriftlichen Version der Dissertation übereinstimmt und die Abhandlung in dieser oder ähnlicher Form noch nicht anderweitig als Promotionsleistung vorgelegt und bewertet wurde.

